



HAL
open science

Seismic imaging and monitoring in mines with ambient seismic noise correlations

Gerrit Olivier

► **To cite this version:**

Gerrit Olivier. Seismic imaging and monitoring in mines with ambient seismic noise correlations. Earth Sciences. Université Grenoble Alpes, 2015. English. NNT : 2015GREAU018 . tel-01684743

HAL Id: tel-01684743

<https://theses.hal.science/tel-01684743>

Submitted on 15 Jan 2018

HAL is a multi-disciplinary open access archive for the deposit and dissemination of scientific research documents, whether they are published or not. The documents may come from teaching and research institutions in France or abroad, or from public or private research centers.

L'archive ouverte pluridisciplinaire **HAL**, est destinée au dépôt et à la diffusion de documents scientifiques de niveau recherche, publiés ou non, émanant des établissements d'enseignement et de recherche français ou étrangers, des laboratoires publics ou privés.

THÈSE

Pour obtenir le grade de

DOCTEUR DE L'UNIVERSITÉ DE GRENOBLE

Spécialité : **Sciences de la Terre, de l'Univers et de l'Environnement**

Arrêté ministériel : 7 Août 2006

Présentée par

Gerrit Olivier

Thèse dirigée par **Florent Brenguier**

préparée au sein de l'ISTerre (Institut des Sciences de la Terre)
et de l'école doctorale Terre, Univers, Environnement

Seismic imaging and monitoring in mines with ambient seismic noise correlations

2 Décembre 2015 ,
devant le jury composé de :

Florent Brenguier

ISTerre, Grenoble, France, Directeur de thèse

Richard Lynch

Institute of Mine Seismology, Hobart, Australia, Co-Encadrant de thèse

Ludovic Margerin

Observatoire Midi-Pyrénées, Toulouse, France, Rapporteur

Jean Schmittbuhl

EOST, Strasbourg, France, Rapporteur

François Cornet

EOST, Strasbourg, France, Examineur

Nick Arndt

ISTerre, Grenoble, France, Président



Remerciements

I wish to thank the following people for making it possible for me to complete my PhD at ISTerre under unique and challenging circumstances:

- My advisor Florent Brenguier for the support he has given me and for helping to make this project happen. You have not only been very helpful for my project, but your work ethic, positive attitude and creative thinking in solving problems has been very inspiring to me.
- The Institute of Mine Seismology for assisting me financially during my PhD project. Thanks in particular to Richard Lynch for giving me this wonderful opportunity, for which I am very grateful.
- Michel Campillo, Philippe Roux and Nikolai Shapiro who have also helped me a lot through the course of my project. Your inputs and discussions have not only been very valuable, but also enjoyable.
- My jury members for taking the time to evaluate my work.
- My family and friends for all the support over the years.
- Amy for being so supportive and patient (especially towards the end).

Abstract

This work focussed on the use of the seismic noise generated by mining activity to reconstruct the seismic Green's functions between underground seismic sensors - effectively turning sensors into virtual sources. Over the last decade this method has become an increasingly popular tool in crustal seismology and volcanology.

In this dissertation I show that the seismic noise generated by mining activity is not ideally suited to reconstruct seismic Green's functions. However, good estimates of the seismic Green's functions between sensors in an underground mine can be retrieved if a processing scheme is used that compensates for monochromatic signals and irregular source distribution. With these Green's functions, I constructed a 3D body-wave velocity model of the underground mining environment without using any costly active sources. The 3D velocity model shows the existence of a high-velocity zone that overlaps with a known ore-body, highlighting the potential of this method for mineral exploration purposes. The successful recovery of the seismic Green's functions enable many other potential applications in the mining industry.

In this dissertation I also show how these estimates of the seismic Green's function can be used to measure small (0.01%) hourly changes in the seismic velocity to investigate the response of a rock mass to a sudden dynamic and static stress change. I performed an experiment to examine: (1) the influence of dynamic and static stress perturbation on seismic velocities, (2) elastic static stress changes and (3) induced earthquake activity associated with a blast and removal of a piece of solid rock. Overall I observed that the blast induced a sudden decrease in seismic velocities, followed by a slow relaxation lasting up to 5 days. Only after this, permanent changes in seismic velocity become apparent. After comparing the spatial pattern of permanent seismic velocity changes with elastic static stress modelling, I inferred that the permanent seismic velocity changes are due to the change in the static volumetric stress induced by the removal of a solid piece of rock by the blast. This is the first instance that noise-based permanent seismic velocity changes associated with static stress changes have been observed.

This dissertation shows the potential of using noise-based seismic imaging and monitoring methods in conjunction with traditional microseismic monitoring to improve safety in mines.

Contents

Part I Methods and Concepts Page 23

2	Seismic interferometry and ambient seismic noise	25
2.1	Wave equation and seismic Green's function	25
2.2	Reconstructing the Green's function with interferometry	26
2.2.1	Mathematical derivation	27
2.2.2	A numerical example	32
2.3	Ambient seismic noise	34
3	Seismic velocities and coda-wave interferometry	37
3.1	Seismic velocities in rock	37
3.1.1	Dependence on stress	38
3.1.2	Dependence on damage	40
3.2	Coda-wave interferometry	41

Part II Applications Page 43

4	Past applications in crustal seismology	45
4.1	Tomography	45
4.2	Monitoring changes in seismic velocity	47
5	Potential applications in a mining environment	51
5.1	3D Seismic velocity models	52
5.1.1	Imaging the subsurface	52
5.1.2	Accurate microseismic event locations	54
5.2	Monitoring velocity variations	54
5.2.1	Measuring stress changes	54

5.2.2	Measuring damage and relaxation for re-entry protocols	55
5.2.3	Monitoring slope stability in open pit mines	56

Part III Reconstruction of seismic Green’s function _____ Page 59

6	Seismic interferometry with mining noise	61
6.1	Introduction	62
6.2	Numerical simulations	64
6.2.1	Creating a realistic model	66
6.2.2	Scattering caused by mining excavations	67
6.2.3	Influence of source-receiver distance on scattering regime	70
6.3	Data	70
6.3.1	Examining scattering properties with microseismic events	71
6.4	Ambient noise cross-correlations	74
6.4.1	Stationary phase locations	74
6.4.2	Monochromatic sources	74
6.4.3	Selective stacking	75
6.4.4	Directional bias from non-isotropic wavefields	80
6.4.5	Convergence of cross-correlation functions to the seismic Green’s functions	80
6.4.6	Frequency content of the cross-correlation functions.	82
6.4.7	3D S-wave velocity model	83
6.5	Conclusions	85
6.6	Appendix A	88
6.6.1	Inversion of the mean-free-path	88
6.7	Appendix B	89
6.7.1	Determination of S-wave arrival with kurtosis estimator	89
6.7.2	3D Tomography	90
6.7.3	Checkerboard resolution test	92

Part IV Measuring seismic velocity variations _____ Page 95

7	Measuring seismic velocity variations in an underground mine	97
7.1	Preliminary methods and parameters	98
7.1.1	Determining window for measuring velocity variations	98

7.1.2	Calculation of relative velocity variations	98
7.1.3	Inversion for time dependent velocity changes	100
7.2	Introduction	102
7.3	Data and methods	104
7.4	Results	108
7.5	Conclusions	111
Conclusions and perspectives		113
Bibliography		117

CONTENTS

List of Figures

2.1	Illustration of the reference frame used for the mathematical derivation of the Green's function between two receivers. Receiver 1 is located at the origin, while receiver 2 is located on the x-axis at position $[R,0,0]$	28
2.2	Setup of the numerical simulation. The triangles indicate the locations of the sensors while the circles indicate the positions of the sources. The locations of the stationary phase locations, as described in the previous section, are shown in red.	32
2.3	The cross-correlation functions for each azimuth along with the sum of all azimuths. The sum of all azimuths represents the signal that would be recorded if one of the sensors are replaced by a source.	33
2.4	A comparison of the sum of all azimuths and a sum of the cross-correlation functions when sources were located in stationary phase locations.	34
2.5	Fourier spectra of the high-frequency noise for (a) vertical component and (b) north-east component recorded in an urban area (Grenoble, French Alps) from Bonnefoy-Claudet et al. (2006). The spectral amplitudes exhibit clear daily and weakly variations related to human activity.	35
3.1	Schematic showing how a change in pressure can cause a change in rock mass and seismic velocity. Here the increased atmospheric air pressure closes microcracks and results in a slight increase in velocity.	38
3.2	A schematic showing how a sudden dynamic stress perturbation (like a blast) can cause a change in the rock mass and seismic velocity. Here the blast induces damage and opens microfractures so that the velocity decreases.	40
3.3	Two hammer shots recorded in a mining pillar after the stress was changed, from Grêt et al. (2006). The change in the medium is not visible in the direct arrival, but clearly visible in the coda.	41
4.1	(a) Raleigh wave isotropic phase speed map from ambient seismic noise and, (b) amplitude and fast direction of the Raleigh wave phase velocities from Ritzwoller et al. (2011).	46

LIST OF FIGURES

4.2	3D reflection image of the Sirte basin created with ambient seismic noise correlations, from Draganov et al. (2009). The horizontal lines indicate discontinuities in the crust.	47
4.3	Seismic velocity changes during the M6.0 Parkfield earthquake measured with ambient seismic noise, as reported in Brenguier et al. (2008a).	48
4.4	(A) Image of the instantaneous seismic velocity change in Japan due to the M9.0 Tohoku-Oki earthquake and (B) seismic velocity susceptibility, determined by the seismic velocity response compared to the dynamic strain change from the earthquake. Figure from Brenguier et al. (2014).	49
5.1	Seismic surveys at the Outokumpu sulfide deposits in Finland taken from Kukkonen et al. (2011). The strong reflectors here are from an ophiolite unit that hosts the sulfide mineralisation.	53
5.2	Figure from Westman et al. (2012) showing velocity contours from double-difference tomography around caved regions indicating the redistribution of stresses.	55
5.3	Photo of the landslide that occurred at Bingham Canyon mine (Ravell Call, Deseret News, 2013)	56
6.1	Section view and plan view of Boliden’s Garpenberg mine in Sweden. The sensors are indicated by blue triangles, the ray paths of the cross-correlation pairs are shown in red and mining tunnels are gray. The red dot on the inset shows the regional location of the mine.	65
6.2	The difference between synthetic seismograms with and without the tunnels and excavations included in the model but with the same source time function (impulsive downward). When tunnels and excavations are included in the model, the seismic waves scatter multiple times and a lot of energy is present in the coda part of the seismogram. For the synthetic seismogram recorded when the tunnels are not included, the only remarkable feature after the body-wave arrivals (weak P- and strong S-wave) is the reflection off the free surface at roughly 0.31 seconds. When the tunnels are included, the direct S-wave arrival is only visible for lower frequencies (below 100 Hz) and the reflection off the free surface is buried by the multiply scattered waves in the coda.	68

6.3 The processing steps taken to invert for the mean-free-path with the synthetic seismograms. The top left figure shows the seismogram band-pass filtered in the range 170 - 220 Hz. The top right figure shows the seismogram after it has been transformed to energy density defined in Equation A.3. The bottom left figure shows the energy density after it was smoothed by a 100 millisecond box window with the control curve (inversion result) in red. The bottom right figure shows the logarithmic function from Equation A.2 along with the computed inversion result in red. The mean-free-path that fits the synthetic data the best was found to be 32 meters for this frequency range. 69

6.4 A seismogram of length 5 seconds showing the changes in seismic noise. Three distinct time periods have been marked in the seismogram: In the first block the repetitive impacts of a hammer drill are visible. Drilling occurs in multiple places during a normal day of mining. The second block shows no distinct features. The noise here is due to a combination of far away sources like trucks, ventilation fans and ore crushing. In the third block a recorded microseismic event is shown. This event has a local magnitude of -3 and was located roughly 30 meters away from the seismic sensor. Thousands of these microseismic events happen in a given day. The bottom three windows show the power spectral density of each time period. For the middle time period with background noise, it is clear that the signal is very peaked in frequency whereas for the other two periods seismic energy is present in a broad frequency range from 10 - 3000 Hz. . . . 72

6.5 A recorded microseismic event filtered in the low frequency band (below 100 Hz) and high frequency band (above 200 Hz). In the low frequency band the direct P- and S-wave arrivals are picked and in the high frequency band the mean-free-path is determined (see Appendix A). The mean-free-path found by the inversion here is 43 meters. The low value of the mean-free-path for the microseismic event is in agreement with the numerical simulations performed in Section 1. 73

6.6 Comparison of the cross-correlation function for one station pair when a subset of 43% of the data is stacked (bottom) compared to the cross-correlation function when all of the data is stacked (top). The cross-correlation function shows direct P and S-wave arrivals when 43% of the data is used. The expected P- and S-wave arrivals are indicated by black lines. The direct arrivals are not clearly visible when all the data is used. Instead we see regularly spaced peaks because of the influence of monochromatic sources. 76

LIST OF FIGURES

6.7 Two 10 second periods of continuous data recorded by the same sensor at different times. At the time of the top figure, 61% of the correlation pairs passed the selective stacking criteria. This is thanks to the multiple sources and broadband content of the data. At the bottom figure only 13 % of the correlation pairs passed the selective stacking criteria. During this time the noise is dominated by ventilation fans that are very peaked in frequency. 78

6.8 The cross-correlation functions arranged by the inter-sensor distance. Figure (A) shows the CCFs when conventional blind vertical stacking are applied. No clear arrival fronts are visible. Figure (B) shows the CCFs when the selective stacking scheme is applied. A S-wave arrival front is visible. The picks that were obtained by the kurtosis-based algorithm are shown in red. Figure (C) shows the synthetic Green’s functions generated with numerical simulations. The synthetic Green’s functions show a weak P-wave arrival and a strong S-wave arrival. The expected arrival times in the synthetic Green’s functions are shown with black lines. 79

6.9 The location of two sensors and the cross-correlation of the seismic noise recorded in them when the selective stacking scheme is used. The causal part (orange) of the cross-correlation function has a strong apparent S-wave arrival whereas the acausal part (purple) has a comparatively weak S-wave arrival. The directional bias of the cross-correlation function can be described by the scatterers in the stationary phase locations: behind sensor A there are many mining excavations that ensures that seismic waves propagate from the stationary phase location from A to B regularly, while behind sensor B there are not as many mining excavations so that seismic waves do not propagate from the stationary phase location from B to A as frequently. 81

6.10 The convergence of the cross-correlation function to the Green’s function. The S-wave arrival is stable after 12 hours (8 hours effective time). After 30 days (20 days effective time), the non-physical arrivals are weaker and a faint P-wave arrival can be seen. The effective time refers to cumulative time that passed the selective stacking criteria and therefore the actual amount of data used to construct the correlation functions. 82

6.11 The different frequency components of the cross-correlation function. Direct P- and S-wave arrivals are visible for the low frequency part of the CCF, whereas the high frequency part is diffuse due to the scattering by the tunnels and excavations. As a result there is no clear direct P- and S-wave arrivals. The inversion of the mean-free-path is shown in the bottom window and was determined to be 37 m. 84

6.12 The S-wave picks (blue) from the automatic Kurtosis based algorithm along with the homogeneous least squares solution (solid red) as a function of distance for cross-correlation functions with successful S-wave picks. The maximum allowed picking variations are indicated by the dashed red lines. The picking constraints ensure that other local maxima (scattered P- or S-waves) are not mistakenly picked as S-wave arrivals. 85

6.13 2D cross section of the result of the 3-dimensional S-wave velocity inversion. The velocity is slightly higher in the tunnel network in the Kaspersbo section on the right and slightly lower in the tunnel network in the Lappberget section on the left. The outlines of known ore bodies are shown in the bottom figure. The locations of these ore bodies are determined by drill samples. The high velocity structure overlaps with the Kaspersbo ore body. 86

6B.1 Determining the S-wave arrival by the kurtosis estimator. We consider maximum value of the positive derivative of the kurtosis estimator as the arrival of the S-wave. 90

6B.2 2D cross section of the synthetic 3D velocity model used to create the Green's functions for the checkerboard resolution test. 91

6B.3 2D cross section of the result from the inversion of data generated by the synthetic checkerboard velocity model. This shows the achievable resolution with the number of successful picks made of the S-wave arrivals of the cross-correlation functions. The outer edges of the checkerboard model can not be retrieved since no rays pass through them. For the interior of the array, the correct velocities structures were mostly recovered. 92

7.1 Stack of cross-correlation functions for the entire 25 day period for one station pair (top) and the envelope and smoothed envelope (bottom). The coda part of the cross-correlation function decays exponentially up to -0.6 and 0.4 seconds lag-time, after which the aliasing of the monochromatic signals prevent the coda waves to decay as expected. 99

7.2 Travel time variations measured with the MWCS technique for two cross-correlation functions. The colors of the points (bottom) indicate the coherence of the cross-correlation functions in each lag-time window. After 0.5 seconds there are points with high coherence, but with small delay times. This is due to the aliasing of monochromatic signals. 100

LIST OF FIGURES

7.3	Travel time variations for one station pair. The travel time variations are shown using the standard stack and compare method (top). The color indicates the coherence of the value and is indicative of the error. The large fluctuations are obtained when the coherence is low. The travel time variations obtained by inverting for the travel time curve are shown in the bottom panel along with the standard method. Since the inversion takes the coherence of each measurement as a weight, the large fluctuations when the coherence is low for the standard method disappears.	101
7.4	Side view of the mine plans of Boliden’s Garpenberg mine in Sweden along with the locations of the seismic sensors (top). Zoomed view of the location of the blast and the proceeding aftershocks (bottom). The aftershocks are coloured by the amount of time elapsed after the blast. The aftershocks are not located homogeneously around the area where blasting occurred and no clear migration pattern is visible.	105
7.5	Stack of all cross-correlation functions (top) and hourly cross-correlation functions for one station pair for the 12 day period (bottom). The time of the blast is indicated by a black dotted line. The cross-correlation functions appear stable for up to at least 0.7 second lag-time. The inset indicates which stations were used to construct the cross-correlation functions. The grey rectangles indicate the windows that were considered when measuring the velocity variations (after the direct S-wave, up to 0.4 seconds).	107
7.6	Seismic velocity variations averaged for one sensor (top). Three features are present: an immediate decrease during the blast, relaxation that takes up to 5 days after the blast and the permanent change in baseline of the seismic velocity. The bottom figure shows the cumulative number of events recorded during the 15 day period, along with the number of events recorded every 10 minutes. The inset shows a zoomed view of the hour in which the blasting took place. The seismic activity rate peaks at 7 minutes after the blast.	109
7.7	Comparison of iso-surfaces of the immediate change in the seismic velocity, the permanent change in the seismic velocity and the modeled volumetric stress change. The permanent change in the seismic velocity (5 days after blast) and the modeled static stress change are qualitatively in agreement for most locations.	110

Chapter 1

Introduction

Contents

2.1	Wave equation and seismic Green's function	25
2.2	Reconstructing the Green's function with interferometry . . .	26
2.2.1	Mathematical derivation	27
2.2.2	A numerical example	32
2.3	Ambient seismic noise	34

1.1 Background and motivation

Over the last decade, a new branch of seismology has emerged that has proven to be useful for a wide variety of applications. Essentially this method uses the ambient seismic noise that is recorded everywhere in the earth to turn receivers into virtual seismic sources. These virtual source signals carry information of the medium through which they travel and can be used in the same way that earthquakes or active sources are used to image and monitor the elastic properties of the earth. By using this method it has been possible to image the earth's crust, monitor and anticipate volcanic eruptions and mud landslides, measure the response of the earth's crust to large earthquakes and many other applications, without the need for earthquakes or costly active sources.

The method relies on the fact that the interaction of the incoming ocean waves with the solid earth generate stable seismic signals that are recorded everywhere in the earth's crust. The wavelengths of these surface waves are several kilometres long and therefore not usable in small scale industrial settings like mines. The seismic noise recorded at higher frequencies are typically generated by human activity, which can be erratic, monochromatic and unstable and thus generally unsuitable for the ambient seismic noise method. This is unfortunate, since many underground and open pit mines have dense

modern seismic monitoring networks that are capable of continuously recording high-frequency seismic signals.

For my PhD project, I examined whether the ambient noise method can nonetheless be applied to seismic noise recorded in an underground mining environment. In my opinion there are many potential applications for this method in mines (which I discuss in the following chapter). The primary objective of this project revolves around improving safety in mines. With the growing global demand for mineral resources, mines are getting deeper and are approaching depths of up to 4 km (for instance Mponeng gold mine, South Africa). At these depths, the natural temperature of rock can be as high as 50 degrees Centigrade and the virgin vertical confining stress can be of the order of 100 MPa. In these high-stress environments rock-bursts and mining induced seismicity can create environments that are extremely dangerous. Although considerable improvements in monitoring seismic activity in mines have been made over the last 20 years (see for example [Riemer and Durrheim, 2011](#)), mining induced earthquakes are still one of the leading causes of fatalities in deep underground mines and remain hard to anticipate.

Over the last four years, I have balanced working at the Institute of Mine Seismology (IMS) and completing my PhD. IMS is the world leader in microseismic monitoring in mines and currently has more than 200 customers around the world. IMS is an independent private research organization focused on developing methodologies, technologies and services for monitoring and modelling the seismic rock mass response to mining. My role at IMS gave me the opportunity to experience the technology and methodologies currently being used in microseismic monitoring for the mining industry first hand. Unlike regional earthquakes, practically all seismic events in mines are induced. As a result, the seismic activity in mines is potentially controllable - if the seismic hazard in an area is elevated, a large seismic event could be prevented or delayed if mining is temporarily halted in this area. Currently it is standard practise to determine the seismic hazard with the temporal and spatial clustering of microseismic events. In my opinion, state-of-the-art seismic techniques (like monitoring with ambient seismic noise) should be investigated in mining environments to assist in the identification of seismic hazard and ultimately improve miner safety.

Apart from the safety incentives in investigating new seismic monitoring techniques, mines are well instrumented underground laboratories that fit naturally between laboratory and crustal scales. Currently, more than 300 mines around the world have seismic monitoring networks. Many of these are dense, modern networks capable of recording continuous data at high sampling rates. Some of these mines are very seismically active and record and locate more than 10000 microseismic events per day. As a result, the data recorded in mines can provide unique insights into unresolved issues in crustal seismology. These issues include: the mechanisms of earthquake triggering, identification of precursory signs of earthquakes, the spatial and temporal distribution of aftershocks, etc. Even though in this dissertation I will only consider data recorded in an underground

mine, I will attempt to extrapolate my findings to provide insights into these phenomena at different scales.

Since the data recorded in an underground mine differs greatly from data recorded by seismic surface arrays, it has been necessary to adapt and substantially modify the methods developed in crustal seismology in order for this method to work in this particular environment. The techniques I developed towards this goal could potentially be applied in other industries, like oil and gas, geothermal reservoirs or hydraulic fracturing.

1.2 Outline of the dissertation

During my PhD project I focussed on adapting the revolutionary methods involving ambient seismic noise correlations so that they can be applied in a mining environment.

Before I could show any useful applications of this method in mines, I needed to investigate whether it was possible to reconstruct the seismic Green's functions with the noise generated by mining activity. Since the nature of the noise generated by human activity is completely different from the stable noise emanating from the interaction of the incoming ocean waves with the solid earth, I encountered many aspects that prevented the cross-correlation functions to converge to the seismic Green's function. I developed a processing scheme that compensates for the imperfect seismic sources and ultimately succeeded in recovering good estimates of the broadband seismic Green's function. The good estimates of the seismic Green's function were used to image the velocity structure of the underground mine and to investigate the scattering caused by underground tunnels and voids. To my knowledge, this was the first successful application of this method in a mining environment.

I then turned my attention to using the reconstructed seismic Green's functions to make regular estimates of the seismic velocity variations in the vicinity of the underground sensors. Since the seismic velocities are sensitive to a number of physical properties of solid rock, including stress change and fracturing, the seismic velocities can provide valuable insights into how the rock mass is responding to mining activities. Accurate (0.01%) measurements of seismic velocity variations were compared to mining and microseismic activity. I found that these measurements are sensitive enough to monitor short- and long-term changes of the rock mass in the presence of dynamic and static stress perturbations. Here I present the first instance in which noise-based permanent seismic velocity changes associated with static stress changes are observed.

These are the main results presented in my dissertation, which is organized in four main parts:

In Part I, I discuss the relevant methods and concepts that will be used throughout this dissertation. I show a mathematical derivation of how the seismic Green's function can be constructed by seismic interferometry and show how this can be applied in practice by conducting a simple numerical simulation. Good knowledge of the underlying mathematical theory behind the method proved to be very useful to reconstruct the seismic Green's function in the presence of imperfect seismic source distribution I encountered in the mine data. I also discuss the nature of seismic noise that is typically recorded at different scales, the origins of seismic velocity variations in rock and coda-wave interferometry.

In Part II, I look at the past applications of this method in different settings for two categories: imaging and monitoring. The past applications served as motivation and lead me to potential applications of this method in a mining environment, which served as added motivation for this study. These applications are dependent on whether I can show that it is possible to use noise recorded in mines to construct seismic Green's functions between sensors.

Part III deals with creating seismic Green's functions with noise induced by mining activities. Here I discuss the modification of the developed cross-correlation technique so that it can be applied in a mining environment to reconstruct the seismic Green's functions. I also show how the Green's functions can be used to image the underground mining environment and investigate the scattering caused by the mining excavations.

Part IV deals with measuring seismic velocity variations in an underground mine with the Green's functions constructed with seismic interferometry. In this part I show that the seismic velocities can be measured accurately enough on an hourly basis to show how the rock mass is responding to mining activities. In particular, I show how a blast in an underground mine causes immediate and permanent changes in the seismic velocity and show how these changes in seismic velocity are related to aftershock activity and permanent changes in the static stress field.

Finally, I conclude the dissertation by summarising the findings of the project and discussing the implications and potential future avenues resulting from my work.

1.3 List of publications

My dissertation contains two articles that have been published or accepted by scientific peer-reviewed journals:

- Chapter 6: Body-wave reconstruction from ambient seismic noise correlations in an underground mine, *Geophysics*, 2015, 80(3), KS11-KS25, by Gerrit Olivier, Florent Brenguier, Michel Campillo, Richard Lynch, Philippe Roux, 10.1190/GEO2014-0299.1

- Chapter 7: Investigation of coseismic and postseismic processes using in situ measurements of seismic velocity variations in an underground mine, *Geophysical Research Letters*, 42, 9261–9269, by Gerrit Olivier, Florent Brenguier, Michel Campillo, Philippe Roux, Richard Lynch, Nikolai Shapiro, 10.1002/2015GL065975

Part I

Methods and Concepts

Chapter 2

Seismic interferometry and ambient seismic noise

Contents

3.1	Seismic velocities in rock	37
3.1.1	Dependence on stress	38
3.1.2	Dependence on damage	40
3.2	Coda-wave interferometry	41

In this chapter I will introduce some of the methods and concepts that will be used throughout this dissertation.

2.1 Wave equation and seismic Green's function

The general form of the seismic wave equation (see [Aki and Richards, 1980](#)) is given by

$$\rho \frac{\partial^2 u}{\partial t^2} = \nabla \lambda (\nabla \cdot u) + \nabla \mu \cdot [\nabla u + (\nabla u)^T] + (\lambda + 2\mu) \nabla \nabla \cdot u - \mu \nabla \times \nabla \times u. \quad (2.1)$$

In the case of a homogeneous medium, the first two terms of the wave equation disappear since they contain gradients of the Lamé parameters so the wave equation simplifies to:

$$\rho \frac{\partial^2 u}{\partial t^2} = (\lambda + 2\mu) \nabla \nabla \cdot u - \mu \nabla \times \nabla \times u. \quad (2.2)$$

We can write the wave equation in terms of the P-wave velocity, α , and S-wave velocity, β , by introducing the expressions:

$$\alpha^2 = \frac{\lambda + 2\mu}{\rho}, \beta^2 = \frac{\mu}{\rho}, \quad (2.3)$$

and substituting them into equation (2.2) to give:

$$\frac{\partial^2 u}{\partial t^2} = \alpha^2 \nabla \nabla \bullet u - \beta^2 \nabla \times \nabla \times u. \quad (2.4)$$

The seismic Green's function between points 1 and 2 is a solution to the seismic wave equation for an impulse source satisfying the boundary conditions $G_{1,2}(t = 0) = 0$, $\frac{\partial G_{1,2}}{\partial t}(t = 0) = 0$ and $G_{1,2}(t) = 0$ if $r_{1,2} \rightarrow \infty$, where $r_{1,2}$ is the distance between points 1 and 2. The Green's function is given by:

$$G_{1,2}(t) = \frac{1}{4\pi c} \frac{\delta(t - \frac{r_{1,2}}{c})}{r_{1,2}}, \quad (2.5)$$

where δ denotes the Dirac delta function and c is the wave velocity. The seismic Green's function therefore refers to the signal that would be recorded at one of these points if the other point was an impulsive source and carries information about the medium between the points. The Green's function here can represent displacement, velocity or acceleration.

2.2 Reconstructing the Green's function with interferometry

Almost 50 years ago, Claerbout argued that "by cross-correlating noise traces recorded at two locations on the surface, we can construct the wave field that would be recorded at one of the locations if there was a source at the other" (Claerbout, 1968). Claerbout's conjecture was well before its time and only gained momentum in the seismology community a few decades later after the approach was successfully applied to helioseismic data (Duvall et al., 1996). A few years later Lobkis and Weaver (2001) showed that the Green's function emerges between two ultrasonic sensors when cross-correlating the signal recorded in them in the presence of a diffuse ultrasonic field. Here the authors remarked that equipartition of modes or a fully diffuse wavefield is required to retrieve the Green's function. This is an condition that is relatively easy to fulfill in ultrasonic experiments, but not realistic in seismology.

Derode et al. (2003) showed that the Green's function can be retrieved by cross-correlation even in the absence of diffusivity with an argument based on time-reversal symmetry. However, the time-reversal symmetry is not valid in the presence of attenuation. Wapenaar (2004) used a reciprocity theorem to show that the Green's function can be retrieved in any inhomogeneous medium by cross-correlating the recordings of two sensors located at a free surface, also in the absence of diffusivity. However, this derivation required the receivers to be located at the surface.

[Snieder \(2004\)](#) showed that in a homogeneous elastic medium with scatterers that act as secondary sources, one can retrieve the Green's function by cross-correlating the signals recorded in two receivers with the stationary phase approximation. This derivation did not require the receivers to be located at surface and applied to any 3D distribution of sensors. Since then there have been numerous authors who have shown mathematically that the Green's function can emerge from seismic noise recordings (for a thorough review of these derivations and a discussion of their similarity see [Boschi and Weemstra, 2015](#)).

Before I proceed with applying this method to real seismic data, I will examine a mathematical proof of the method and the circumstances under which it is valid. A good understanding of the underlying theory could be crucial to apply this method in an unfamiliar environment.

2.2.1 Mathematical derivation

The mathematical derivation I will present is valid for two receivers in a 3D homogeneous elastic medium surrounded by large number of impulsive sources. The derivation follows the arguments presented in [Snieder \(2004\)](#). I consider this derivation to be the most appropriate for an underground mining environment, since it holds true for a 3D distribution of receivers and is valid in the presence of attenuation and absence of diffusivity.

Consider two receivers located in a 3D homogeneous medium surrounded by impulsive sources. The reference frame is chosen so that receiver 1 is at the origin and receiver 2 is on the x-axis at a distance R (see [Figure 2.1](#)).

The signal recorded at receiver 1 (u_1) from an impulsive source, S , is given by the Green's function as specified in [equation \(2.5\)](#)

$$u_1(t) = G_{1,S}(t) = \frac{1}{4\pi c} \frac{\delta(t - \frac{r_1^S}{c})}{r_1^S}, \quad (2.6)$$

where δ denotes the Dirac delta function, c is the wave velocity, and r_n^S is the distance between receiver n and source S . The cross-correlation function between the signals from source S recorded at receivers 1 and 2 is then given by

$$C_S(t) = \int_0^T G_{1,S}^*(\tau) G_{2,S}(\tau + t) dt. \quad (2.7)$$

Imagine a scenario where the receivers are surrounded by a large number of sources. Now, the signal recorded at a receiver can be written as the superposition of the Green's

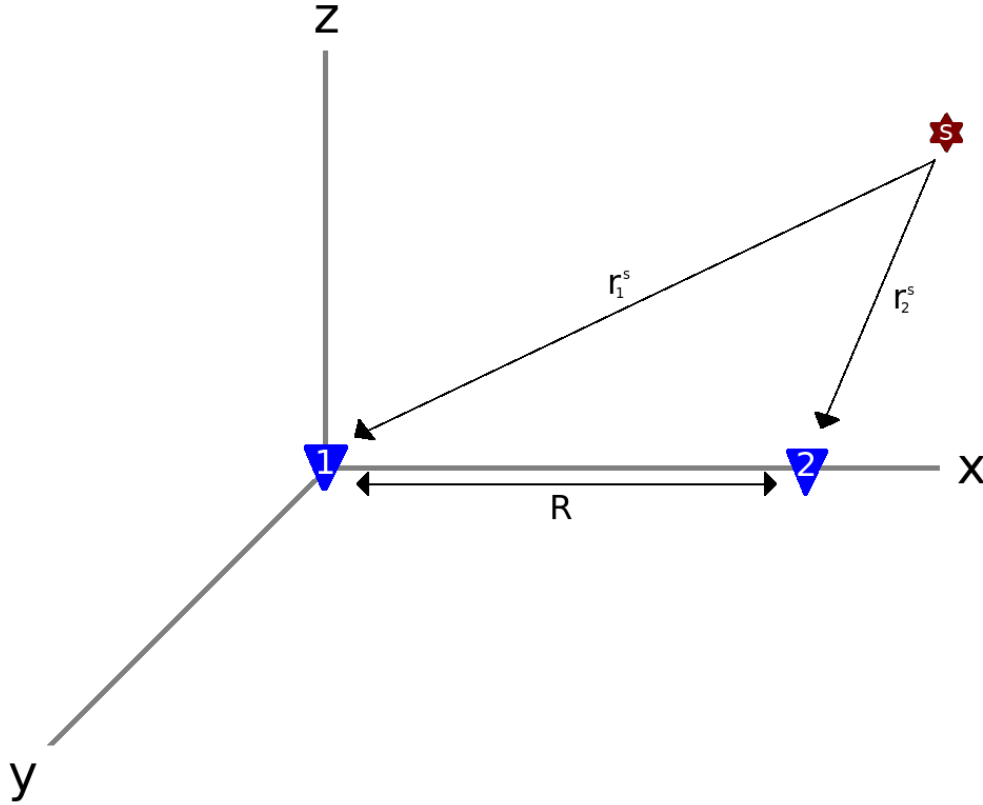


Figure 2.1 – Illustration of the reference frame used for the mathematical derivation of the Green’s function between two receivers. Receiver 1 is located at the origin, while receiver 2 is located on the x-axis at position $[R,0,0]$.

functions between each source and the receiver:

$$u_1(t) = \sum_S G_{1,S}(t) = \sum_S \frac{1}{4\pi c} \frac{\delta(t - \frac{r_1^S}{c})}{r_1^S}. \quad (2.8)$$

The cross-correlation function between the signals from all sources recorded at receivers 1 and 2 is then given by the double sum

$$C(t) = \sum_S \sum_{S'} \int_0^T G_{1,S}^*(\tau) G_{2,S'}(\tau + t) dt. \quad (2.9)$$

The double sum can be split into diagonal ($S = S'$) and cross terms ($S' \neq S$). In general the cross terms are non-zero. However, as shown in [Snieder \(2004\)](#), if the sources are spatially and temporally uncorrelated, the cross terms vanish in the limit $S \rightarrow \infty$ or $T \rightarrow \infty$. This limit is referred to as *time/event averaging*. Physically, the cross terms are non-zero when signal recorded at receiver 1 from a source correlates with signal recorded in receiver 2

from a different source. Ignoring the cross terms, the cross-correlation function becomes

$$C(t) \approx \sum_S \int_0^T G_{1,S}^*(\tau) G_{2,S}(\tau + t) dt = \sum_S C_S(t). \quad (2.10)$$

This means that the cross-correlation function of the signals recorded by two sensors for N randomly placed sources is approximately equal to the sum of the N cross-correlation functions of signals containing only one source in each of the N locations. The Green's function in frequency domain is given by the Fourier transform of equation (2.6)

$$G_{1,S}(\omega) = \frac{1}{4\pi c} \frac{1}{\sqrt{2\pi}} \frac{\exp[-i\omega r_1^S/c]}{r_1^S}. \quad (2.11)$$

Taking the Fourier transform of equation (2.10) and substituting this in equation (2.11) gives

$$\begin{aligned} \mathcal{F}(C(t)) &= C(\omega) \\ &= \sum_S G_{1,S}^*(\omega) \cdot G_{2,S}(\omega) \\ &= \frac{1}{2^4 \pi^3 c^2} \sum_S \frac{1}{r_1^S r_2^S} \exp\left[\frac{i\omega}{c}(r_1^S - r_2^S)\right]. \end{aligned} \quad (2.12)$$

In the limit $S \rightarrow \infty$, we can replace the sum over sources with a volume integral that is weighted by n_v , which is the number of sources per unit volume. Equation 2.12 then becomes

$$C(\omega) = \frac{1}{2^4 \pi^3 c^2} \int \frac{\exp[i\omega(r_1^S - r_2^S)/c]}{r_1^S r_2^S} n_v dx dy dz. \quad (2.13)$$

For large $\frac{\omega}{c}$ the integrand is rapidly oscillating and the integration over the x and y coordinates can be approximated with the stationary phase method (see [Bender and Orszag, 1999](#)). The stationary phase approximation is exact in the limit $\frac{\omega}{c} \rightarrow \infty$ or in terms of the wavelength, $\lambda \rightarrow 0$. After applying this approximation

$$C(\omega) \approx \frac{i}{2^3 \pi^2 \omega c} \int_{-\infty}^{\infty} \frac{\exp[\frac{i\omega}{c}(|x| - |R - x|)]}{||x| - |R - x||} n_v dx. \quad (2.14)$$

To evaluate the remaining integral, I split the integration range into: $x < 0$, $0 < x < R$ and $x > R$, so that

$$C(\omega) = \frac{i}{2^3 \pi^2 \omega c} \left(\int_{-\infty}^0 \frac{e^{ikf(x)}}{|f(x)|} n_v dx + \int_0^R \frac{e^{ikf(x)}}{|f(x)|} n_v dx + \int_R^{\infty} \frac{e^{ikf(x)}}{|f(x)|} n_v dx \right), \quad (2.15)$$

where

$$f(x) = \begin{cases} -R, & \text{if } x < 0 \\ 2x - R, & \text{if } 0 < x < R \\ R, & \text{if } x > R. \end{cases}$$

The integrand for the region $0 > x > R$ is oscillatory and as a result it's contribution is much smaller to the final integral than the integrands for other regions. Neglecting this term gives

$$\begin{aligned} C(\omega) &= \frac{i}{2\pi\omega c} \left(\frac{e^{-ikR}}{4\pi R} \int_{-\infty}^0 n_v dx + \frac{e^{ikR}}{4\pi R} \int_R^{\infty} n_v dx \right) \\ &= \frac{i}{\sqrt{2\pi}\omega} \left(G_{1,2}(\omega) \int_{-\infty}^0 n_v dx + G_{1,2}(-\omega) \int_R^{\infty} n_v dx \right). \end{aligned} \quad (2.17)$$

Now, if we take the inverse Fourier transform of equation (2.17) to go back to time domain

$$C(t) = \frac{i}{2\pi} \left(\int_{-\infty}^0 n_v dx \int_{-\infty}^{\infty} \frac{1}{\omega} G_{1,2}(\omega) e^{i\omega t} d\omega + \int_R^{\infty} n_v dx \int_{-\infty}^{\infty} \frac{1}{\omega} G_{1,2}(-\omega) e^{i\omega t} d\omega \right). \quad (2.18)$$

If we take the time derivative on both sides of equation (2.18) the $\frac{1}{\omega}$ factors disappear so that that

$$\frac{d}{dt} C(t) = \frac{-1}{2\pi} \left[G_{1,2}(t) \int_{-\infty}^0 n_v dx - G_{1,2}(-t) \int_R^{\infty} n_v dx \right]. \quad (2.19)$$

The term $G_{1,2}(t)$ represents the Green's function from receiver 1 to receiver 2 (causal) and $G_{1,2}(-t)$ represents the Green's function from receiver 2 to receiver 1 (acausal). Equation (2.17) also contains two diverging integrals. These integrals show that all sources on the receiver line ($y = z = 0$) for $x < 0$ or $x > R$ contribute equally to the Green's function.

The diverging integrals can be handled in a few ways. Firstly we can consider a scenario where the sources are limited to the surface of a sphere centred in the middle of the receivers, as shown in [Boschi and Weemstra \(2015\)](#). The volume integral in 2.13 can then be replaced by a double integral over the surface of the sphere. As a result only the sources on the receiver line at the fixed radius of the sphere contribute to the Green's function so that there are no diverging integrals. Although this constraint succeeds in solving the diverging integrals, it is not realistic to expect the sources to be confined on the surface of a sphere

Another option, as shown in [Snieder \(2004\)](#), is to consider each of the sources as a scatterer that scatter an incoming wave from an external source (like an earthquake). Each scatterer acts as a secondary source, but waves can be multiply scattered on the way to the receivers. As a consequence, sources (or scatterers) close to the sensors on the receiver line ($y = z = 0$) are less likely to scatter and have a stronger contribution to the final solution than sources (or scatterers) far away that attenuates. To implement this, I introduce a scattering attenuation term in the Green's function in equation (2.6)

$$G_{1,s}(\omega) = \frac{1}{4\pi c} \frac{1}{\sqrt{2\pi}} \frac{\exp[-i\omega r_1^S/c]}{r_1^S} \left(\exp[-r_1^S/2L] \right), \quad (2.20)$$

where L is the attenuation length. If the same steps are followed and the stationary phase integrals solved, this gives

$$\frac{d}{dt}C(t) = \frac{-L}{2\pi} [G_{1,2}(t) - G_{1,2}(-t)]. \quad (2.21)$$

Equation (2.21) indicates that the seismic Green's function is related to the time derivative of the cross-correlation function. However, as shown in Roux et al. (2005b) for a finite bandwidth signal the cross-correlation function and its time derivative resemble each other so that the cross-correlation function is a good estimate of the seismic Green's function. The authors here also state that the time derivative could introduce undesired high frequency noise.

The mathematical derivation presented here shows that estimates of the causal and acausal Green's functions between two receivers can be obtained by cross-correlating data recorded in these receivers, if signals (from sources or scatterers) travel from all directions. The derivation relies on the stationary phase method, which states that only sources (or scatterers) located in the stationary phase locations contribute to the cross-correlation function.

A few assumptions are necessary for this proof to be valid. Firstly, for the cross-terms in the sum in equation (2.9) to be negligible, the sources (or scatterers) should be spatially and temporally uncorrelated, a large number of sources should be distributed around the receivers and we need to cross-correlate a long time series. The cross terms represent signals recorded in one receiver that are cross-correlated with signals recorded in the other receiver, when these signals are from different sources. In an industrial environment, these cross-terms could be problematic since some stable mechanical sources could be present in different locations. For instance in a mine there are many ventilation fans in the underground tunnels. The seismic signals from these fans are quite similar and spatially stable so that the influence of the cross-terms could therefore be non-negligible.

Unfortunately, when applying this method to real data we have little to no control over the temporal and spatial distribution of sources. However, some processing techniques can be used so that unfavourable spatial and/or temporal distributions of sources do not prevent the recovery of the Green's function. In practice, the recorded data is split into smaller sections and cross-correlated. All these cross-correlation functions are then summed (or stacked) to produce a cross-correlation function for the entire time series. This reduces the influence of cross-terms at longer lag-times and is analogous to equation (2.10). By splitting the data series in smaller sections, we can also speed up the recovery of the Green's function and reduce the influence of the cross-terms by using stacking and filtering techniques like adaptive covariance filtering (Nakata et al., 2015) or selective stacking (presented in the Section 6).

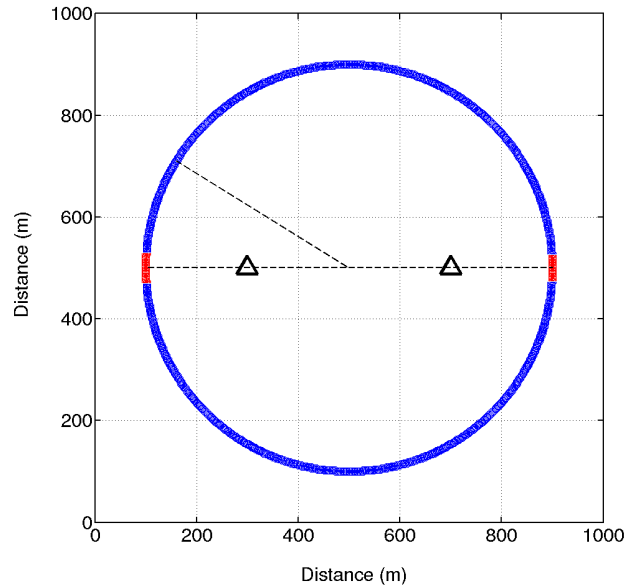


Figure 2.2 – Setup of the numerical simulation. The triangles indicate the locations of the sensors while the circles indicate the positions of the sources. The locations of the stationary phase locations, as described in the previous section, are shown in red.

Secondly, for the stationary phase approximation to be exact, the limit $\frac{\omega}{c} \rightarrow \infty$ or equivalently $\lambda \rightarrow 0$ has to be taken in equation (2.14). In real situations, this is of course not possible. Considering the rest of the exponent in (2.14), the parameter we need to consider for this approximation to be reasonable, is that the wavelength is much shorter than the distance between the sources and receivers. The error of the stationary phase approximation has been studied as a function of frequency in Zhan and Ni (2010) and a similar observation was made.

2.2.2 A numerical example

To illustrate the validity of the mathematical derivation even when all the conditions are not strictly met, I conducted a simple finite difference numerical simulation. Consider a situation where two seismic sensors in 2D are surrounded by seismic sources spread on circle so that all azimuths (θ) are represented between them. The scenario is depicted in Figure 2.2.

According to the mathematical derivation presented in the previous section, the stationary phase integral in equation (2.14) states that only the sources that are located in the stationary phase locations will contribute to the final solution for the integral. The simulation consisted of two sensors and 1000 sources placed around the two sensors so that all azimuths between the sensors were represented. One simulation was performed

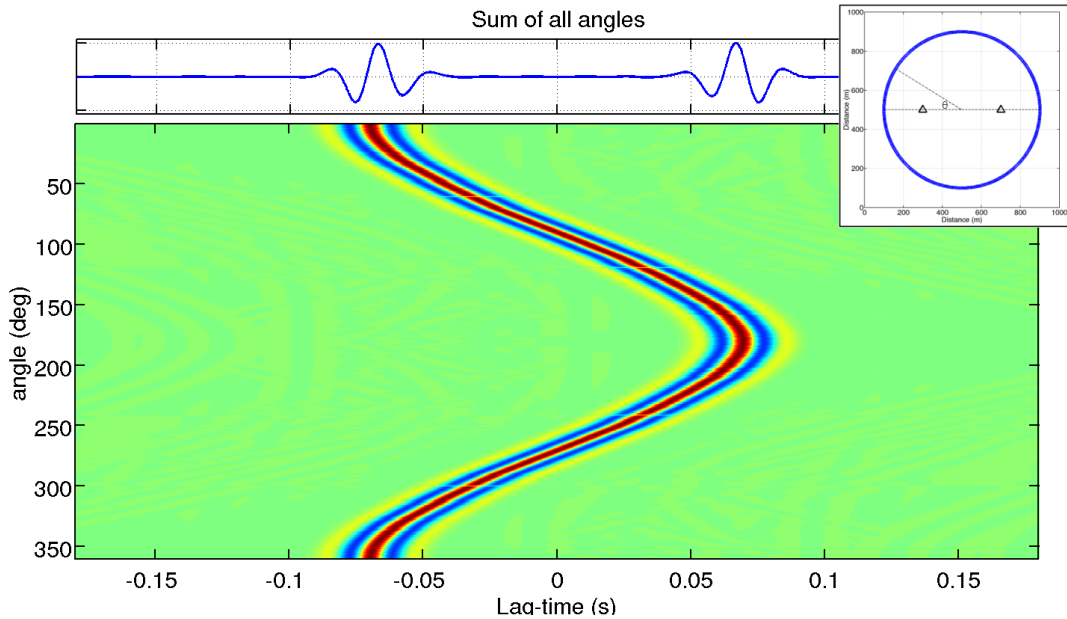


Figure 2.3 – The cross-correlation functions for each azimuth along with the sum of all azimuths. The sum of all azimuths represents the signal that would be recorded if one of the sensors are replaced by a source.

for each of the 1000 source locations and a Ricker-wavelet source was used for each simulation. Here, by performing a different simulation for each source location, the cross terms in (2.9) are automatically zero. The same result could have been achieved by randomly offsetting the sources in time and having an infinite number of sources (time/event averaging).

The cross-correlation functions for all azimuths are shown in Figure 2.3 along with the sum of all cross-correlation functions. Even though a finite number of sources were used in the simulation, from the sum of all azimuths it is clear that cross-correlation function at azimuths inbetween the stationary phase locations destructively interfere and only the sources located in stationary phase locations (0 and 180 degrees) remain.

Since the sources in non-stationary phase locations destructively interfere, the sum of the stationary phase correlation functions should be the same as the sum for all angles. A comparison of the two situations is shown in Figure 2.4. From the comparison, we see that the two sums produce approximately the same result. The difference in the two sums are due to the fact that only a relatively small number of simulations (1000) were performed.

The numerical example shows how the mathematical derivation of the underlying theory can be applied in practice if seismic signals are coming from all directions. Since the seismic signals in a mining environment are almost exclusively from human activity, it is probable that the locations of the seismic sources are confined to the mining tun-

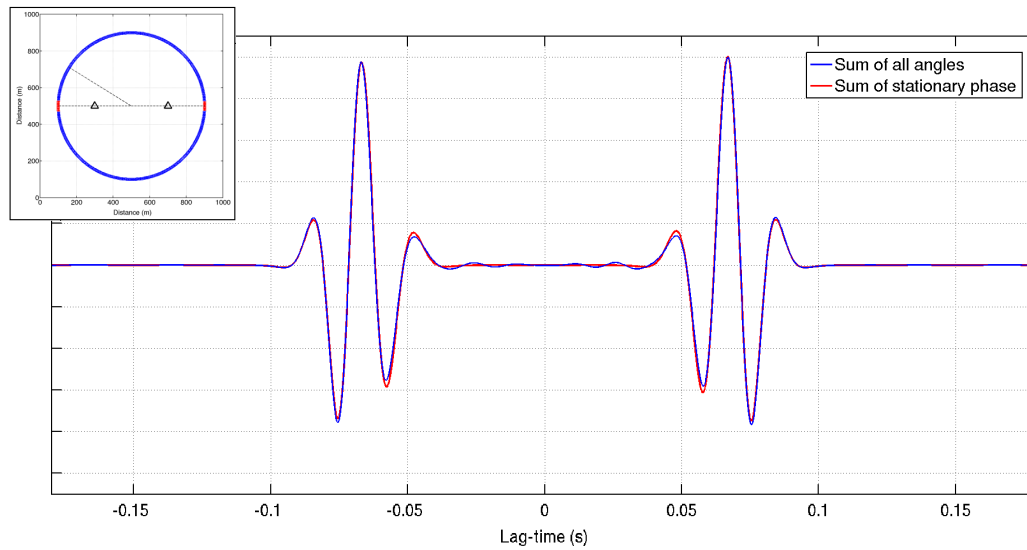


Figure 2.4 – A comparison of the sum of all azimuths and a sum of the cross-correlation functions when sources were located in stationary phase locations.

nels. In this case, it seems unlikely that sensors would be surrounded in all directions by seismic sources. However, according to the mathematical derivation, even if signals are not coming from all directions, we can still recover the seismic Green's functions as long as there are sources located in the stationary phase locations (close to receiver line). This attribute will prove to be useful in Chapter 6.

2.3 Ambient seismic noise

Ambient seismic noise refers to the continuous vibrations that are present in the earth at different frequencies. For a long time, it was believed that the seismic noise is nothing more than a nuisance and a lot of studies were devoted to minimising the seismic noise that was thought to only obscure useful signals from earthquakes or active sources. In pioneering work, [Aki \(1969\)](#) showed that the seismic noise carries information about the medium. Since then it has been shown that seismic noise consists of multiply scattered waves and, if processed carefully, can be used to illuminate and monitor the earth's interior at different scales.

The origin of these ambient vibrations depend on the wavelength considered. The longest period seismic noise (above 100 s) is often referred to as earth "hum". These long-period seismic waves have been attributed to atmospheric motion ([Tanimoto and Um, 1999](#); [Ekström, 2001](#)). More recent studies have attributed the seismic noise at these frequencies to a long-period ocean gravity wave ([Tanimoto, 2005](#); [Rhie and Romanowicz,](#)

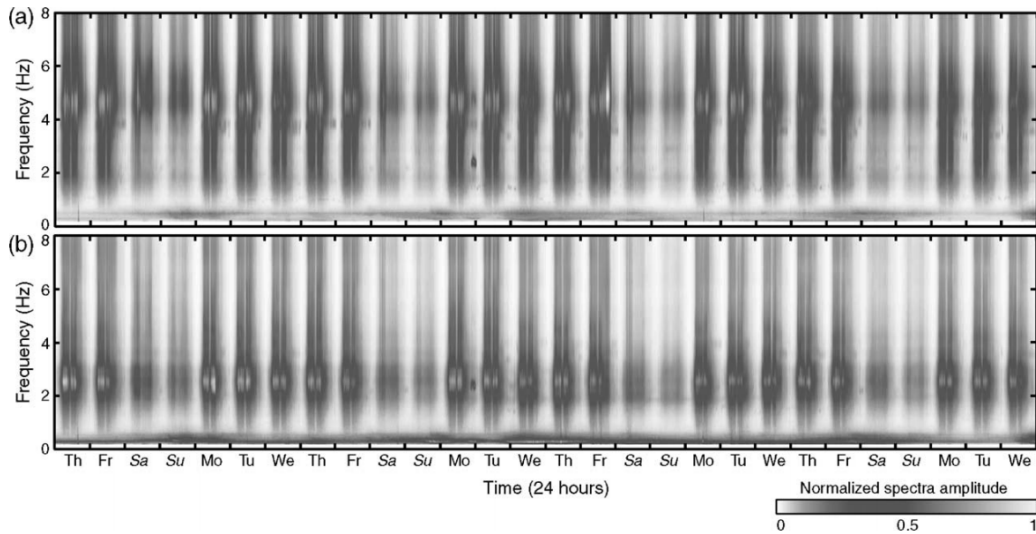


Figure 2.5 – Fourier spectra of the high-frequency noise for (a) vertical component and (b) north-east component recorded in an urban area (Grenoble, French Alps) from [Bonnefoy-Claudet et al. \(2006\)](#). The spectral amplitudes exhibit clear daily and weakly variations related to human activity.

[2004, 2006](#)).

Seismic noise in the period band between 5 to 20 seconds have been attributed to the interaction of the incoming ocean waves with the solid earth ([Webb, 1998](#)). The seismic noise in this band is referred to as oceanic microseisms. Within this band, there are two distinct peaks (at roughly 7 seconds and 14 seconds) that can be observed everywhere in the earth's crust. The origin of the primary microseism (14 seconds) is well understood and results from the direct interaction of the incoming ocean waves with the shallow sea floor ([Hasselmann, 1963](#)). The origin of the secondary microseism is less obvious and has been attributed to the non-linear interaction of the retracting ocean waves with the incoming ocean waves of the same frequency, which creates a compressional wave on the sea floor ([Longuet-Higgins, 1950](#)).

High frequency seismic noise with period below 1 second results mostly from anthropogenic sources and have daily and weekly variations linked to human activity (see Figure 2.5 from [Bonnefoy-Claudet et al., 2006](#)). The origins of the cultural noise include strong machinery, traffic and industrial activity. Since the high-frequency seismic waves attenuates relatively quickly, the dominant sources of seismic signal are very dependent on the location of recording. In [Bonnefoy-Claudet et al. \(2006\)](#), the authors note that the origin of seismic noise can be classified in frequency bands as follows: (1) Seismic noise below 0.5 Hz originates from oceanic and global meteorological conditions; (2) seismic noise between 0.5 and 1 Hz are from wind and local meteorological effects; (3) above 1 Hz the seismic noise is generated by human activity.

For seismic surface arrays used in crustal seismology, the interaction of the ocean with the solid earth provides stable ambient seismic noise coming from all azimuths that (mostly) satisfy the conditions necessary to reconstruct the seismic Green's function between two sensors by cross-correlating the signals recorded in them.

Chapter 3

Seismic velocities and coda-wave interferometry

Contents

4.1 Tomography	45
4.2 Monitoring changes in seismic velocity	47

In this chapter I will discuss the dependence of seismic velocity in rock on physical processes and show the method commonly used to measure small changes in seismic velocity.

3.1 Seismic velocities in rock

Seismic velocities can either be measured by passive or active methods in the earth's crust. Active methods are inconvenient, sometimes very expensive and have limited range. On the other hand, most passive methods (like travel time tomography with passive seismic events) can only measure velocity changes accurately enough to detect relative velocity variations of the order of 1 percent and with temporal resolution on the order of 1 month (Patanè et al., 2006), which are not accurate or frequent enough to detect processes associated with earthquake nucleation or relaxation. Over the last decade, it has been shown that the use of ambient seismic noise can bridge the gap between active and passive methods - it can enable us to make daily (or better) measurements of seismic velocity variations over long ranges without any extra instrumentation (eg. Brenguier et al., 2014). In this section I will briefly discuss the two main parameters driving the seismic velocity changes in the earth's crust.

The seismic velocities of rock are dependent on the elastic moduli, the stress (direction and magnitude) and fractures (density, orientation and saturation). For intact rock, only the stresses and fractures are likely to change. In this section I will briefly discuss

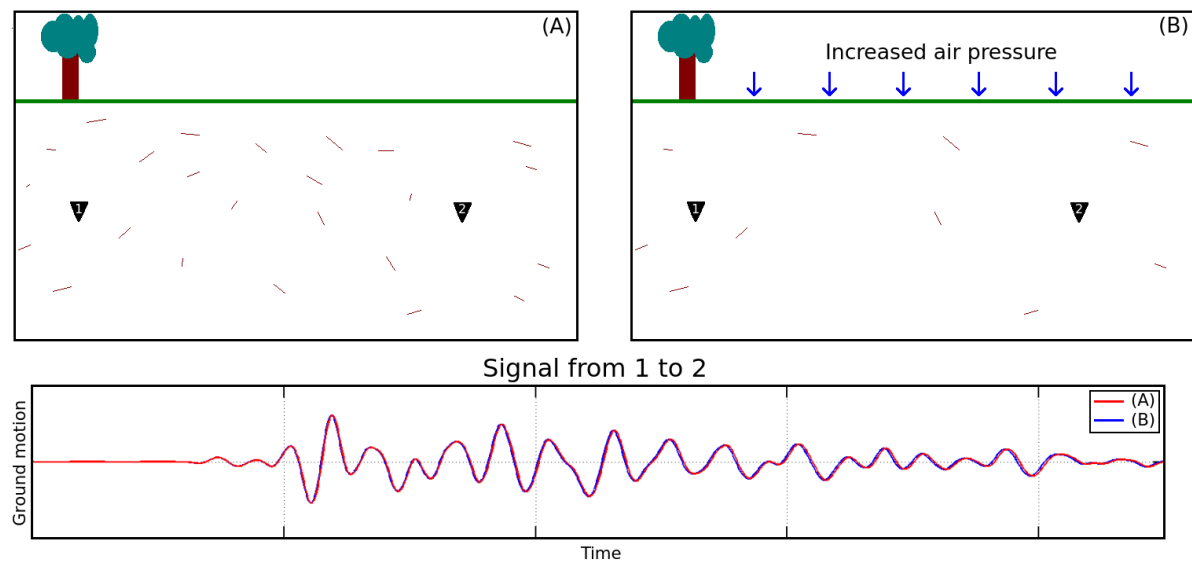


Figure 3.1 – Schematic showing how a change in pressure can cause a change in rock mass and seismic velocity. Here the increased atmospheric air pressure closes microcracks and results in a slight increase in velocity.

the dependence of seismic velocity on these two parameters.

3.1.1 Dependence on stress

The dependence of seismic velocity on applied stress has long been known (e.g. Birch, 1961; Nur and Simmons, 1969; Nur, 1971; O’Connell and Budiansky, 1974; Lockner et al., 1977). This effect has been observed in a variety of laboratory (Eberhart-Phillips et al., 1989; Verdon et al., 2008; Larose and Hall, 2009) and field studies (Fazio et al., 1973; Reasonberg and Aki, 1974; Leary et al., 1979; Yamamura et al., 2003; Silver et al., 2007). The dependence of the seismic velocity on stress differs for different rock types, but for a certain pressure range this relationship appears to be linear to a first order approximation (Eberhart-Phillips et al., 1989; Verdon et al., 2008; Larose and Hall, 2009).

There are two descriptions for the influence of changing stresses on seismic velocities. The first is the closing of microcracks which elastically stiffens the rock so that an increase in stress results in an increase in velocity and vice versa. A simple illustration of this description is shown in Figure 3.1, where an increase in atmospheric air pressure closes microcracks and thereby increases the seismic velocity. This description is very intuitive, but hard to formulate and implement mathematically.

The second description comes directly from third-order elasticity theory (Murnaghan, 1951), where the seismic velocities can be expressed in terms of isotropic strain and elastic

moduli as

$$V_p = \sqrt{\frac{\lambda + 2\mu + \frac{1}{3}(7\lambda + 10\mu + 6l + 4m)\theta}{\rho_0}}. \quad (3.1)$$

and

$$V_s = \sqrt{\frac{\mu + (\lambda + 2\mu + m - n/6)\theta}{\rho_0}}. \quad (3.2)$$

where θ is the volumetric strain, λ and μ are the second-order elastic moduli (or Lamé's constants), and l , m and n are the third-order elastic moduli (or Murnaghan constants). The difference between the expressions for the P- and S-wave velocities shown here and in (2.3) are from the contributions of the third-order terms of the strain energy function, which were neglected in (2.3). As shown in Aoki (2015) in the absence of damage from dynamic stress perturbations, change in seismic velocity due to infinitesimal change in isotropic strain can be approximated by

$$\frac{1}{V_p} \frac{dV_p}{d\theta} = \frac{7\lambda + 10\mu + 6l + 4n}{6(\lambda + 2\mu)}. \quad (3.3)$$

and

$$\frac{1}{V_s} \frac{dV_s}{d\theta} = 2 + \frac{\lambda + m - n/6}{2\mu}. \quad (3.4)$$

This description can be used relatively easily to estimate the response of the seismic velocities to strain changes, but no physical interpretation of the moduli have been formulated so that their values are hard to estimate (Aoki, 2015). Tsai (2011) modeled the expected velocity change from the thermoelastic and poroelastic strain changes with reasonable values of the third-order elastic constants to investigate if seasonal variations in seismic velocity observed by Meier et al. (2010) in southern California can be explained by this theory. Here the author found that the observed velocity variations are generally too large to be explained by third-order elasticity theory so that another mechanism was probably responsible for the velocity variations. Although it is hard to determine which one of the two descriptions best describes the susceptibility of seismic velocity to stress change, knowing the exact mechanism is not strictly necessary for the purposes of this dissertation.

The influence of stress on seismic velocity, along with the fact that earthquakes are initiated by accumulating tectonic stress, has for a long time lead researchers to believe that accurate measurement of time dependent seismic velocity variations could potentially be a method to predict earthquakes (Whitcomb et al., 1973; Mjachkin et al., 1975). Seismic velocity variations have been reported prior to a few large earthquakes (Niu et al., 2008; Lucente et al., 2010), but more results are needed for the correlation to be convincing.

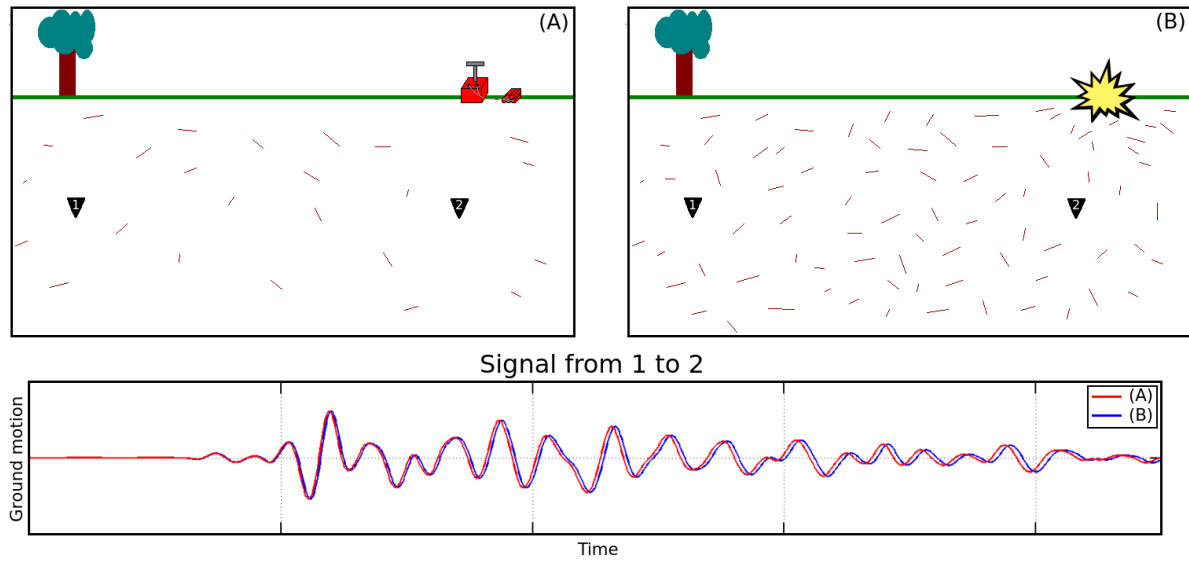


Figure 3.2 – A schematic showing how a sudden dynamic stress perturbation (like a blast) can cause a change in the rock mass and seismic velocity. Here the blast induces damage and opens microfractures so that the velocity decreases.

3.1.2 Dependence on damage

The linear relation between stress and seismic velocity is not always valid. In the presence of a sudden dynamic stress perturbation, like an earthquake or a blast, the rock responds in a very complex and non-linear fashion. In this scenario, the dynamic stress perturbation causes a sudden decrease in velocity followed by slow relaxation. These observations have been made in laboratory studies and is referred to as anomalous non-linear fast dynamics and slow dynamics (Johnson and Sutin, 2005). This has also been observed in numerous crustal studies, specifically in relation to damage from large earthquakes (Brenguier et al., 2008a; Wegler et al., 2009; Cheng et al., 2010; Taira et al., 2015). Damage here could refer to motions at grain joints or the opening of microfractures. A simple illustration of this is shown in Figure 3.2. Recently, non-linear damage rheology models have been developed to explain such behaviour (Lyakhovsky et al., 2009). It is also possible that the short-term velocity decrease prior to volcanoes are related to this non-linear effect (Brenguier et al., 2011).

Both the linear and non-linear behaviour of rock in response to stress changes are of interest in a mining environment - this will be discussed in Chapter 5. For example, accurate measurements of damage induced by development blasts or induced earthquakes, a non-linear behaviour, can help determine the influence range of these events and time dependent relaxation can be used to determine re-entry times. Measurements of stress change, a linear behaviour, can be used in conjunction with conventional passive seismic monitoring to determine seismic hazard as a function of space and time.

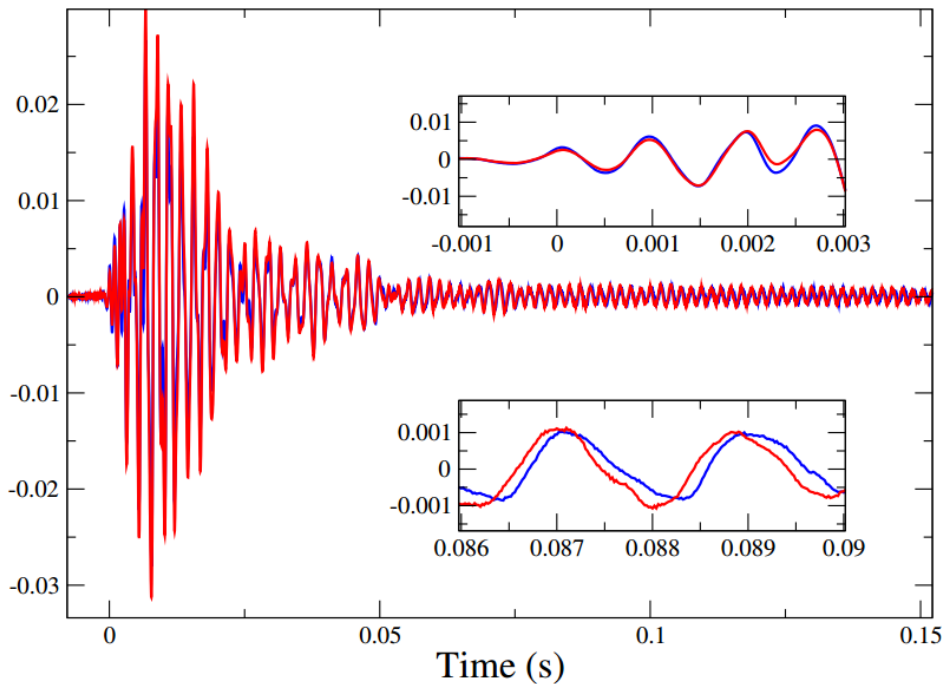


Figure 3.3 – Two hammer shots recorded in a mining pillar after the stress was changed, from Grêt et al. (2006). The change in the medium is not visible in the direct arrival, but clearly visible in the coda.

Although the non-linear effects of a dynamic perturbation on the seismic velocities have been shown with ambient seismic noise for a number of studies, to my knowledge changes in static stress have not been observed.

3.2 Coda-wave interferometry

In this section, I will briefly discuss the method that is commonly used to measure small changes in seismic velocity. Coda is the Italian word for "tail" and coda-waves refer to the multiply scattered waves that arrive after the direct waves. For a long time it was thought that extracting useful information from coda waves was impossible. This was changed by the pioneering work of Keitii Aki, which showed that the coda-waves contain information of the local medium that is independent of the source (Aki, 1969; Aki and Chouet, 1975).

Since the coda waves are multiply scattered between source and receiver, they sample the medium for much longer intervals than the direct waves. As a result, the coda-waves are very sensitive to changes in the medium and can illuminate changes in the medium that can not be observed from the direct arrivals. This is shown in Figure 3.3 for two

hammer shots in a mining pillar after the stress in the pillar was increased (Grêt et al., 2006). In Figure 3.3, we can clearly see the effect of the change in the medium in the coda part of the wave, even though the direct arrival appears unchanged.

This attribute of coda-waves have been used in recent years along with repeating sources (highly similar earthquakes or active sources) to measure small changes in seismic velocity (Wang et al., 2008; Wegler et al., 2009; Kanu et al., 2014; Sawazaki et al., 2015). The method is referred to as coda-wave interferometry (CWI). For a mathematical description of the method, I refer the reader to Snieder (2006).

In recent years, it has been shown that reconstructing the late part of the seismic Green's functions with ambient seismic noise correlations, is less dependent on the seismic source distribution than the direct arrivals (Colombi et al., 2014). This means that the late part of the cross-correlation functions (or the coda) converges to the seismic Green's function faster than the direct arrivals. Hadziioannou et al. (2009) have also shown that the fully converged Green's functions are not needed to measure changes in seismic velocity. Here the authors showed that the phase information of the Green's function is retrieved much faster than the amplitude information. Therefore the velocity variation measurements can be made in the coda even if the cross-correlation function has not converged to the seismic Green's function. Since the coda of the cross-correlation function is very stable, can be retrieved relatively fast and is not very dependent on the seismic source distribution, CWI is a very applicable method to measure velocity variations in cross-correlation functions from ambient seismic noise.

Part II

Applications

Chapter 4

Past applications in crustal seismology

Contents

5.1	3D Seismic velocity models	52
5.1.1	Imaging the subsurface	52
5.1.2	Accurate microseismic event locations	54
5.2	Monitoring velocity variations	54
5.2.1	Measuring stress changes	54
5.2.2	Measuring damage and relaxation for re-entry protocols	55
5.2.3	Monitoring slope stability in open pit mines	56

In this chapter I will show examples where the Green's functions retrieved from seismic interferometry has been used to deduce physical properties of the earth's crust. I will group these applications in two categories: tomography and monitoring. A review of the past applications in these categories can be useful, since these are two applications that I identified to be useful in a mining environment.

4.1 Tomography

[Shapiro and Campillo \(2004\)](#) were the first to show that Raleigh waves emerge from the correlation of ambient seismic noise coming from the oceanic microseisms. Shortly after this discovery, the potential applications of this method started to become clear with two studies showing how this method can be used to construct high-resolution images of the upper crust of California ([Shapiro et al., 2005](#); [Sabra et al., 2005a](#)). This started a revolution in seismology: there was no longer a need for inconvenient controlled seismic sources to image and monitor the earth at different scales, instead we can turn each sensor into a virtual seismic source. This happened at a time when the deployment of

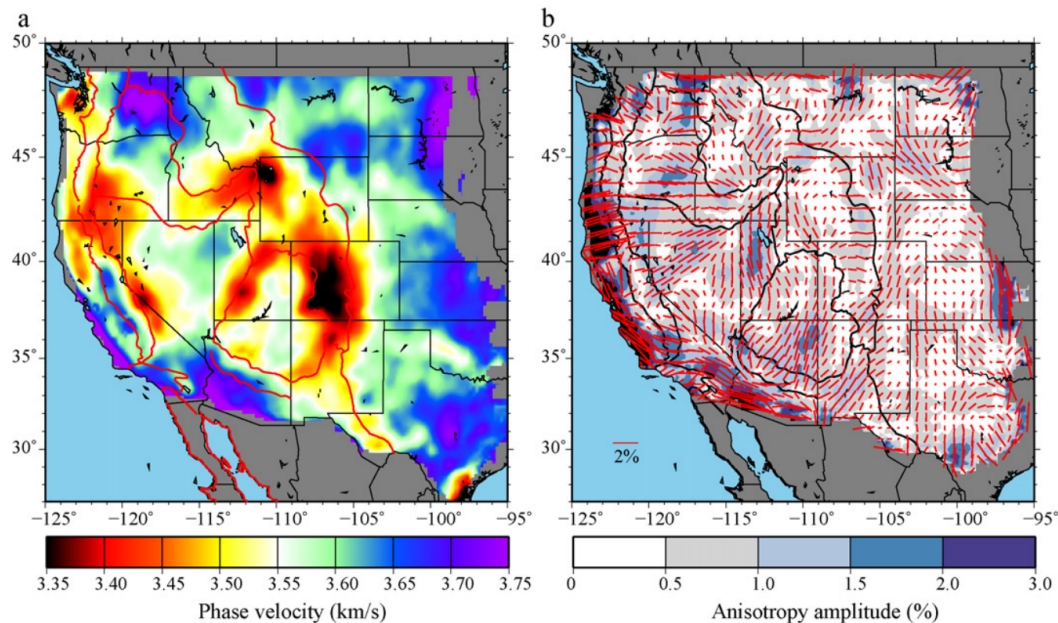


Figure 4.1 – (a) Raleigh wave isotropic phase speed map from ambient seismic noise and, (b) amplitude and fast direction of the Raleigh wave phase velocities from [Ritzwoller et al. \(2011\)](#).

large seismic arrays (like USArray) became more and more prevalent.

Since the first images of the crust of California were created with ambient seismic noise, there have been a multitude of studies using ambient seismic noise to image the earth. It became apparent that the method is very well suited to dense seismic arrays. [Yang et al. \(2007\)](#) used 125 broadband stations to create Raleigh wave images across Europe. [Lin et al. \(2008\)](#) used more than 250 sensors from the transportable component of the USArray and applied the method to the western United States with unprecedented resolution. [Ritzwoller et al. \(2011\)](#) used more than 1000 stations from the USArray to create Raleigh wave phase velocity and anisotropy maps (see Figure 4.1). Recently, [Nakata et al. \(2015\)](#) used a network of about 2500 sensors with 100 m spacing to extract body waves and image the subsurface in Long Beach, California with higher accuracy than was previously possible with surface waves. Since the body waves are harder to extract than the surface waves ([Forghani and Snieder, 2010](#)), the authors used a filter that selected time periods with strong body waves coming from local traffic.

Although the majority of the ambient noise tomography studies in the literature were conducted with regional seismic surface arrays, there are a few notable examples where ambient seismic noise imaging was performed in smaller scale environments. [Brenquier et al. \(2007\)](#) applied the method to Piton de la Fournaise volcano on Reunion island to create a 3D S-wave velocity model of the region surrounding the volcano and succeeded in imaging the magma chamber. Similar studies have since been performed at other

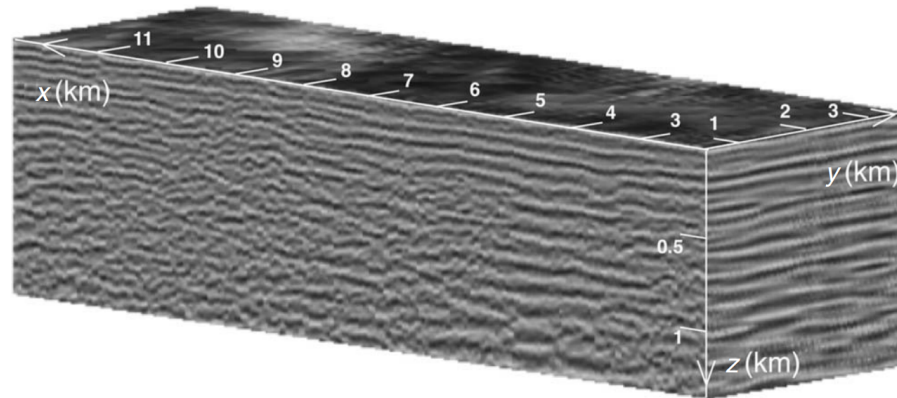


Figure 4.2 – 3D reflection image of the Sirte basin created with ambient seismic noise correlations, from [Draganov et al. \(2009\)](#). The horizontal lines indicate discontinuities in the crust.

volcanoes, for instance Yellowstone ([Seats and Lawrence, 2014](#)). [Draganov et al. \(2009\)](#) used ambient seismic noise recorded along 8 parallel lines in the Sirte basin to construct a migrated reflection image of the subsurface, showing the promise the method has to be used in seismic exploration (see Figure 4.2). [Nakata and Snieder \(2011\)](#) showed that the seismic noise generated by traffic can be used to perform small scale shear wave imaging.

Although ambient noise tomography has not been applied in a mining environment, the small scale applications and the applications where the noise from local traffic was used, are encouraging signs that the method could be applied in a mining environment.

4.2 Monitoring changes in seismic velocity

If I am able to construct the seismic Green's function between sensors, this process could be performed regularly so that I essentially have a repeatable source. If I use these repeatable sources with CWI (discussed in Section 3.2), it could enable me to detect very small changes in the seismic velocity in the medium. In this section I will show examples where ambient seismic noise was used exactly in this way - as a repeatable virtual seismic source.

By using ambient seismic noise and CWI, [Wegler et al. \(2009\)](#) detected a sudden 0.6% decrease in seismic velocity following the M6.6 Mid-Niigata earthquake. Here the authors interpreted the decrease in seismic velocity as a decrease in stress in the earth's crust due to the earthquake. Similarly, [Brennguier et al. \(2008a\)](#) used ambient seismic noise correlations to measure the response of the crust to the M6.0 Parkfield earthquake. This study showed that the earthquake caused an immediate decrease in the seismic

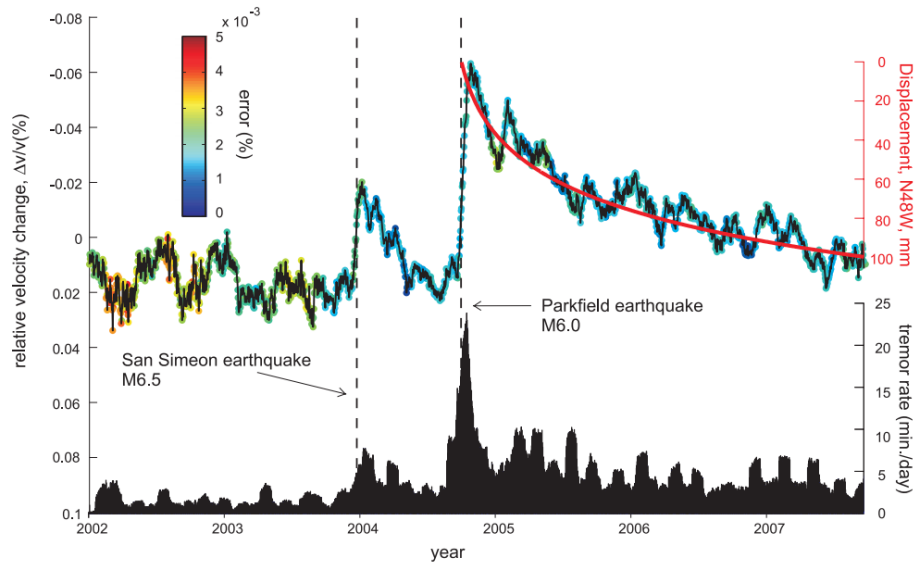


Figure 4.3 – Seismic velocity changes during the M6.0 Parkfield earthquake measured with ambient seismic noise, as reported in [Breguier et al. \(2008a\)](#).

velocity followed by a slow relaxation. In this paper, the authors attributed the decrease in velocity to the damage and fracturing caused by the dynamic strain wave from the earthquake. An interesting finding in the study was that the seismic velocities take more than 4 years to return to the values they were before the earthquake. The results of the study show the non-linear behaviour of the seismic velocities to stress perturbations that has also been observed in laboratory studies ([Johnson and Sutin, 2005](#)).

[Sens-Schönfelder and Wegler \(2006\)](#) used seismic interferometry to measure seismic velocity on a daily basis up to 0.1% accuracy at Merapi volcano. The authors detected strong seasonal variations of the seismic velocities which they described with a depth dependent hydrological model. Seasonal variations in seismic velocity have since also been detected in the Los Angeles basin and San Jacinto fault area with ambient seismic noise ([Meier et al., 2010](#); [Hillers et al., 2015a](#)). [Breguier et al. \(2008b\)](#) showed the potential of using ambient seismic noise to forecast volcanic eruptions. The paper showed that there was a notable systematic short-term decrease in seismic velocity prior to volcanic eruptions, which the authors related to the dilation of a part of the volcanic edifice as a result of magma pressurisation.

Recently, a new method of imaging the earth's interior with ambient seismic noise has been developed. This method relies on monitoring changes in the seismic velocity and comparing these changes to expected (or measured) strain changes ([Breguier et al., 2014](#)). In this study, the authors measured seismic velocity variations with the dense (more than 900 stations) Japanese Hi-net seismic network during the M9.0 Tohoku-Oki earthquake. A comparison of the measured velocity change and the expected strain

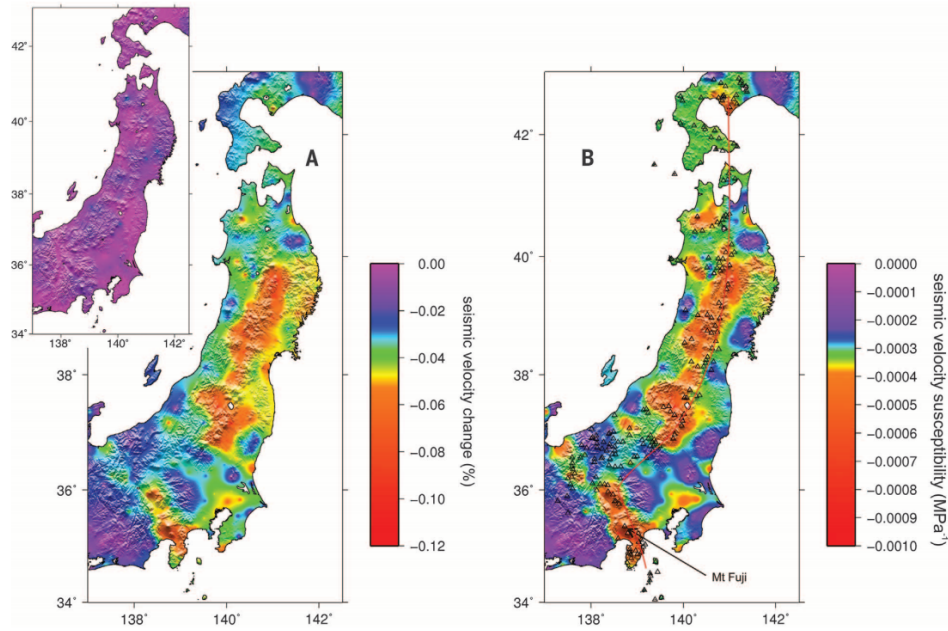


Figure 4.4 – (A) Image of the instantaneous seismic velocity change in Japan due to the M9.0 Tohoku-Oki earthquake and (B) seismic velocity susceptibility, determined by the seismic velocity response compared to the dynamic strain change from the earthquake. Figure from [Brenquier et al. \(2014\)](#).

change from the earthquake, show the susceptibility of the seismic velocities to strain changes (see Figure 4.4). This imaging method clearly illuminated the Japanese volcanic front, which indicated that areas with high pore-pressure are more susceptible to dynamically-induced seismic velocity change than others.

Most of the applications where ambient seismic noise has been used to monitor velocity variations were either during large earthquakes or volcanic eruptions. There are other areas where ambient seismic noise correlation have been used to monitor seismic velocity variations, including geothermal reservoirs ([Hillers et al., 2015b](#); [Obermann et al., 2015](#)) and mud landslides ([Mainsant et al., 2013](#)). The diverse environments where ambient seismic noise correlations have been used to monitor seismic velocity variations are encouraging and indicate that the same method could be useful in mines.

Chapter 5

Potential applications in a mining environment

Contents

6.1	Introduction	62
6.2	Numerical simulations	64
6.2.1	Creating a realistic model	66
6.2.2	Scattering caused by mining excavations	67
6.2.3	Influence of source-receiver distance on scattering regime	70
6.3	Data	70
6.3.1	Examining scattering properties with microseismic events	71
6.4	Ambient noise cross-correlations	74
6.4.1	Stationary phase locations	74
6.4.2	Monochromatic sources	74
6.4.3	Selective stacking	75
6.4.4	Directional bias from non-isotropic wavefields	80
6.4.5	Convergence of cross-correlation functions to the seismic Green's functions	80
6.4.6	Frequency content of the cross-correlation functions.	82
6.4.7	3D S-wave velocity model	83
6.5	Conclusions	85
6.6	Appendix A	88
6.6.1	Inversion of the mean-free-path	88
6.7	Appendix B	89
6.7.1	Determination of S-wave arrival with kurtosis estimator	89
6.7.2	3D Tomography	90
6.7.3	Checkerboard resolution test	92

The previous applications of ambient seismic noise correlations in crustal seismology led me to a discussion of the potential applications in a mining environment in this

chapter. The potential applications in mines serve as motivation for this project.

5.1 3D Seismic velocity models

In the previous chapter, it was shown that the direct waves in the reconstructed Green's functions can be used to create 3D velocity models of the subsurface. If I am able to construct the Green's functions in mines, this would enable the construction of 3D velocity models and a number of useful applications would follow. In this section I will briefly discuss some of these applications.

5.1.1 Imaging the subsurface

The ability to accurately image the deep subsurface below a mine and create accurate 3D models of mineral resources could cause a dramatic decrease in the cost of production and improve output. To image the subsurface, the mining industry uses a variety of geophysical methods, like electromagnetic, magnetic and gravimetric surveys. Unfortunately, as mines are getting deeper the depth of penetration and the resolution of these methods have been found wanting.

A commonly used mineral exploration technique for existing mines is analysing drill core samples. This involves drilling long exploration holes into future mining areas and retrieving the drill cores to identify mineral deposits. This method is attractive since the samples are easy to analyse, but only provides localised measurements and is extremely expensive.

The potential of using seismic surveys for mine planning have been known for a long time and a few notable studies have been published (see Figure 5.1), but unlike the oil and gas industry the mining industry has been slow to adopt it. This is partly because of the costs involved in a high-resolution survey and partly because other geophysical methods have been adequate for the shallow depths involved in early mining projects. For a review on the seismic methods used in the mineral exploration industry, see [Malehmir et al. \(2012\)](#). The difficulty of applying seismic imaging could be due to the relatively low acoustic impedance contrast between ore-bodies and host rock, which makes the reflections from ore-bodies weak and hard to identify. Additionally, the presence of strong scatterers in the form of mining tunnels and voids can make the task of identifying weak reflections from ore-bodies even more difficult ([Ahmadi et al., 2013](#)). It is interesting to note that the strong scattering caused by the mining structures that makes it difficult to use conventional seismic imaging from the surface, will eventually aid in reconstructing the seismic Green's function at depth in Chapter 6.

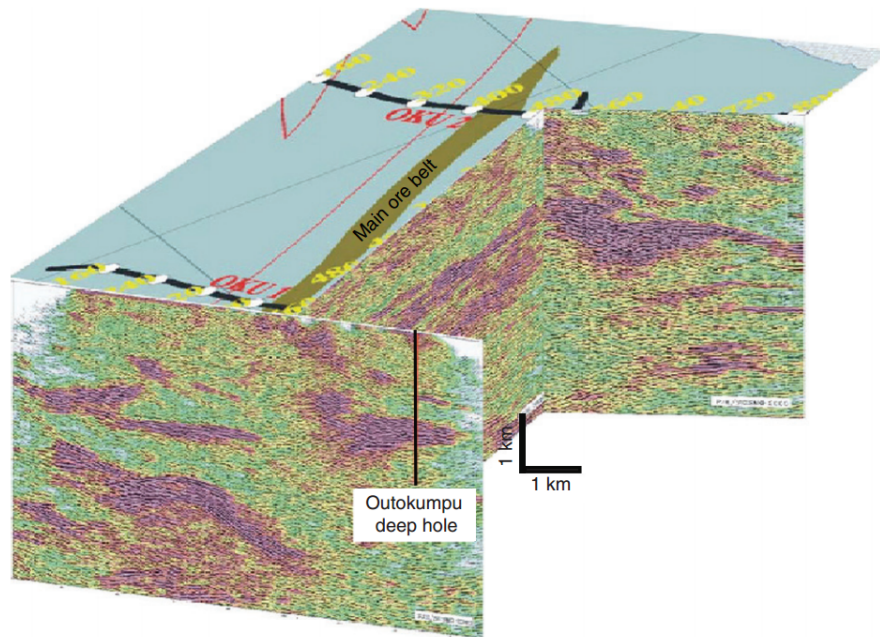


Figure 5.1 – Seismic surveys at the Outokumpu sulfide deposits in Finland taken from [Kukkonen et al. \(2011\)](#). The strong reflectors here are from an ophiolite unit that hosts the sulfide mineralisation.

Passive seismic imaging with recorded microseismic events recorded in a mine has also been investigated in a number of studies ([Jackson et al., 1995](#); [Friedel et al., 1995, 1996](#); [Scott et al., 1996](#)). The main constraint of this method is the unknown location and initiation time of the microseismic event, which decreases the accuracy of the method. Additionally, we have little control over the locations of the microseismic events so that high resolution imaging with this method is not guaranteed. This can be circumvented by using a controlled active source, where we have control over the location, initiation time and coverage ([Cai et al., 2014](#)). However, active seismic sources can be expensive and have limited range.

During my PhD project, I investigated whether virtual seismic sources (created by cross-correlating ambient seismic noise) can be used as a complimentary technique to image the subsurface in a mining environment. Essentially, each of the virtual seismic sources would be used as an active source. With this method, existing seismic sensors can be used along with data that would normally be discarded, potentially reducing the costs involved in conventional seismic imaging. The exact start times and locations of the virtual seismic sources are also known, so that these sources can potentially give more accurate results than passive imaging with microseismic event sources.

5.1.2 Accurate microseismic event locations

At present, it is common for mines with microseismic monitoring systems to use homogeneous velocity models to locate microseismic events (Mendecki, 1997). Creating inhomogeneous 3D velocity models and using methods like ray-tracing could enable more accurate microseismic event locations (Lurka and Swanson, 2009; Spottiswoode and Linzer, 2005). Accurate microseismic event locations are important to identify spatial clustering of events that could indicate fault zones or areas with increased seismic risk. Furthermore, it has been shown that the spatial clustering of microseismic events achieved with 3D velocity models can enable the tracking and migration of cave fronts (Lynch and Lotter, 2007; Sewee et al., 2008).

By creating an accurate inhomogeneous 3D seismic velocity model of the underground mining environment with ambient seismic noise, it can enable more accurate locations of microseismic events, improving the overall usefulness of mine seismology.

5.2 Monitoring velocity variations

As shown in Section 3.1, the seismic velocities of solid rock in a mining environment are dependent on stress and damage. Therefore, accurately measuring small changes in the seismic velocity would enable me to monitor the time dependent changes in these parameters. This method has been attempted by a few studies in mines with active sources or earthquakes (Maxwell and Young, 1992; Huang et al., 2013; Westman et al., 2012; Luxbacher et al., 2008; Grêt et al., 2006), but to my knowledge not with ambient seismic noise. Monitoring these parameters accurately could be of great use in mines, and below I discuss a few potential applications.

5.2.1 Measuring stress changes

Currently stress meters, borehole strain cells, gauges, etc. are used in mines to determine the values of stress and deformation in different areas in the mine (Fairhurst, 2003). However, many of these measurements are very localised in space and can be plagued by site effects. Additionally, most of these methods are not practical to implement regularly.

It is well known that seismic velocities of rock are sensitive to applied stress (see 3.1). Unfortunately, the susceptibility of seismic velocity to stress change is very low - of the order of $10^{-8}/\text{Pa}$ (see table in Yamamura et al., 2003). Therefore, in order to measure kPa level stress changes, seismic velocities need to be measured with up to 0.001% accuracy. Some studies have attempted to measure the changes in seismic velocity due to changes in stress with microseismic events (Maxwell and Young, 1992; Westman et al., 2012) or active sources (Grêt et al., 2006; Huang et al., 2013) to evaluate the response of the rock to mining activities (see for example Figure 5.2), but have not been able to

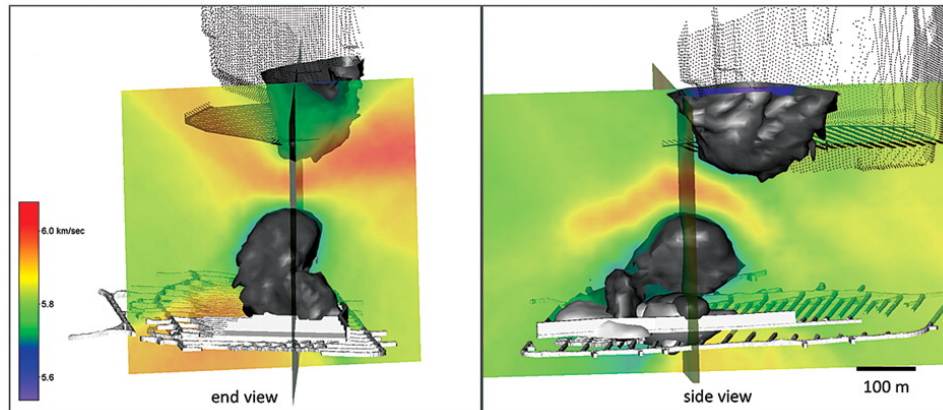


Figure 5.2 – Figure from [Westman et al. \(2012\)](#) showing velocity contours from double-difference tomography around caved regions indicating the redistribution of stresses.

reach the desired level of accuracy.

If virtual seismic sources can be used to regularly measure small changes in seismic velocity, it can provide information about how stresses are evolving as a function of time. Since the rate of microseismic activity in mines can be controlled to a certain degree ([Mendecki, 1997](#)), it could be possible to evaluate the evolution of stress and plan mining activities accordingly and ultimately improve safety.

During my PhD project, I investigated whether changes in seismic velocity can be used to monitor kPa level stress change on an hourly basis in a mine. This is shown in Chapter 7, where I investigate the influence of a blast in the mine on the local stress distribution by accurately measuring seismic velocity variations.

5.2.2 Measuring damage and relaxation for re-entry protocols

Another mechanism by which seismic velocities can change, is by damage - the opening of microfractures or motions at the grain joints. As shown in the previous section, a large dynamic stress perturbation, like a large earthquake or a blast, can damage the surrounding rock and cause a sudden decrease in seismic velocity. After the dynamic stress perturbation has damaged the rock, the confining static stress can "heal" the rock by systematically closing the fractures ([Brenquier et al., 2008a](#)). In some cases, it has been shown that the seismic velocities can take years to return to the original value (see Figure 4.3).

Currently the most common parameter used for re-entry times in mines after blasts or earthquakes is the microseismic event activity rate with Omori's law ([Vallejos and](#)



Figure 5.3 – Photo of the landslide that occurred at Bingham Canyon mine (Ravell Call, Deseret News, 2013)

McKinnon, 2010). I believe that the damage and relaxation of the rock, as indicated by seismic velocity variations, could be an alternative method to examine re-entry times in mines. In Section 7, I will compare the aftershock activity rate with the relaxation of the seismic velocities after a blast and show that the seismic velocity is a more sensitive parameter than aftershock activity rate and has the potential to be used as an alternative method to determine re-entry times after large blasts or seismic events.

5.2.3 Monitoring slope stability in open pit mines

In open pit mines, landslides are very serious threats. This was illustrated by the landslide that occurred at the Jiama copper and gold mine in Tibet in 2013 that cost the lives of 83 workers. A potentially lethal landslide also occurred at Bingham Canyon open pit mine in 2013 (see Figure 5.3). Bingham Canyon has a monitoring network consisting of radar, laser, gps and seismic sensors. As a result, they were able to detect slope movement and evacuate the mine roughly 12 hours before the landslide and no fatalities or injuries occurred.

Recently, it has been shown that ambient seismic noise can be used to monitor areas prone to mud landslides (Mainsant et al., 2013). In this study the authors showed that there was a significant velocity decrease that started roughly 4 days prior to the Port Bourquin landslide in Switzerland. Due to the similarity in these two settings, I believe that this indicates that monitoring seismic velocity variations can give open pit mines

an additional tool to monitor pit walls that might be prone to failure. Since many open pit mines already have seismic monitoring networks in place, they have the ability to implement this method for relatively low costs as no extra hardware would be required.

Part III

Reconstruction of seismic Green's function

Chapter 6

Seismic interferometry with mining noise

Contents

7.1	Preliminary methods and parameters	98
7.1.1	Determining window for measuring velocity variations	98
7.1.2	Calculation of relative velocity variations	98
7.1.3	Inversion for time dependent velocity changes	100
7.2	Introduction	102
7.3	Data and methods	104
7.4	Results	108
7.5	Conclusions	111

A crucial aspect of my project was to determine whether the seismic noise induced by mining activity could be used to construct the seismic Green's function between underground short-period sensors. This proved to be a difficult task, since the noise generated by mining activity is not well suited to apply the standard methodologies developed in crustal seismology. My first published paper addressed these issues.

Body-wave reconstruction from ambient seismic noise correlations in an underground mine

Gerrit Olivier, Florent Brenguier, Michel Campillo, Richard Lynch, Philippe Roux

Geophysics, VOL. 80, NO. 3 (MAY-JUNE 2015); KS11 KS25,
10.1190/GEO2014-0299.1

Abstract: The reconstruction of seismic Green's functions from correlations of ambient seismic noise recently developed as a promising approach for exploring the Earth's interiors without the requirement of costly active seismic sources. This approach has been widely employed for imaging the crust at a kilometer scale. However, few studies report noise-based Green's functions reconstruction at smaller scales in industrial environments. In this study, we investigate the possibility of constructing seismic Green's functions between sensors in an active underground mine (Garpenberg, Sweden) by cross-correlating seismic noise generated by mining activities. We show with realistic numerical simulations that the mining excavations in an underground mine leads to a regime of strong scattering, which is favorable for constructing seismic Green's functions by cross-correlating seismic noise. One month of continuous data was recorded by 18 seismic sensors located more than 1 km below surface. A variety of broadband (10 - 3000 Hz) seismic sources are present, but the seismic wavefields are directional and often monochromatic, so that the conditions for constructing Green's functions by cross-correlating ambient seismic noise are not ideal (isotropic illumination and spectrally white). We developed a stacking scheme that dismisses data during periods when the seismic noise is dominated by monochromatic signals or when noise sources are not in stationary phase locations. Estimates of the seismic Green's functions were retrieved for a broad frequency range (20 - 400 Hz) for almost all of the correlation pairs when we used the selective stacking scheme. We used the direct body-waves present at low frequencies (below 100 Hz) in the reconstructed seismic Green's functions to invert for the 3D S-wave velocity structure of the mine. The results show the existence of a high and low velocity zone that corresponds with known ore bodies.

6.1 Introduction

Cross-correlating ambient seismic noise can be used to construct seismic Green's function between sensors pairs, effectively turning one of the sensors into a virtual source (Shapiro and Campillo, 2004; Campillo, 2006; Sabra et al., 2005b; Stehly et al., 2008).

Over the last decade Green's functions, constructed by cross-correlating ambient seismic noise, have been predominantly used to image the upper crustal structure of the earth (Shapiro et al., 2005; Moschetti et al., 2007; Sabra et al., 2005a; Boué et al., 2014;

Lin et al., 2013a,b). The vast majority of ambient noise tomography studies have been performed with surface waves, since the sensor arrays used for these studies are located at surface and the seismic noise is dominated by the surface waves emanating from the interaction of the ocean with the solid earth (Webb, 1998). Constructing body waves by cross-correlating ambient seismic noise has proven to be much more difficult (Forghani and Snieder, 2010), but there are a few notable examples where body waves have been extracted from ambient seismic noise (Nakata and Snieder, 2011; Roux et al., 2005a; Zhang et al., 2009; Boué et al., 2013).

To construct full Green's functions between sensors by cross-correlating seismic noise, sensors should be surrounded in all directions by a large (theoretically infinite) number of spectrally white sources (Lobkis and Weaver, 2001) or spectrally white sources should only be located in stationary phase locations (Roux and Kuperman, 2004). The stationary phase locations of a sensor pair refer to the conical areas behind each sensor pointing toward the other. An isotropic seismic wavefield and a directional seismic wavefield can produce the same cross-correlation function - for isotropic wavefields, signals not coming from stationary phase locations destructively interfere so that only signals from sources located in stationary phase locations contribute to the cross-correlation function (Gouedard et al., 2008). This property is useful for small scale and high frequency applications where local sources strongly contribute to the seismic wavefields so that the resulting seismic wavefields are not isotropic.

Currently, most mines with seismic monitoring networks only use a small fraction of the recorded vibrations - in the form of microseismic events - while all other data are discarded. Although a large number of these microseismic events are recorded in a given day, using them to examine the properties of the surrounding medium is difficult since the exact location and start time of these events are unknown. This means prior information about the seismic velocities have to be used to determine the start time and location of the events. These same events are then used to try and iteratively improve the velocity models, which is somewhat ambiguous. Therefore, not knowing the exact start time and location of the source signals reduce the achievable accuracy of the final velocity model. Furthermore there is no control over the location of the events, so that the spatial resolution is dependent on the distribution of the microseismic events - we can not perform tomographic inversion in areas where no rays from microseismic events pass through. Here the advantages of using ambient seismic noise to construct virtual source signals becomes apparent: we know the exact location (location of the sensors) and start time (zero lag time in correlation functions) of our virtual source signals so that the accuracy of the achievable velocity model is higher. We can also control the spatial resolution by installing sensors where greater resolution is required and we use all the available data.

In this study, we investigated the possibility of constructing seismic Green's functions between sensors by cross-correlating ambient noise recorded in an active underground mine. One month of continuous data recorded with the standard mine seismic moni-

toring network (<http://www.imseismology.org>) at Boliden's Garpenberg mine (Sweden) was examined.

In the first section of this article, we construct and use a 3D model of the mining excavations (tunnels, stopes, voids, caves, etc.) inside homogeneous host rock to generate numerical estimates of the seismic Green's functions between sensor pairs. We use these numerical Green's functions to approximate the scattering (caused by known mining excavations) of the seismic waves propagating between sensors to examine if these excavations create favorable conditions for reconstructing seismic Green's function by cross-correlating ambient noise.

In the following section we describe the different seismic noise sources that contribute to the recorded continuous data and examine the associated spectral properties. We found that the ambient seismic noise recorded in the underground mining environment is not ideal to construct seismic Green's functions between sensors by cross-correlating ambient noise with conventional methods - although sources of seismic energy were located in many different locations during the recording period, the noise is dominated by vibrations associated with mining activities which are often peaked in frequency and not distributed evenly around the seismic sensors. In other words, seismic noise sources in an active underground mine are not spectrally white and the seismic wavefield is not isotropic but directional.

In the final section we show that the large number of noise sources and the strong scattering caused by mining excavations create similar conditions where estimates of the Green's function can be retrieved, if cross-correlation functions are only considered when broadband noise sources are positioned, or scattered off excavations, in stationary phase locations. To identify time periods where these conditions are reasonably met, we develop and implement a selective stacking algorithm.

For the majority of the station pairs, we retrieve convincing Green's functions in the frequency band 20 - 400 Hz after the selective stacking algorithm is implemented. Two different frequency bands are used for different applications: we pick the arrival times of the body waves to perform an inversion for the 3D velocity structure of the underground mine for frequencies below 100 Hz and we use the multiply scattered waves in the reconstructed Green's functions to determine the scattering properties of the seismic waves caused by the mining excavations at frequencies above 200 Hz.

6.2 Numerical simulations

Seismic sources generated by industrial activity are not favorable for Green's function reconstruction as they are localized in space and peaked in frequency. However the seis-

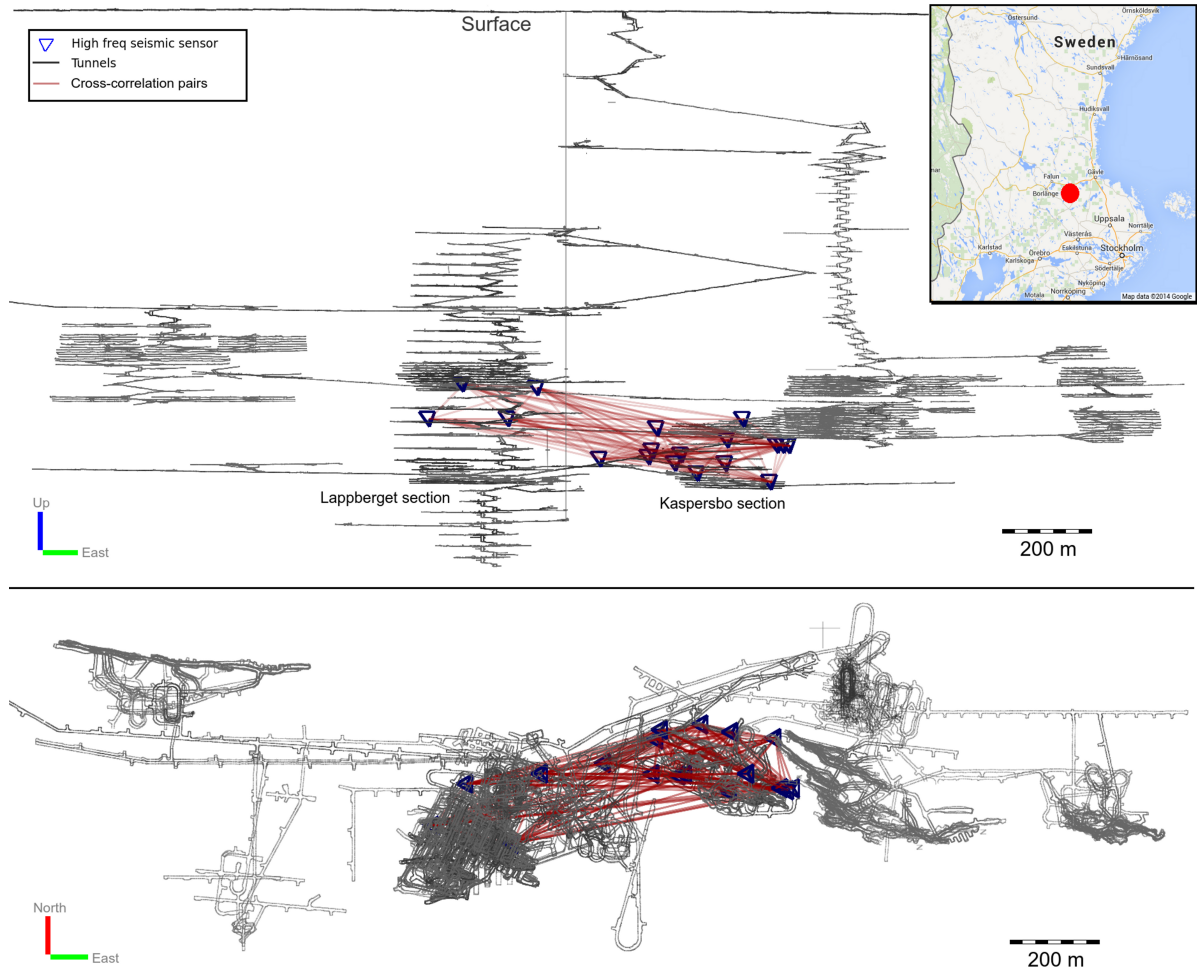


Figure 6.1 – Section view and plan view of Boliden’s Garpenberg mine in Sweden. The sensors are indicated by blue triangles, the ray paths of the cross-correlation pairs are shown in red and mining tunnels are gray. The red dot on the inset shows the regional location of the mine.

mic waves are scattered and each scatterer can act as a secondary source when enough seismic energy is present to excite it. The combination of these primary and secondary sources could yield more isotropic illumination, which is favorable for Green’s function reconstruction by cross-correlating seismic noise. It is thus important to understand the scattering caused by known excavations in the studied medium. In this section, we use numerical simulations of seismic waves propagating between sensors to evaluate the scattering caused by mining excavations in the studied underground mine.

In many underground mines the locations of the strong scatterers (mining excavations) are known to a good accuracy. Additionally, the average P- and S-wave velocities are known from calibration blasts. This gives an excellent opportunity to numerically calculate Green’s functions between sensor pairs.

To numerically model seismic Green's functions between sensor pairs, we construct a 3D structural model of the mining excavations inside the host rock and use a finite-difference kinematic seismic wavefield modeling code to generate synthetic seismograms between sensors. Since we use an impulsive, spectrally white source to generate the synthetic seismograms, these seismograms can be considered as numerical Green's functions. With these numerical Green's functions, we examine the scattering of the seismic waves caused by the mining excavations by calculating the average distance the seismic waves travel before they scatter (mean-free-path). Since the mining excavations are the only heterogeneities included in the otherwise homogeneous numerical model, we can compare the mean-free-path calculated from the numerical Green's function and the mean-free-path calculated from actual seismic data to reveal if the mining excavations are predominantly responsible for the scattering of the seismic waves in an underground mining environment.

6.2.1 Creating a realistic model

We constructed the numerical model from the known mining excavations that are present at Boliden's Garpenberg mine in Sweden (see Figure 1). In the numerical model we modeled all the points inside tunnels as air points with $v_s = 0$ m/s, $v_p = 300$ m/s, $\rho = 1$ g/m³ and near zero Q-factor ($Q = 0.01$). We constructed the rest of the model as the host rock with $v_p = 6650$ m/s, $v_s = 3850$ m/s, $\rho = 2700$ kg/m³ and frequency dependent Q-factor $Q(f) = \frac{10 \cdot Q_f}{f}$ with $Q_f = 1000$ Hz. The P- and S-wave velocities we chose are close to the values used by the mine to locate seismic events and have been determined by 5 calibration blasts that were performed on the 8th of August 2012 ($v_p = 6645 \pm 70$ m/s and $v_s = 3828 \pm 85$ m/s), whereas the density is representative of the average density of the host rock and Q-factor is chosen so that $Q(100$ Hz) = 100. To eliminate reflections from the boundaries of the model, we used absorbing boundary layers below and alongside the model, with a reflecting surface at the top which represents the surface of the earth.

The resulting model was roughly 4.2 km³ in size (3.5 km x 1.7 km x 0.7 km). With 2 m grid spacing, this amounts to about 500 million grid points. The grid spacing here is dependent on the frequency content we want to consider. Since signals of up to 400 Hz will be considered, the shortest wavelengths will be around 10 meters. The rule of thumb with numerical simulations is that each wavelength has to be sampled by at least 5 samples, so at most 2 m grid spacing is needed to adequately sample waves of all frequencies considered. Although the grid spacing is not small enough to sample the propagation of the acoustic waves through the air in the tunnels, we do not care about these acoustic waves but only the seismic waves scattered off the mining excavations.

Although the model contains realistic approximations of the mining excavations, it assumes that the excavations are surrounded by homogeneous host rock. Reality is somewhat more complicated: excavations have a fracture zone surrounding them and the host rock is inhomogeneous, especially close to surface where the host rock is layered. These inaccuracies make the multiply scattered coda part of the Green's function hard to model. The goal of generating the numerical Green's functions are therefore not to exactly retrieve the seismic Green's function, but rather to examine the scattering of the seismic waves by the known mining excavations so that we can determine if the excavations are the dominant cause of scattering of the seismic waves in the underground mining environment. If the mining excavations do cause significant scattering of the seismic waves propagating in the mining area, it could prove beneficial for reconstruction seismic Green's functions by cross-correlating seismic noise in sensor pairs since these excavations would themselves act as secondary sources (Derode et al., 2003).

6.2.2 Scattering caused by mining excavations

We want to investigate the influence of the mining excavations on the seismic waves propagating between sensors, to determine if the scattering caused by them are beneficial for constructing cross-correlation functions (CCFs) that resemble seismic Green's functions. To do this, we generated numerical Green's functions between all seismic sensors. In each simulation, we replaced one of the 18 sensors with an impulsive, spectrally white source in a downward (-Z) direction and recorded the vertical ground motion (Z) traces on the other sensors. We created the source by applying a bandpass-filter in the frequency range 20 to 400 Hz to an impulsive signal. We chose this frequency range in order to compare the results with the ambient noise cross-correlations later in this article.

In Figure 2 we show a comparison of the seismograms of a source-receiver pair 400 meters apart, where the tunnels and excavations were included and excluded in the numerical model. The inclusion of the tunnels dramatically changes the shape of the recorded seismograms in three ways: (a) the coda part of the waveform is extended due to the scattering caused by excavations (b) when the tunnels are included, a clear direct S-wave arrival is only visible in the low frequency part (below 100 Hz) of the seismogram and (c) the highest amplitude is observed after the direct wave arrivals.

When strong multiple scattering occurs, it has been shown that the amplitude of the coda waves can be larger than the direct arrivals (Nakamura, 1977). For multiply scattered waves, we can model seismograms with the diffusion model when the time is larger than the average time the seismic waves travel before scattering (mean-free-time) (Wegler and Luhr, 2001). By transforming seismograms to energy density and comparing them with different energy densities that are modeled by the diffusion model, we can isolate the energy loss due to scattering and intrinsic attenuation (see details in

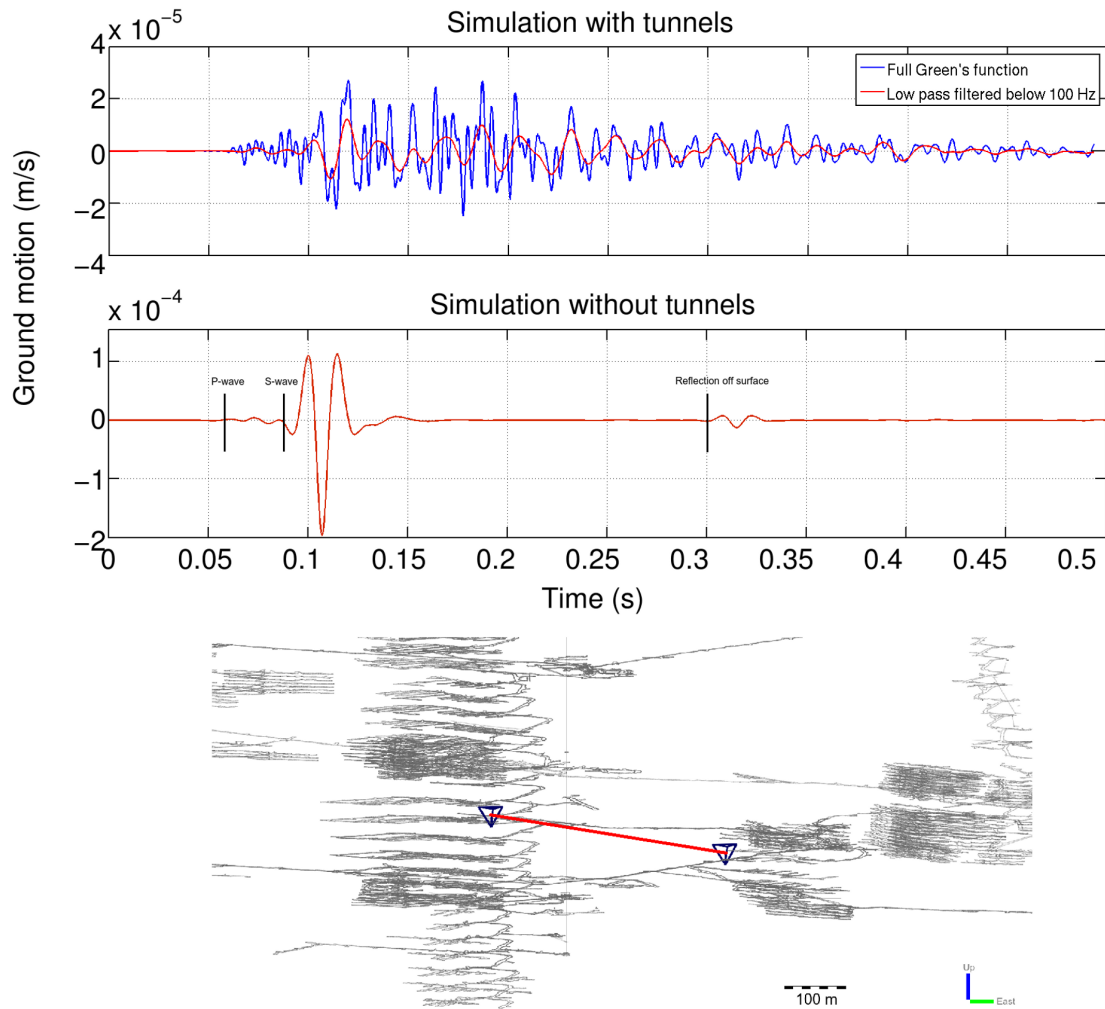


Figure 6.2 – The difference between synthetic seismograms with and without the tunnels and excavations included in the model but with the same source time function (impulsive downward). When tunnels and excavations are included in the model, the seismic waves scatter multiple times and a lot of energy is present in the coda part of the seismogram. For the synthetic seismogram recorded when the tunnels are not included, the only remarkable feature after the body-wave arrivals (weak P- and strong S-wave) is the reflection off the free surface at roughly 0.31 seconds. When the tunnels are included, the direct S-wave arrival is only visible for lower frequencies (below 100 Hz) and the reflection off the free surface is buried by the multiply scattered waves in the coda.

Appendix A). When we constructed the numerical model, we explicitly specified the intrinsic attenuation (Q-factor), therefore when modeling the numerical seismograms with the diffusion model, the only parameter to fit is the scattering attenuation coefficient (η_s). The mean-free-path is given by the inverse of the scattering attenuation coefficient (η_s^{-1}).

In Figure 3 we show the process of transforming a seismogram to the energy density and inverting for the mean-free-path with the diffusion model. The details of this inversion are given in Appendix A. The average value of the mean-free-path for the 153 station pairs was found to be 33 meters with a standard deviation of 9 meters. The minimum value was 16 meters and the maximum value 56 meters. In general, the mean-free-path was found to be slightly higher in the Lappberget section than in the Kaspersbo section (see Figure 1).

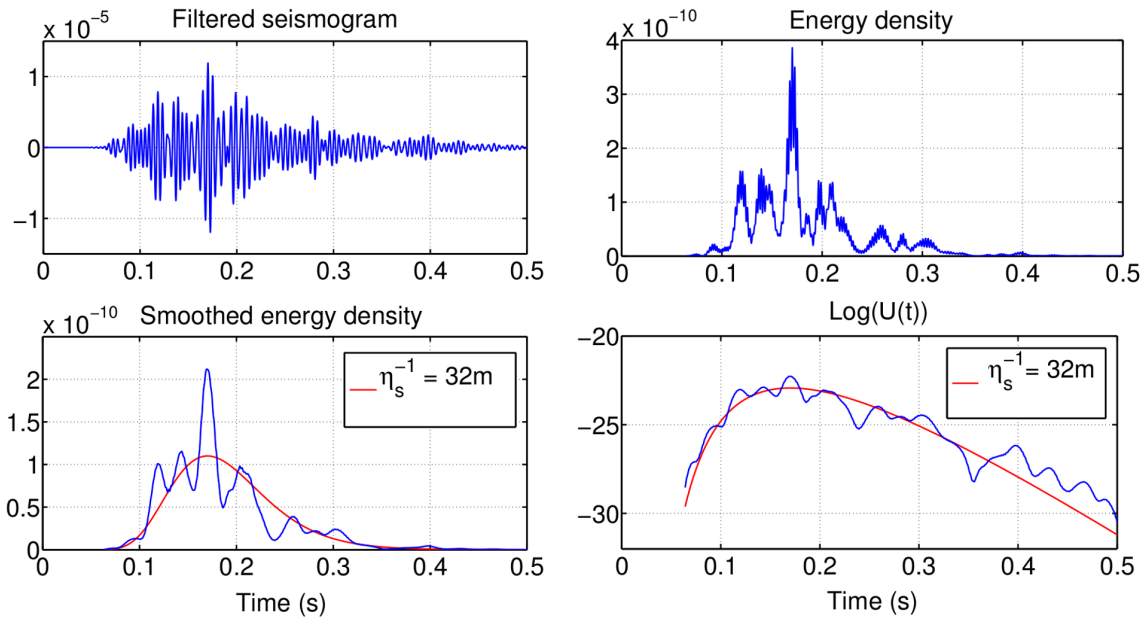


Figure 6.3 – The processing steps taken to invert for the mean-free-path with the synthetic seismograms. The top left figure shows the seismogram band-pass filtered in the range 170 - 220 Hz. The top right figure shows the seismogram after it has been transformed to energy density defined in Equation A.3. The bottom left figure shows the energy density after it was smoothed by a 100 millisecond box window with the control curve (inversion result) in red. The bottom right figure shows the logarithmic function from Equation A.2 along with the computed inversion result in red. The mean-free-path that fits the synthetic data the best was found to be 32 meters for this frequency range.

The diffusion model is a very simplified model that assumes strong scattering. The conditions necessary for strong scattering to occur and the diffusion model to be reasonable is that the wavelength of the seismic waves should be much smaller than the mean-free-path and the distance between the source and receiver. The mean-free-path we found in Figure 3 was 32 meters for the frequency range 170 - 220 Hz. This length is roughly the same as the wavelength of a S-wave of frequency of 120 Hz. Therefore, for the rest of the article we will only attempt to calculate the mean-free-path for frequencies above 200 Hz. For frequencies above 200 Hz, we also ensure that the distance between

the source and receiver is much larger than the wavelengths of the seismic waves for almost all station pairs.

6.2.3 Influence of source-receiver distance on scattering regime

The level of diffraction of the seismic signal is related to the ratio of the source-receiver distance to the mean-free-path. If the distance between the source and receiver is much larger than the average distance before the seismic wave scatters, multiply scattered waves arrive at the receiver shortly after the primary waves (Margerin et al., 2000). This scenario is referred to as the multiply scattered regime. However, if the distance between source and receiver is less than the average distance before the seismic wave scatters, this is not the case and the waves are in the single-scatter regime.

The signatures of the single scatter regime are clear direct arrivals and short coda waves indicating little scattering. For the numerical simulations we found that the waves are in the single-scatter regime for lower frequencies as clear direct arrivals are visible. For higher frequencies, the direct arrivals are not clearly visible and the coda part of the waveforms are extended - in this case the signals are in the multiply-scattered regime. Although the frequencies where the different scattering regimes occur are different for each source-receiver pair, we generally found that for frequencies below 100 Hz the waves are in the single-scatter regime and for frequencies above 200 Hz the waves are in the multiply-scattered regime (see Figures 5 and 11).

The fact that for frequencies below 100 Hz the waves propagating between sensors are in the single scatter regime does not mean that the low frequency seismic waves in the ambient noise are not scattered by the mining excavations before they are recorded by the seismic sensors. Rather the seismic sensors are too close to each other for the longer wavelengths going from one sensor to the other to be multiply scattered.

Throughout this article, we use the two scattering regimes for two different applications: for frequencies below 100 Hz (single-scatter regime) we identify the direct arrivals and use them with tomographic inversion to determine the local velocity structure, whereas for frequencies above 200 Hz (multiply-scattered regime) we fit the diffusion model to the waves and determine the mean-free-path of the medium.

6.3 Data

The seismic monitoring network consists of 7 tri-axial and 11 uni-axial short-period 14 Hz geophones. The geophones were permanently installed into boreholes 10 meters

above tunnel structures. Signals were sampled at 6000 samples per second and time synchronization is achieved over dedicated fiber-optic cables from the central GPS receiver to each of the underground stations. The inter-sensor distances range between 13 and 900 meters and the sensors are located roughly 1 km below surface. In Figure 1, we show the mine plans with the location of the seismic sensors relative to the mining excavations. At this depth, the sensors are not in the layered host rock close to the surface and far enough above the tunnels to be out of the zone of fractured rock surrounding them (estimated by the mine to be 5 meters). This is advantageous when looking at high frequency content which is normally attenuated very quickly close to the surface (Picozzi et al., 2009; Frankel et al., 1990).

In Figure 4 we show an example of 5 seconds of continuous seismogram data. The first part of the seismogram shows the repetitive signal resulting from impacts of a hammer drill that was roughly 120 meters away from the sensor. Drilling, which will typically occur in many places simultaneously, is very energetic and has broad spectral content which is beneficial for reconstructing a seismic Green's function if drilling occurs in stationary phase locations. The second part of the signal has no noteworthy attributes and consists of noise generated by multiple sources far away, like air vents and trucks. Although the strength of this section of noise is low compared to first section, the level is still an order of magnitude above the electronic self-noise level of the analogue/digital converter. The power spectral density of this part shows that mechanical sources are very peaked in frequency. The third part of the signal shows a microseismic event. This event has a local magnitude of -3 and was located roughly 30 meters away from the seismic sensor. The data slice shows the sources of seismic signal can change in a short period of time - the drilling in this example changes the amplitude of the background seismic signal multiple orders of magnitude in a matter of seconds. The power spectral density of each of the three parts show that during the second part of the signal, the noise is dominated by monochromatic sources.

6.3.1 Examining scattering properties with microseismic events

To examine how realistic the mean-free-paths obtained from the numerical simulations are, we considered microseismic events recorded and located by the seismic monitoring network during June, 2013. In Figure 5 we show one of these microseismic events in two different frequency bands. In the low frequency band (below 100 Hz) the direct P- and S-wave arrivals are visible (indicated on the figure), whereas in the high frequency band (above 200 Hz) the arrivals are not clear. We can confirm that these arrivals are P- and S-waves by (a) determining the travel time residual of the direct arrivals after the event is located by the seismic monitoring system and (b) by the ratio of the apparent P-wave velocity over the S-wave velocity of the direct arrivals - if the travel time residual is small and the $\frac{V_p}{V_s}$ ratio is close to $\sqrt{3}$ the arrivals are confirmed to be P- and S-waves.

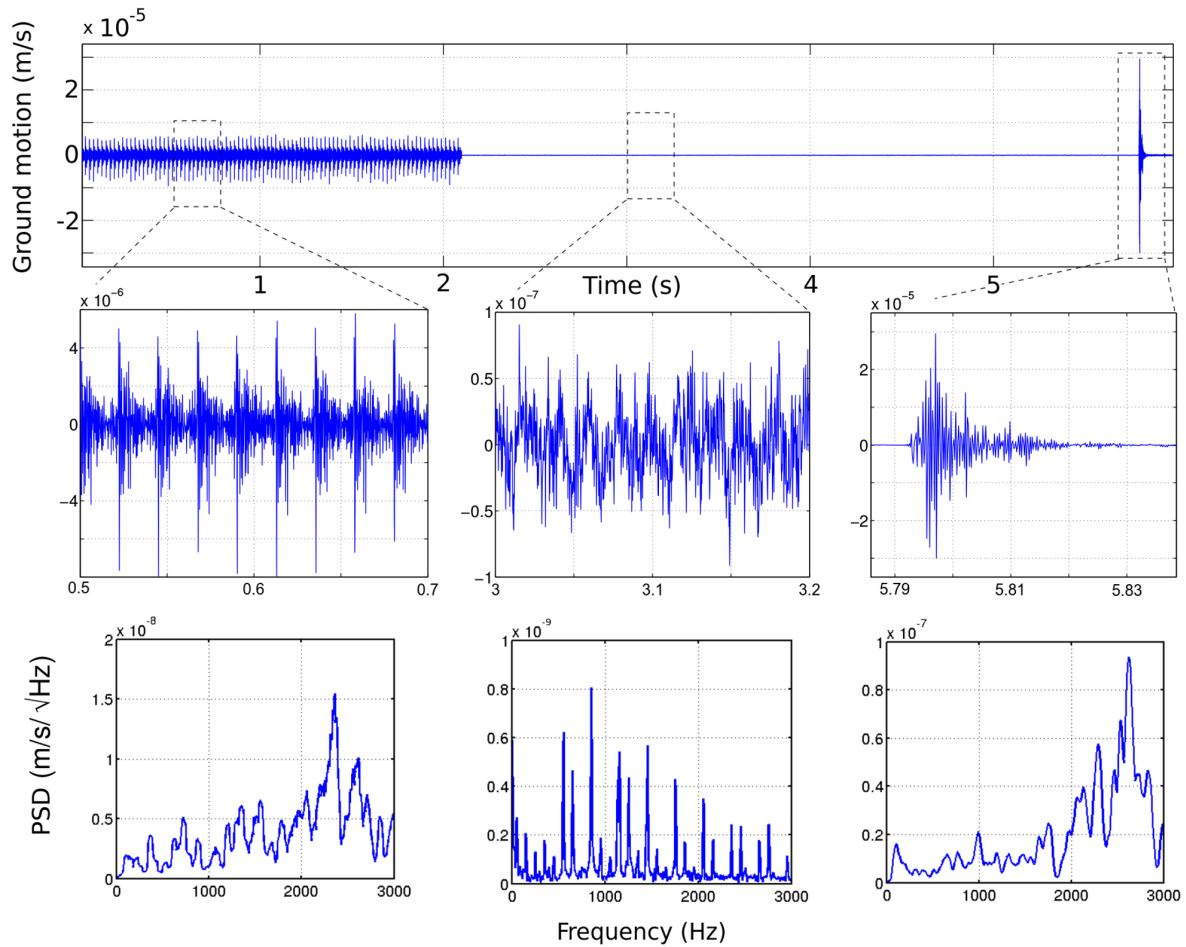


Figure 6.4 – A seismogram of length 5 seconds showing the changes in seismic noise. Three distinct time periods have been marked in the seismogram: In the first block the repetitive impacts of a hammer drill are visible. Drilling occurs in multiple places during a normal day of mining. The second block shows no distinct features. The noise here is due to a combination of far away sources like trucks, ventilation fans and ore crushing. In the third block a recorded microseismic event is shown. This event has a local magnitude of -3 and was located roughly 30 meters away from the seismic sensor. Thousands of these microseismic events happen in a given day. The bottom three windows show the power spectral density of each time period. For the middle time period with background noise, it is clear that the signal is very peaked in frequency whereas for the other two periods seismic energy is present in a broad frequency range from 10 - 3000 Hz.

In Figure 5 we show the inversion for the mean-free-path for frequencies above 200 Hz (see Appendix A for details). The value of the mean-free-path we found by the inversion is 43 meters. This value is close to the value found with the numerical simulations. Since we only included mining excavations inside the homogeneous host rock in the numerical model, and we obtain similar values for the mean-free-path with actual seismic data, it confirms that the mining excavations are the dominant cause of scattering in an under-

ground mining environment.

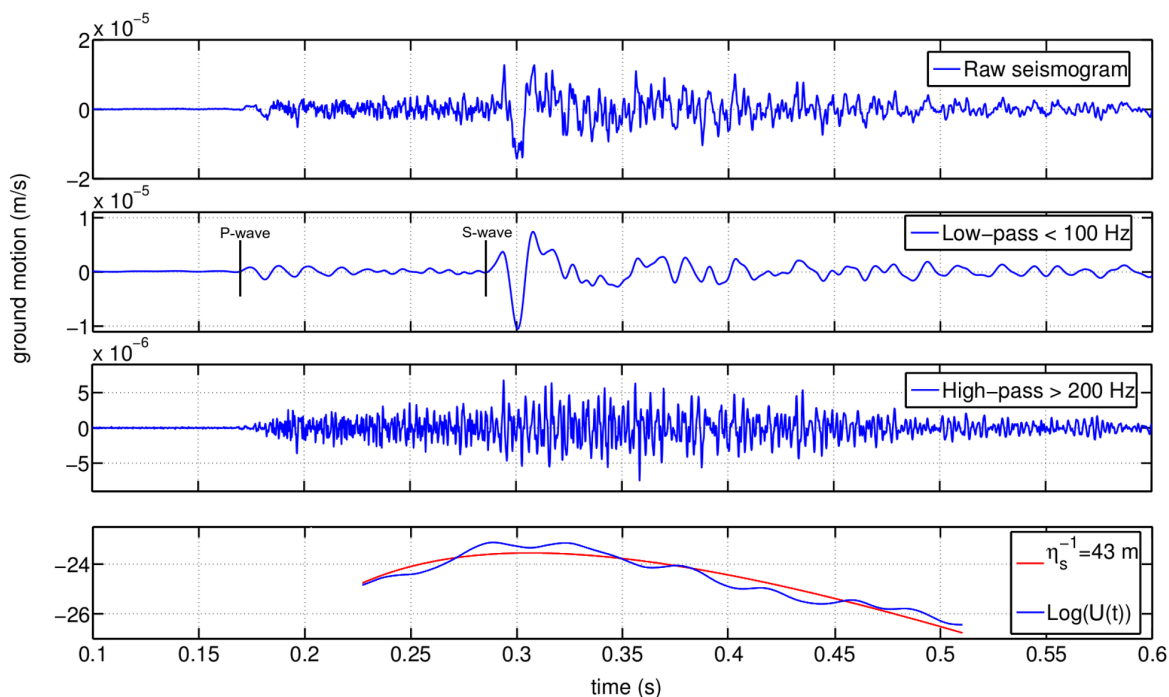


Figure 6.5 – A recorded microseismic event filtered in the low frequency band (below 100 Hz) and high frequency band (above 200 Hz). In the low frequency band the direct P- and S-wave arrivals are picked and in the high frequency band the mean-free-path is determined (see Appendix A). The mean-free-path found by the inversion here is 43 meters. The low value of the mean-free-path for the microseismic event is in agreement with the numerical simulations performed in Section 1.

By filtering the seismogram in different frequency bands, we show the possibility of using the same signal for different applications. The low frequency content of the seismic waves display direct body wave arrivals; we pick these arrivals and use it to establish a velocity model of the medium. The high frequency content does not show clear body wave arrivals since the wavefield is diffuse; we use this part to approximate the scattering properties (like the mean-free-path) of the medium.

From the dramatic change in the waveforms after the tunnels were inserted in the numerical model and the low mean-free-path obtained from the inversion of synthetic and real data at high frequency, it is clear that the tunnels and excavations cause the seismic waves to be highly scattered before they are recorded by the seismic sensors. This scattering ensures that high frequency signals are in the multiple scattering regime even when the source-receiver distance is as low as 100 meters which will prove to be beneficial when we are constructing cross-correlation functions. If we can construct good estimates of the Green's functions by cross-correlating ambient seismic noise, we can

examine the material properties of the surrounding medium with greater accuracy than by using microseismic events.

6.4 Ambient noise cross-correlations

In general, it is assumed that the longer the duration of the seismic signal used to construct cross-correlation functions, the better the convergence of the correlation function to the Green's function will be due to the reduction of random fluctuations and enhanced contribution of weak sources (Larose et al., 2008). In this section we explore an optimized way of retrieving Green's functions in the conditions of non-stationary industrial sources of seismic noise.

6.4.1 Stationary phase locations

The seismic Green's functions can be reconstructed by cross-correlating spectrally white seismic noise coming from all exterior directions recorded in two sensors (Lobkis and Weaver, 2001) or by cross-correlating spectrally white noise only coming from stationary phase locations (Roux and Kuperman, 2004). In an active underground mine, the seismic noise is dominated by local mining activities so that the resulting seismic wavefields are directional. When cross-correlating directional seismic wavefields, only station pairs that are favorably aligned so that the noise is propagating in the stationary phase directions will succeed in recovering the seismic Green's functions.

Because of the noisy nature of an underground mine it is reasonable to assume after an adequate amount of time that there are noise sources located at almost every location in the mining excavations (all excavations should at least experience traffic from underground vehicles at some point in a one month period). Additionally, the mining excavations could scatter incoming seismic waves and therefore themselves act as secondary seismic sources when enough seismic energy is present to excite them (Derode et al., 2003). Although the seismic wavefields are directional and the mining excavations are not spatially distributed all around the seismic sensors, when we consider Figure 1 it seems likely that many of the sensor pairs could at some point have seismic energy propagating from (or scattered off) their corresponding stationary phase locations.

6.4.2 Monochromatic sources

In general mechanical sources (pumps, fans, etc.) are expected to be peaked in frequency. When monochromatic sources dominate the noise records, the cross-correlation

function will have regularly spaced peaks where the lag-time between peaks correspond to the monochromatic phase. When we blindly use all data the recorded for this study to construct correlation functions, the correlation functions have peaks at regular intervals, which shows that it is dominated by monochromatic sources or sources that are peaked in frequency (see the middle section of Figure 4).

We determined that these regularly spaced peaks in the correlation functions are due to ventilation fans in the tunnels, which are very strong, stable sources that are peaked in frequency. These fans are so stable that whitening the signals before cross-correlating is not sufficient to suppress them - if we stack enough of the individual cross-correlation functions, the regularly spaced peaks reappear due to their stability and strength. This phenomenon can be seen in Figure 6, where we show that selectively stacking a subset of one month of data yields a more convincing estimate of the Green's function than stacking all the data. We discuss the selective scheme used to determine the subset of data in the following section.

The abundant sources, together with the strong scattering properties established earlier, indicate that theoretical conditions exist for creating good estimates of the seismic Green's functions by cross-correlating ambient noise for station pairs that are favorably orientated. The challenge is to only use the sources in stationary phase locations to create the correlation functions and to dismiss the data from strong, stable monochromatic sources or sources in non-stationary phase locations.

6.4.3 Selective stacking

To dismiss data from monochromatic sources and sources in non-stationary phase locations, we developed a selective stacking scheme. This scheme identifies time periods when noise sources are located in stationary phase locations (and are not monochromatic) and only uses correlation functions during these times to add to the stacks for individual station pairs.

To identify the periods when the noise is coming from stationary phase locations, we calculate the root-mean-square (RMS) of the signal in the lag-time window of the correlation function around the expected arrival times of the S-waves and divide it by the RMS of the signal in the far coda part of the signal to get an effective signal-to-noise ratio (SNR). The lag-time window we consider for calculating the SNR is the distance between sensors divided by the S-wave velocity $\pm 30\%$ ($[\frac{d}{0.7*V_s}, \frac{d}{1.3*V_s}]$). This lag-time window is wide enough to ensure that sufficient individual time periods pass the stacking criteria so that the stacked correlation functions converge to stable waveforms.

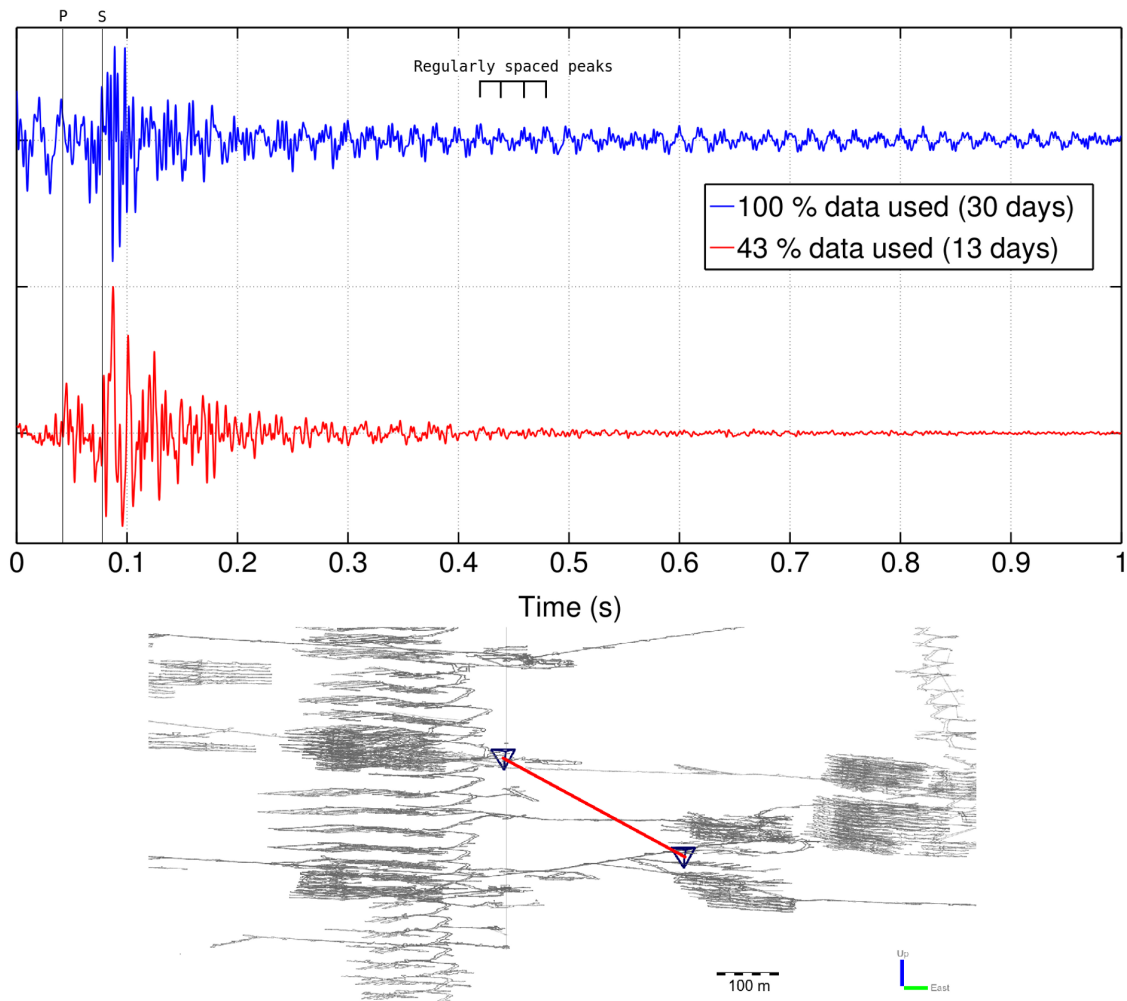


Figure 6.6 – Comparison of the cross-correlation function for one station pair when a subset of 43% of the data is stacked (bottom) compared to the cross-correlation function when all of the data is stacked (top). The cross-correlation function shows direct P and S-wave arrivals when 43% of the data is used. The expected P- and S-wave arrivals are indicated by black lines. The direct arrivals are not clearly visible when all the data is used. Instead we see regularly spaced peaks because of the influence of monochromatic sources.

If we only stack the cross-correlation functions when the SNR is high in the expected arrival time window, it increases the chances of selecting time periods where the noise sources are located in or scattered off the stationary phase locations. For sources in non-stationary phase locations (that do not scatter off mining excavations in stationary phase locations) the correlation functions will have a peak at earlier lag-times and no peaks in the expected arrival time window. Selective stacking also dismisses time periods where the noise is dominated by monochromatic sources or sources in non-stationary phase locations - in the presence of monochromatic sources the correlation functions have a

low SNR because of the regularly spaced peaks.

We spectrally whitened short continuous data slices (10 seconds) between 20 and 400 Hz for each seismic sensor and cross-correlated them to construct individual cross-correlation functions. Although a lot of seismic energy is present at higher frequencies (see Figure 4), we found that the frequency window maximizes the SNR of the final cross-correlation functions. Also - as shown in the previous section - the higher frequency content is not useful for tomography since the waves are in the multiply scattered regime. As the nature of the noise can change rapidly in a matter of seconds (see Figure 4) it is important that we only consider 10 second intervals at a time, since longer period could contain a mix of short seismic signals in stationary phase locations and monochromatic sources or sources that are not located in stationary phase locations. We did not perform time domain normalization (one-bit normalization) in order to try to preserve the dominant influence of energetic seismic signals (like microseismic events, drilling, blasting, etc.) in stationary phase locations. If the SNR of an individual cross-correlation function for a station pair is higher than 4, the individual cross-correlation function is weighted by the square of the SNR and added to the total stack for the station pair. By weighting the cross-correlation functions, we favor the time periods when energetic seismic sources are in stationary phase locations in the stack. For some station pairs we found that the weighting of the correlation functions are enough to suppress the monochromatic signal, but for most of the station pairs (with one or more sensors close to a ventilation fan) that this is not the case and the selection criterion is necessary.

In Figure 7, we show 10 second intervals of continuous data recorded by the same sensor at different times. In the top figure the noise is usable for many station pairs since multiple sources are present and seismic energy is contained in a broad frequency band. During this time 61% of the correlation pairs pass the selective stacking criterion. For the time period shown in the bottom figure, the magnitude of the seismic noise is significantly less and the noise is dominated by monochromatic signals from the ventilation fans. During this time period only 13% of the correlation functions pass the stacking criterion due to the monochromatic nature of the seismic noise recorded in most of the sensors.

In Figure 8 we compare the results of conventional blind vertical stacking and selective stacking for all 153 ZZ-components of the correlation functions between sensor pairs. For the top figure where we used blind vertical stacking, no clear wave arrival fronts can be seen. For the middle figure where we used the selective stacking, an arrival front is visible at positive and negative lag-times. The velocity of the arrival front is close to the current S-wave velocity used with the monitoring network to locate microseismic events (3828 m/s), even though the selection window is wide. For the 3-component sensors that were available, we examined the polarity of these waves to confirm that they are in fact S-waves. The SNR of the S-wave arrivals are significantly increased by using the amplitude selective stacking scheme. In the bottom figure we show the ZZ-component of the

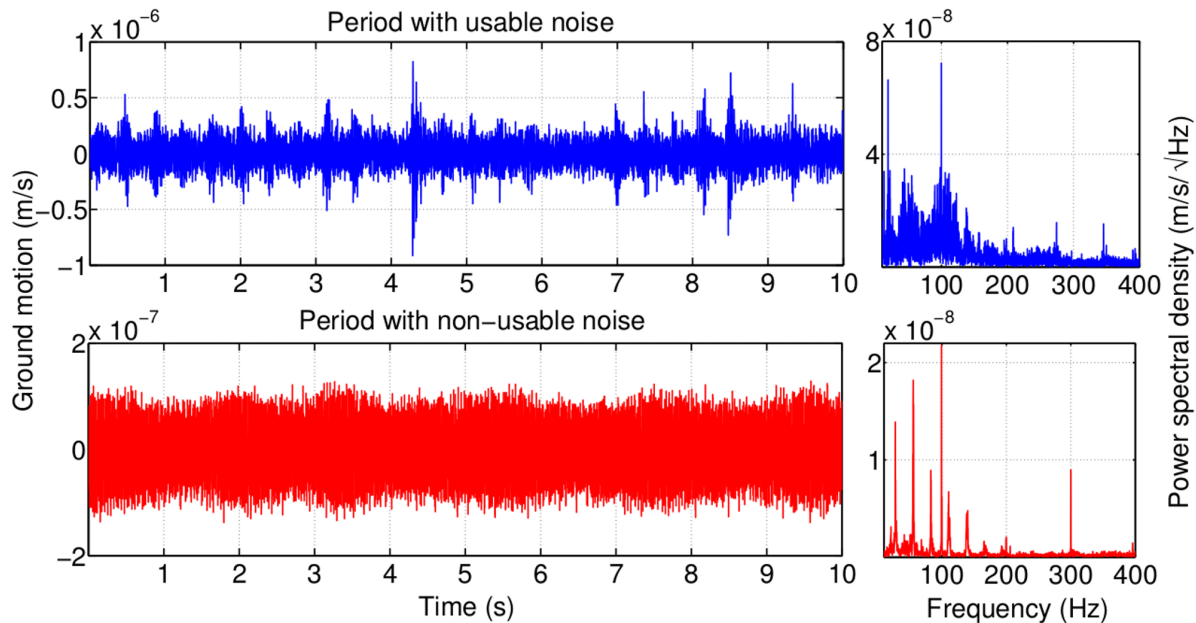


Figure 6.7 – Two 10 second periods of continuous data recorded by the same sensor at different times. At the time of the top figure, 61% of the correlation pairs passed the selective stacking criteria. This is thanks to the multiple sources and broadband content of the data. At the bottom figure only 13 % of the correlation pairs passed the selective stacking criteria. During this time the noise is dominated by ventilation fans that are very peaked in frequency.

numerical Green’s functions generated in Section 1. The ZZ-components of the numerical Green’s functions show a weak P-wave arrival front and a strong S-wave arrival front (indicated by black lines).

The ZZ-components of the cross-correlation functions do not show a clear P-wave arrival front. For some cross-correlation functions, an apparent P-wave arrival is visible (see Figures 6,10 and 11), but most cross-correlation functions do not. This is contrary to the idea that anthropogenic noise (drilling, hammers, etc.) consists mostly of P-wave energy, but we argue that there are 3 main reasons why the S-wave arrival front is more clearly visible than a P-wave arrival front: (1) The ZZ-component cross-correlation functions represent the signal recorded on the Z-component of one sensor if the other sensors was an impulsive source in the Z-direction. Since the sensors are roughly on the same horizontal plane, we therefore expect the S-waves to be the strongest. The ZZ-components of the numerical Green’s tensor in Figure 8 show a weak P-wave arrival front and a stronger S-wave arrival front which confirms this observation (2) The selective stacking scheme selects periods when the SNR of the correlation functions in the lag-time window corresponding to the expected S-wave arrival time are high - therefore with the stacking scheme we explicitly select times when the noise consists of S-waves. We purposefully chose the lag-time window around the expected S-wave arrival time window, since it is

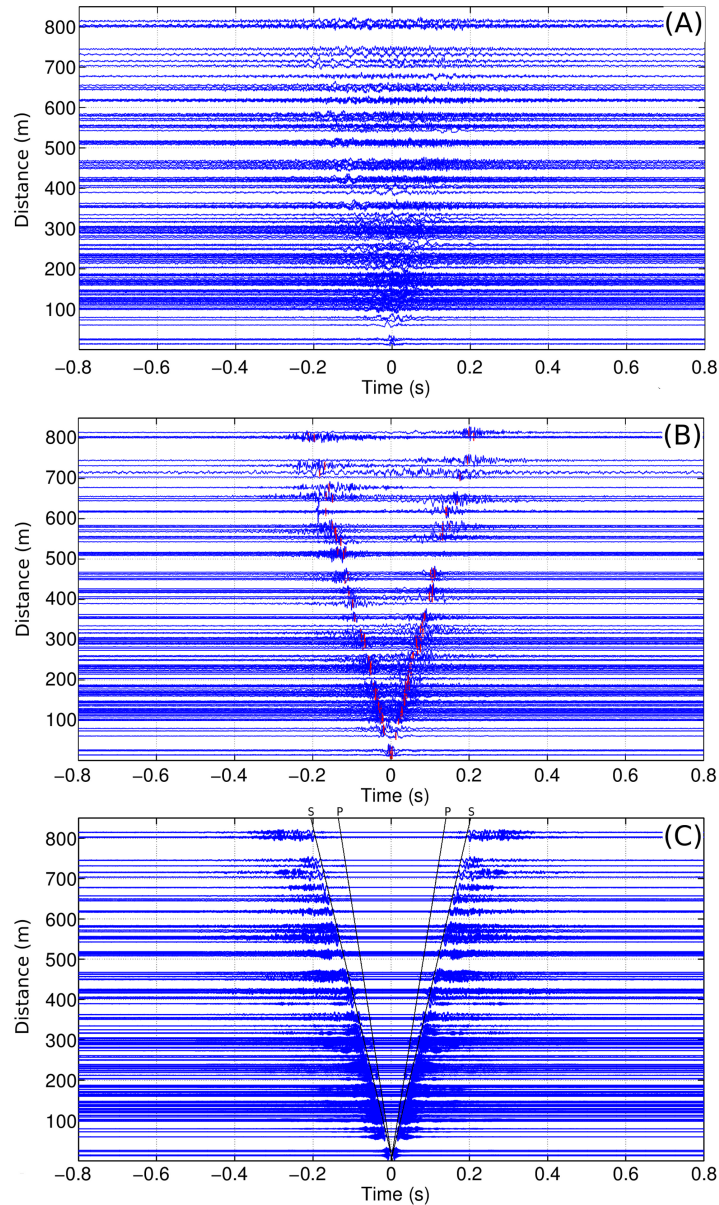


Figure 6.8 – The cross-correlation functions arranged by the inter-sensor distance. Figure (A) shows the CCFs when conventional blind vertical stacking are applied. No clear arrival fronts are visible. Figure (B) shows the CCFs when the selective stacking scheme is applied. A S-wave arrival front is visible. The picks that were obtained by the kurtosis-based algorithm are shown in red. Figure (C) shows the synthetic Green's functions generated with numerical simulations. The synthetic Green's functions show a weak P-wave arrival and a strong S-wave arrival. The expected arrival times in the synthetic Green's functions are shown with black lines.

hard to determine if the seismic energy in the lag-time window corresponding to the expected P-wave arrival time consists of P-waves in stationary phase locations or of S-

waves in non-stationary phase locations (3) It is known that multiply scattered waves consists mostly of S-waves, since P-waves are converted to S-waves more frequently than vice versa (Aki, 1992) so that continuous data is expected to consist mostly of multiply scattered S-waves, regardless of the source.

6.4.4 Directional bias from non-isotropic wavefields

Since sources of seismic signal (and mining excavations that act as secondary sources) are not uniformly distributed around our monitoring network, a directional bias is possible in the cross-correlation functions that could influence the tomography results (Tsai, 2009; Weaver et al., 2009). The potential error in the apparent velocity is inversely proportionate to the inter-station distance, so that sensor pairs close to each other are more likely to be affected. Furthermore, since we choose the time window for the selective stacking scheme to be wide ($V_s \pm 30\%$), if there are constant strong noise sources that dominate the stack of cross-correlation functions the error in apparent velocity can be up to 30%. To reduce the potential errors in the final tomography result, we could either narrow the window of the selective stacking scheme and/or we could only consider pairs far apart. If we narrow the window, we greatly reduce the amount of data used and artificially constrain the velocity to the expected value. Also since most of the sensors are less than 200 m apart, the achievable resolution of the model decreases significantly if we only consider sensors further apart. Instead, we only considered sensors further than 100 m apart and only accepted S-wave picks that are within 10% of the expected S-wave velocity (see Appendix B). This results in 121 of the 153 cross-correlation pairs to be usable in the tomography.

Apart from phase shifts, the causal (positive lag-time) and acausal (negative lag-time) could have different amplitudes depending on how frequently sources are located in each corresponding stationary phase location. This is confirmed in Figure 9, where we show a sensor pair where many mining excavations are located in the stationary phase location of signals going from sensor A to B, but not many excavations for signals going from B to A. Accordingly, the cross-correlation function has a strong apparent S-wave arrival in the causal part (signal from A to B) and a comparatively weak S-wave in the acausal part (signal from B to A) present in the cross-correlation function.

6.4.5 Convergence of cross-correlation functions to the seismic Green's functions

In Figure 10 we show the convergence of a cross-correlation function to a stable function after a sufficient amount of data has been processed. In this case after roughly 12 hours of raw time (8 hours effective time), a strong S-wave arrival is visible. When we

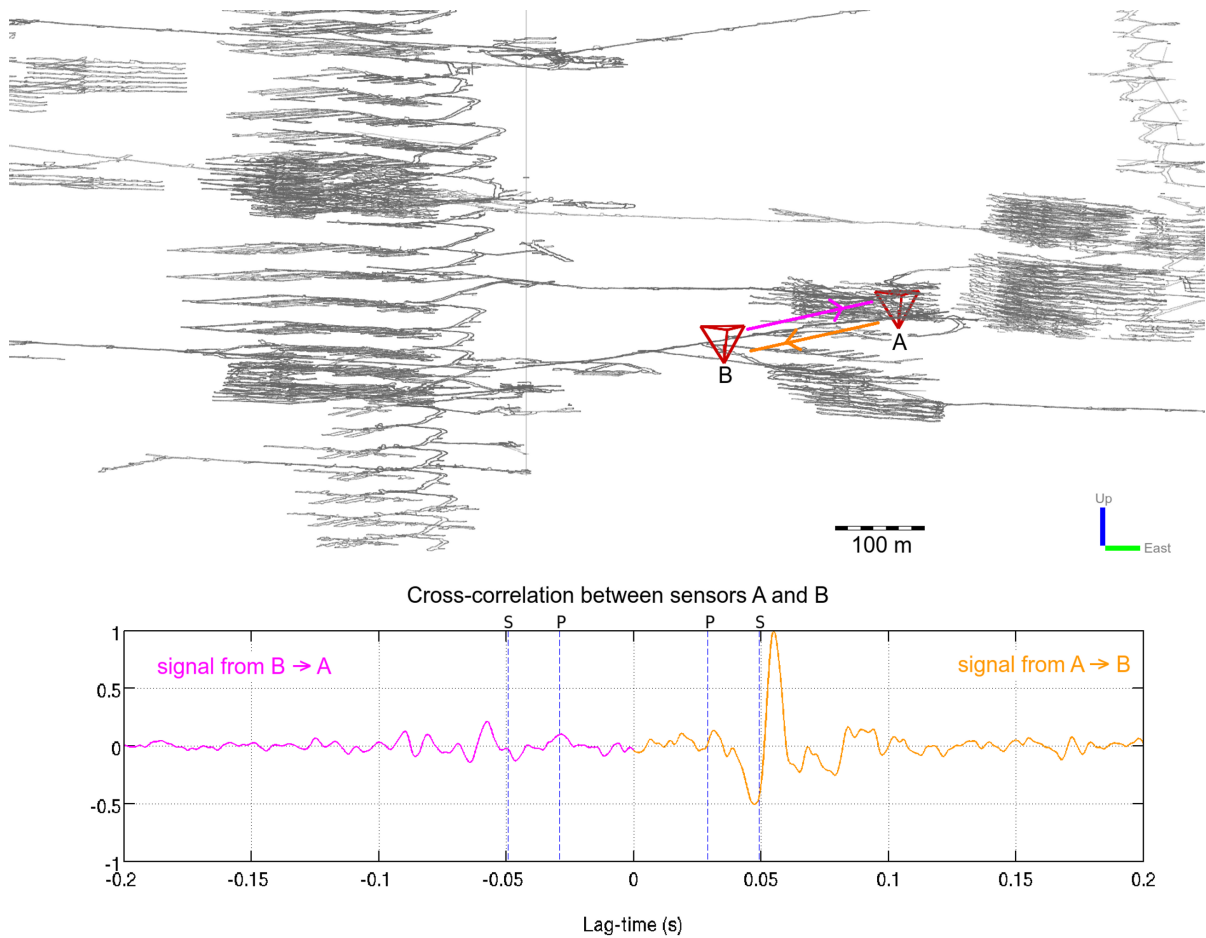


Figure 6.9 – The location of two sensors and the cross-correlation of the seismic noise recorded in them when the selective stacking scheme is used. The causal part (orange) of the cross-correlation function has a strong apparent S-wave arrival whereas the acausal part (purple) has a comparatively weak S-wave arrival. The directional bias of the cross-correlation function can be described by the scatterers in the stationary phase locations: behind sensor A there are many mining excavations that ensures that seismic waves propagate from the stationary phase location from A to B regularly, while behind sensor B there are not as many mining excavations so that seismic waves do not propagate from the stationary phase location from B to A as frequently.

correlate and stack more data, the amplitude of non-physical arrivals (around zero lag time) is decreased and finally after processing one month of raw continuous data (20 days effective time) a weak P-wave arrival is visible. In general, we found that the rate of convergence of the cross-correlation function to the Green's function is dependent on the inter-sensor distance, with the pairs closer together converging faster than the pairs further apart, as expected. Additionally, the larger the inter-sensor distance, the more energetic sources are needed to satisfy the selective stacking criteria. This means that the percentage of data used to construct the cross-correlation functions is inversely pro-

portional to the inter-sensor distance.

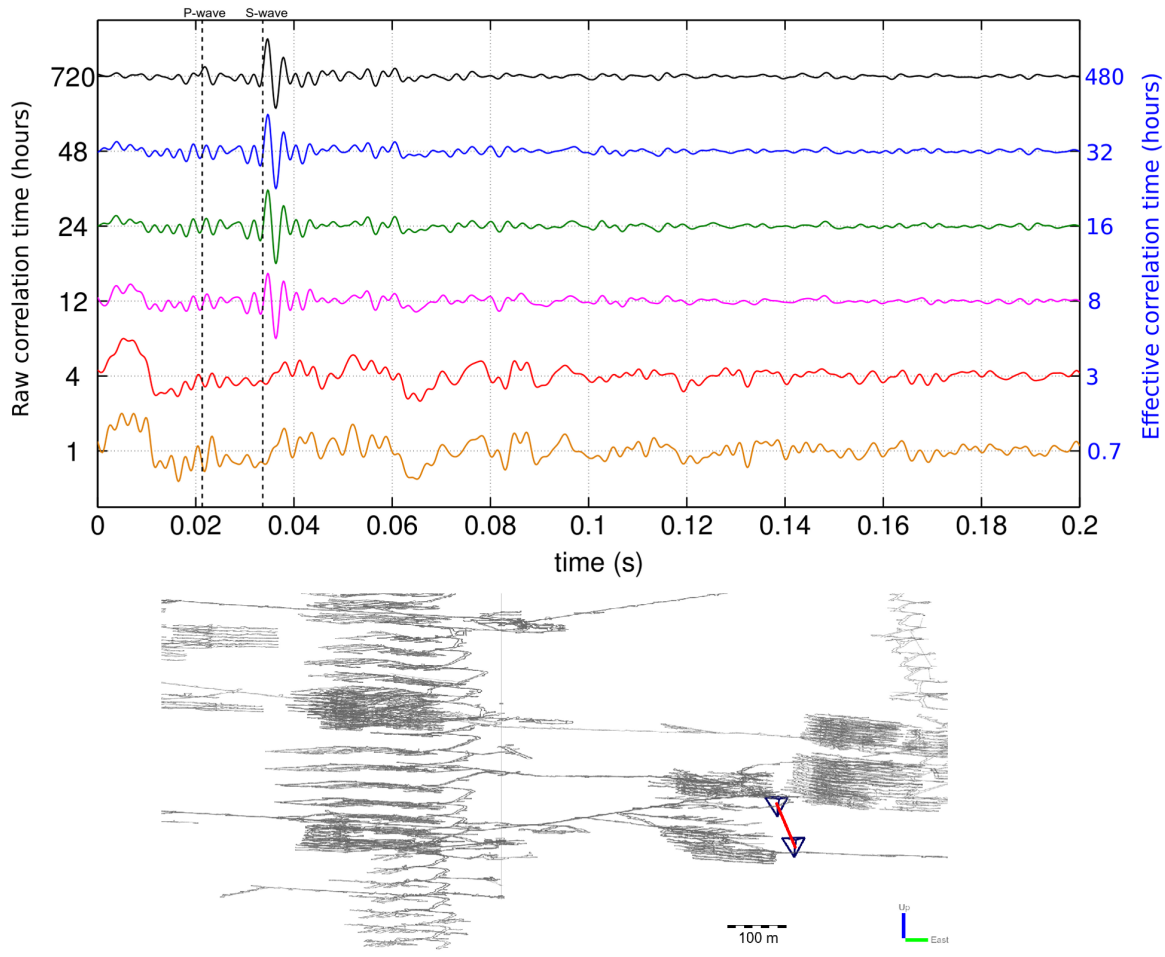


Figure 6.10 – The convergence of the cross-correlation function to the Green’s function. The S-wave arrival is stable after 12 hours (8 hours effective time). After 30 days (20 days effective time), the non-physical arrivals are weaker and a faint P-wave arrival can be seen. The effective time refers to cumulative time that passed the selective stacking criteria and therefore the actual amount of data used to construct the correlation functions.

6.4.6 Frequency content of the cross-correlation functions.

Since we found that seismic Green’s functions can be constructed for a broad frequency range (20 - 400 Hz), we can use different frequency bands for different applications (as discussed in the previous section). In Figure 11 we show a cross-correlation function split in two frequency bands. Below 100 Hz direct P- and S-waves arrivals can

be seen (indicated on the figure), whereas above 200 Hz this is not the case. This is because above 200 Hz the wavefield is diffuse due to the scattering caused by the mining excavations. The bottom figure shows the result of the inversion we obtained for the mean-free-path when the cross-correlation function is high-pass filtered above 200 Hz. The average value of the mean-free-path calculated for all of the 153 cross-correlation functions was found to be 39 meters with a standard deviation of 17 meters; this observation is consistent with the results from the numerical simulations and microseismic data. In the following section we use the lower frequency content of the cross-correlation functions to invert for the local velocity structures by picking the arrival times of the direct S-waves.

6.4.7 3D S-wave velocity model

Most underground mines use an isotropic homogeneous seismic velocity model in routine microseismic monitoring. The average velocities are determined by calibration blasts or minimizing the travel time residual for a large number of events recorded by multiple sensors (Mendecki, 1997). This simple velocity model is predominantly used because of the relatively small errors in seismic event locations and also because of the difficulty of conducting the many calibration blasts required to calibrate a full 3D velocity model. An accurate three dimensional inhomogeneous velocity would improve the location accuracy of seismic events and could also indicate geological features near the mine.

The details of the automatic picking of the S-wave arrivals and the inversion process are given in Appendix B. We show the successful picks of the cross-correlation functions with inter-sensor distance larger than 100 meters in Figure 12. The travel time misfit of the S-wave picks for the homogeneous model with least squares solution of $V_s = 3862\text{m/s}$ is 3.2 *ms*. The travel time misfit for the final result of the inversion is 2.5 *ms*. This corresponds to a misfit reduction of 22%.

We show the final result of the velocity inversion in Figure 13. The 3D S-wave velocity model shows a high S-wave velocity zone in the Kaspersbo section (on the right) and a low S-wave velocity structure in the Lappberget section (on the left). These two sections consist of two known ore bodies. The locations of these ore bodies are shown by wire frames determined by drill samples in the bottom of Figure 13. The location of the ore body in the Kaspersbo section is in agreement with the high velocity zone from the inversion, but the low velocity zone is mispositioned with regard to the Lappberget ore body. This is because most of the Lappberget ore body is outside the grid where we invert for the velocity. According to geologists at Garpenberg, the ore body in Kaspersbo has significantly different material properties to the ore body in Lappberget - most notably there are many silica and skarn intrusions in Kaspersbo. The silica and skarn intrusions simultaneously decrease the average density and increase the shear modulus of the bulk medium as observed in laboratory measurements on core samples (Boliden, 2014). Both

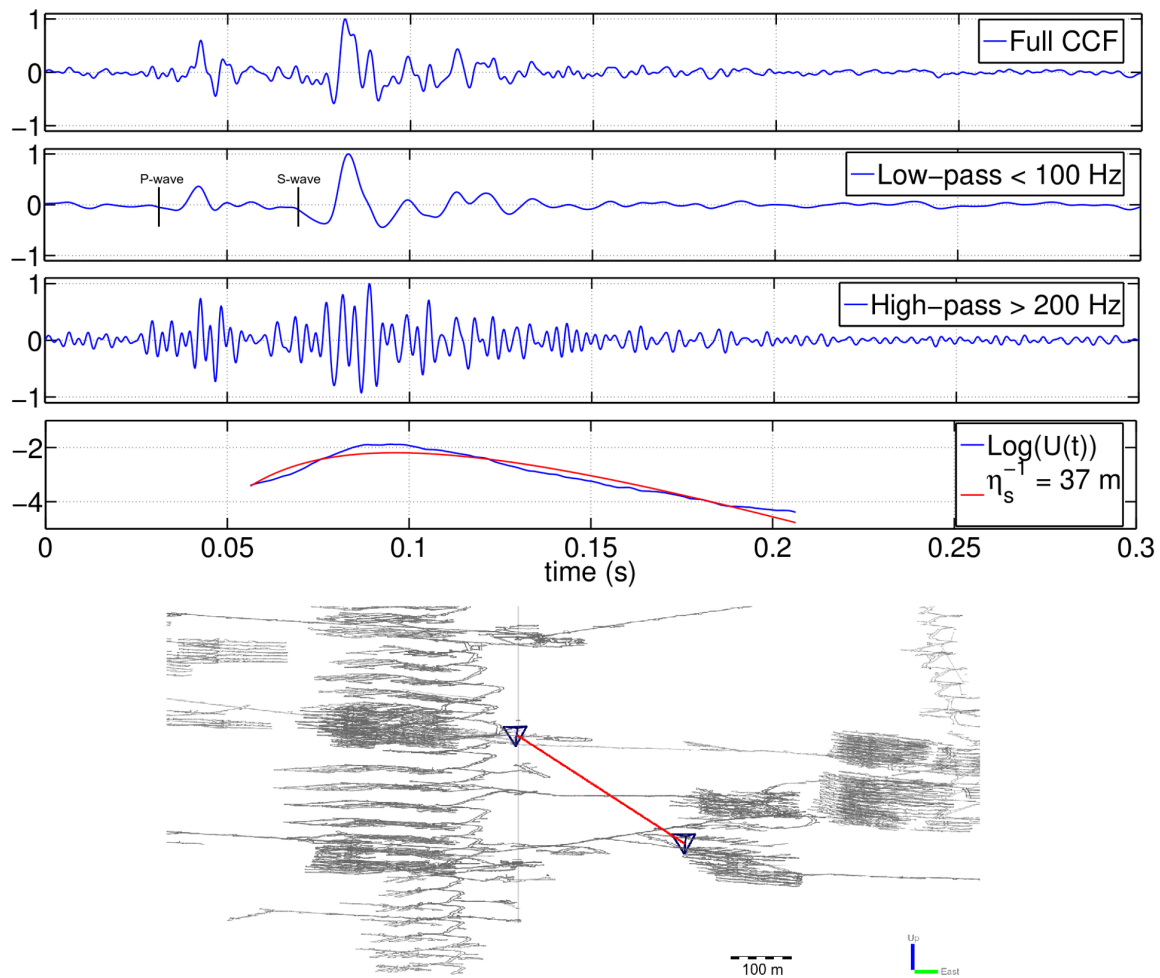


Figure 6.11 – The different frequency components of the cross-correlation function. Direct P- and S-wave arrivals are visible for the low frequency part of the CCF, whereas the high frequency part is diffuse due to the scattering by the tunnels and excavations. As a result there is no clear direct P- and S-wave arrivals. The inversion of the mean-free-path is shown in the bottom window and was determined to be 37 m.

a decrease in density and increase in shear modulus are expected to increase the S-wave velocity of the medium (Aki and Richards, 1980).

An alternative explanation for the higher and lower S-wave velocity found in the Kaspersbo and Lappberget sections could be the uneven distribution of noise sources, since it has been shown that an non-isotropically distributed noise sources can lead to errors in the apparent arrival times in cross-correlation functions as discussed earlier. The error in travel times for direct arrivals induced by non-isotropically distributed wave intensities have been studied with theoretical methods (Froment et al., 2010) and with field data (Yao and van der Hilst, 2009) and in both cases found to be negligible (less

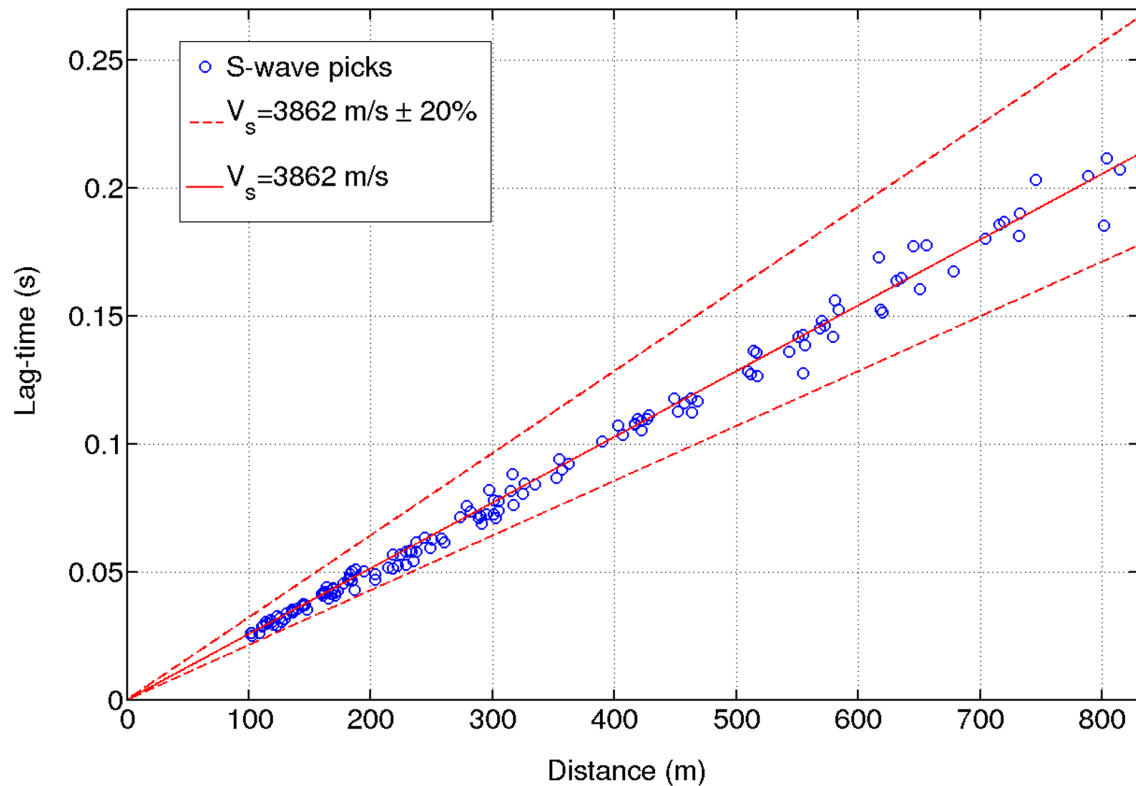


Figure 6.12 – The S-wave picks (blue) from the automatic Kurtosis based algorithm along with the homogeneous least squares solution (solid red) as a function of distance for cross-correlation functions with successful S-wave picks. The maximum allowed picking variations are indicated by the dashed red lines. The picking constraints ensure that other local maxima (scattered P- or S-waves) are not mistakenly picked as S-wave arrivals.

than 1 %) for tomographic studies. Therefore we consider that the different material properties are the true explanation for the apparent high and low velocity structures in the final S-wave velocity model.

6.5 Conclusions

In this article we investigated the possibility of using seismic sensors installed at depth along with seismic noise generated by mining activities to estimate the seismic Green's functions between sensors. The results of numerical simulations indicate that seismic waves are highly scattered by mining excavations, indicated by the average distance the waves travel before they are scattered (mean-free-path) that we found was roughly 35 meters by modeling the numerical seismograms with the diffusion model in

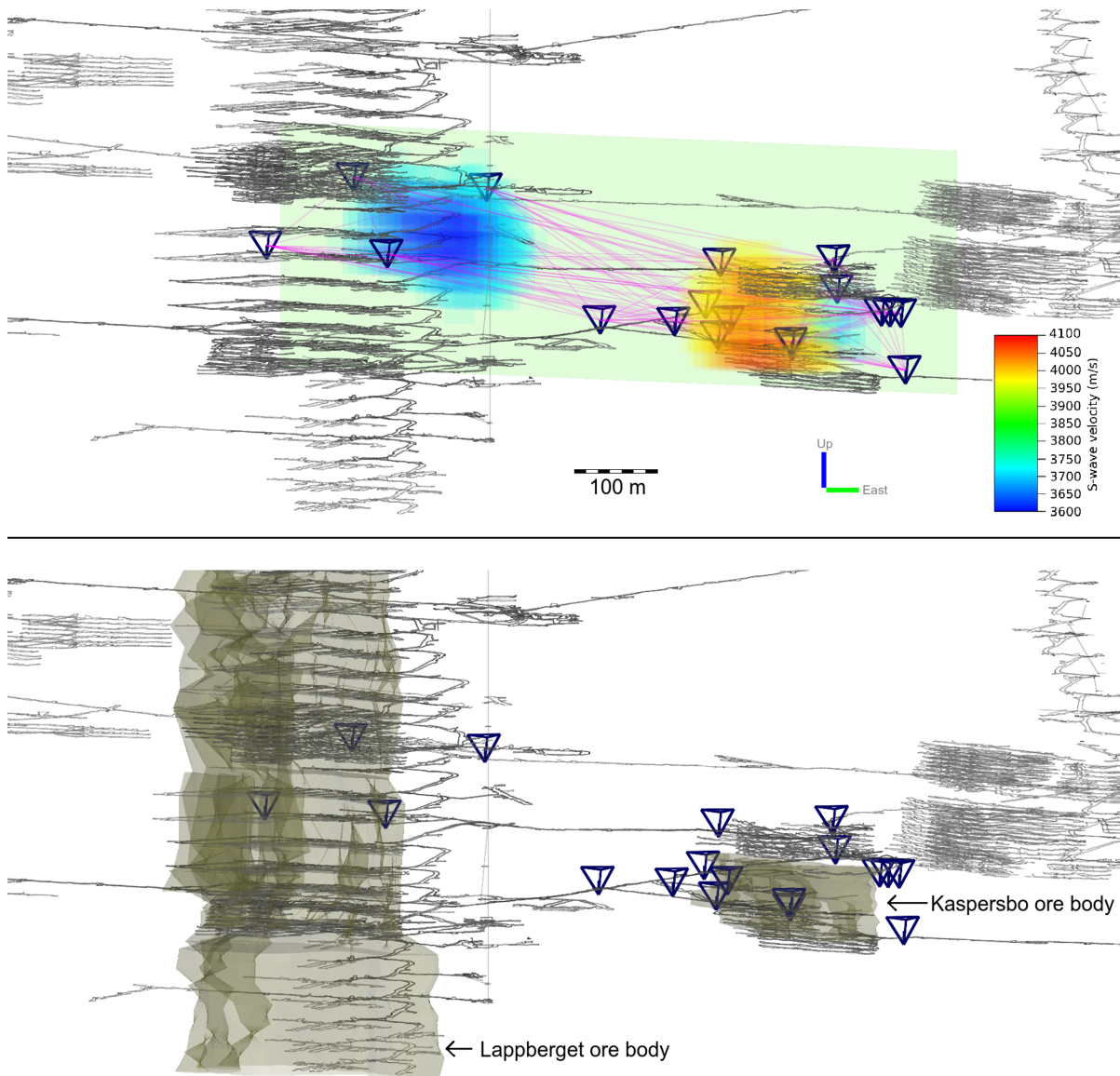


Figure 6.13 – 2D cross section of the result of the 3-dimensional S-wave velocity inversion. The velocity is slightly higher in the tunnel network in the Kaspersbo section on the right and slightly lower in the tunnel network in the Lappberget section on the left. The outlines of known ore bodies are shown in the bottom figure. The locations of these ore bodies are determined by drill samples. The high velocity structure overlaps with the Kaspersbo ore body.

the frequency band [170-220] Hz.

By inspecting the continuous data we found that a large number of noise sources with broad frequency content are present in an active mine. Not all seismic waves generated by mining activities are useful to construct seismic Green's functions between sensors; more specifically stable, monochromatic vibrations from ventilation fans and sources in

non-stationary phase locations dominate some cross-correlation functions and retard convergence to the seismic Green's functions. We developed a selective stacking scheme that identifies time periods when sources were located in stationary phase locations (and not monochromatic) and that would therefore contribute positively towards reconstruction of the seismic Green's functions. This stacking scheme, along with the highly scattering medium, enabled us to retrieve estimates of the seismic Green's functions between sensors.

After we identified and used periods of time where noise sources are in stationary phase locations (and not monochromatic), the cross-correlation functions show direct S-wave arrivals and, in the case of favorable orientation, weak P-wave arrivals for low frequency bands (below 100 Hz). We used the strong S-wave arrivals that are present for most of the cross-correlation pairs at low frequencies to perform an inversion for the 3D S-wave velocity structure of the area enclosed by the sensors. The 3D S-wave velocity structure shows the existence of a high and a low velocity zone that correspond to known ore bodies with different material properties.

We used the higher frequencies contained in the cross-correlation functions (above 200 Hz) to determine the average distance the seismic waves travel before they are scattered (mean-free-path). We found the value of the mean-free-path with the cross-correlation functions to be around 37 meters. This value compares well with the mean-free-path we found with numerical simulations when only mining excavations were included in the otherwise homogeneous model. This indicates that the mining excavations are predominantly responsible for the scattering in this environment.

The methodology we used in this study not only shows many potential applications in an underground mining environment, but also in any setting where sensors are installed at depth and broadband seismic noise is locally generated. Other potential applications include imaging and monitoring oil and gas reservoirs, hydraulic fracturing wells, CO_2 sequestration reservoirs, geothermal reservoirs and active fault zones with down hole sensors.

ACKNOWLEDGMENTS

We would like to thank Boliden's Garpenberg mine in Sweden for giving permission to use mine plans and data, the IMS research patrons for funding the project, Nikolai Shapiro for the useful discussions, the Center for High Performance Computing in Cape Town, South Africa for giving access to computing facilities to run simulations and process data and Joost van der Neut, Nori Nakata and 2 anonymous reviewers for useful suggestions and comments.

6.6 Appendix A

6.6.1 Inversion of the mean-free-path

As shown in (Dainty and Toksoz, 1977), the diffusion model describes the seismic energy for body waves as a function of space and time as

$$W(\mathbf{r}, t) = E_0 \left(\frac{4\pi V_s t}{3\eta_s} \right)^{-3/2} \exp[-\eta_i V_s t - \frac{3r^2 \eta_s}{4V_s t}], \quad (\text{A.1})$$

where E_0 is the source energy, V_s the S-wave velocity, r is the distance and η_i and η_s are the coefficients for intrinsic and scattering attenuation respectively. By choosing a reference distance, r_1 , so that $W_1(r_1, t_1) = 1 \text{ J m}^{-3}$ for $t_1 = 1 \text{ s}$ in the same way as Wegler and Luhr (2001) we can linearize the diffusion model as

$$\ln U(t) = a_1 + a_2 t + a_3 \frac{1}{t}, \quad (\text{A.2})$$

here $U(t) = \frac{W(\mathbf{r}, t)}{W_1} \left(\frac{t}{t_1} \right)^{3/2}$, $a_1 = \ln \left[\frac{E_0}{W_1} \left(\frac{4\pi V_s t_1}{3\eta_s} \right)^{-3/2} \right]$, $a_2 = -\eta_i V_s$ and $a_3 = -\frac{3r^2 \eta_s}{4V_s}$.

To use the linearized form of the diffusion model and to determine the scattering coefficients for different frequencies, we filter seismograms in different frequency bands and transform from ground motion to energy density, $W(\mathbf{r}, t)$, by

$$W(\mathbf{r}, t) = \sum_{i=1}^3 [f_i(\mathbf{r}, t)]^2 + [H\{f_i(\mathbf{r}, t)\}]^2, \quad (\text{A.3})$$

where $H\{f\}$ is the Hilbert transform of f and $f_i(\mathbf{r}, t)$ is the filtered i -component seismogram at location \mathbf{r} at time t . By now multiplying the energy density by the geometrical factor $t^{3/2}$ and taking the logarithm on both sides, we see that we have constructed the left-hand side of equation A.2 which is only linearly dependent on the three base functions 1, t and $1/t$. We can now perform a simple least squares inversion to fit the linear function with the parameters a_1 , a_2 and a_3 to the energy density. Since we know the S-wave velocity to a good degree, we can calculate the coefficients for intrinsic (η_i) and scattering attenuation (η_s) from a_2 and a_3 respectively.

When we are considering synthetic data, the uncertainty of the result of the scattering attenuation coefficient is reduced by the fact that the inversion is performed for two variables (a_1 and a_3) since the intrinsic attenuation is a specified value in our numerical model ($\eta_i = \frac{10}{V_s t_1}$). When using the microseismic data or the cross-correlation functions, where the intrinsic attenuation is unknown, our inversion is identical to that used in Wegler and Luhr (2001).

6.7 Appendix B

6.7.1 Determination of S-wave arrival with kurtosis estimator

To construct a 3-dimensional S-wave velocity model from the source-receiver functions constructed by cross-correlating ambient seismic noise, we have to determine the arrival times of these waves in the source-receiver functions. To do we use the commonly used method of constructing kurtosis estimators of the source-receiver functions (Langet et al., 2014). The standard definition of the kurtosis, K , of a signal, x , is given by:

$$K(x_1 \cdots x_n) = \frac{1}{n} \sum_{j=1}^n \left[\frac{x_j - \bar{x}}{\sigma} \right]^4, \quad (\text{B.1})$$

where \bar{x} is the mean of x and σ is the standard deviation of x . As discussed in (Langet et al., 2014), the maximum value of the kurtosis will be delayed in terms of the true first arrival. To reduce the bias (the delayed maximum of the kurtosis) we consider the arrival of the seismic wave to be the maximum of the positive time derivative of the K , defined as $dK_+ = \frac{dK}{dt}$ if $\frac{dK}{dt} \geq 0$ or $dK_+ = 0$ if $\frac{dK}{dt} < 0$. In Figure B.1 we show the result of the kurtosis estimator on one of the cross-correlation functions. The maximum of the Kurtosis gradient is still slightly delayed with respect to the S-wave arrival. To reduce this delay, we use the Akaike information criteria (AIC) as defined in (Zhang et al., 2003) in a window around the peak of the maximum of the Kurtosis gradient and locate the minimum of the AIC. As explained in (Zhang et al., 2003), this gives a better estimate of the exact S-wave arrival time.

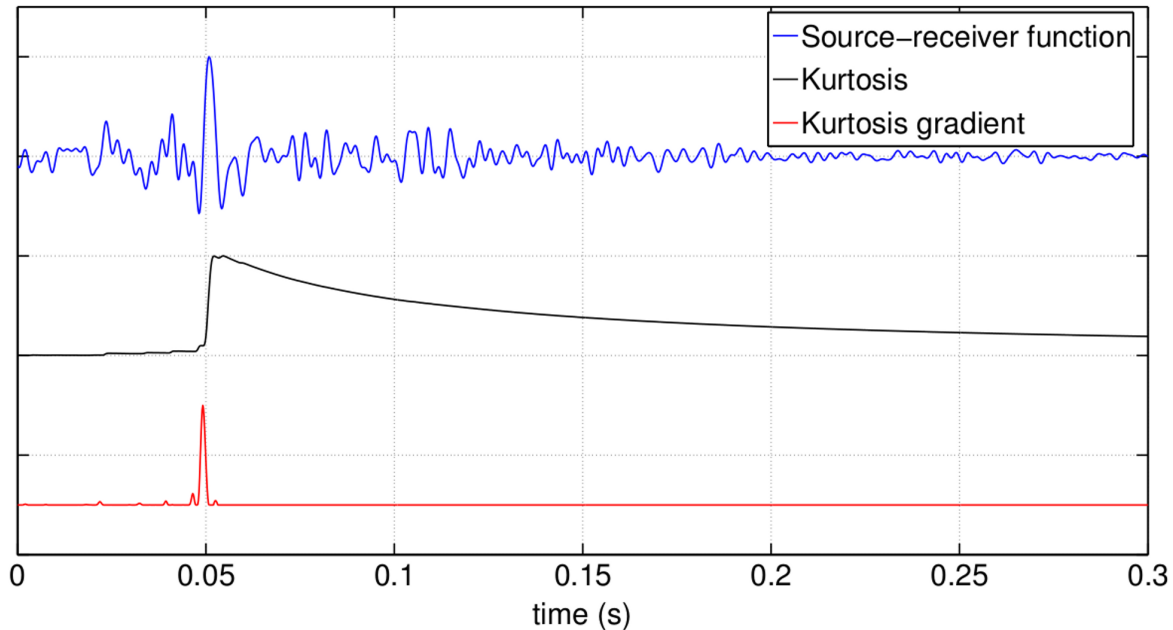


Figure 6B.1 – Determining the S-wave arrival by the kurtosis estimator. We consider maximum value of the positive derivative of the kurtosis estimator as the arrival of the S-wave.

Automatic picking and detection of seismic waves is hard for a number of reasons (see for example the introduction of [Langet et al. \(2014\)](#)). For our study it is much simpler, since we know the S-wave velocity, start time and position of the virtual sources to a good degree. In other words, we only need to search for the S-wave arrivals in a small time window.

6.7.2 3D Tomography

To invert for the three-dimensional velocity model, we divided the area enclosing all source-receiver pairs into blocks. The size of these blocks will determine the resolution of our 3D velocity model. The volume enclosing the sensors are divided into blocks of 8000 m^3 ($20 \text{ m} \times 20 \text{ m} \times 20 \text{ m}$). When picking the arrival times of the S-waves, we considered waves of frequency between 20 and 100 Hz. S-waves with frequency of 100 Hz have a wavelength of roughly 40 m. Bearing this in mind, we spatially smoothed the final velocity model in 3D with 40 m smoothing windows, since smaller structures can not be resolved with these wavelengths.

To ensure that the arrival times of the S-waves can accurately be picked, the inter-sensor distance needs to be larger than the wavelengths of the S-waves so that signals are not in the near-field. For S-waves of 100 Hz the wavelengths are roughly 40 m. Bearing

this in mind, sensor pairs with inter-sensor distance of more than 100 m was used to invert for the S-wave velocity model. Of the 153 cross-correlation pairs, 144 had inter-sensor distances larger than 100 m. Of these 144 possible S-wave arrivals, 121 S-waves were successfully picked by the Kurtosis estimator. For the 23 pairs that didn't have successful picks, the peak of the Kurtosis estimator was less than a predefined threshold.

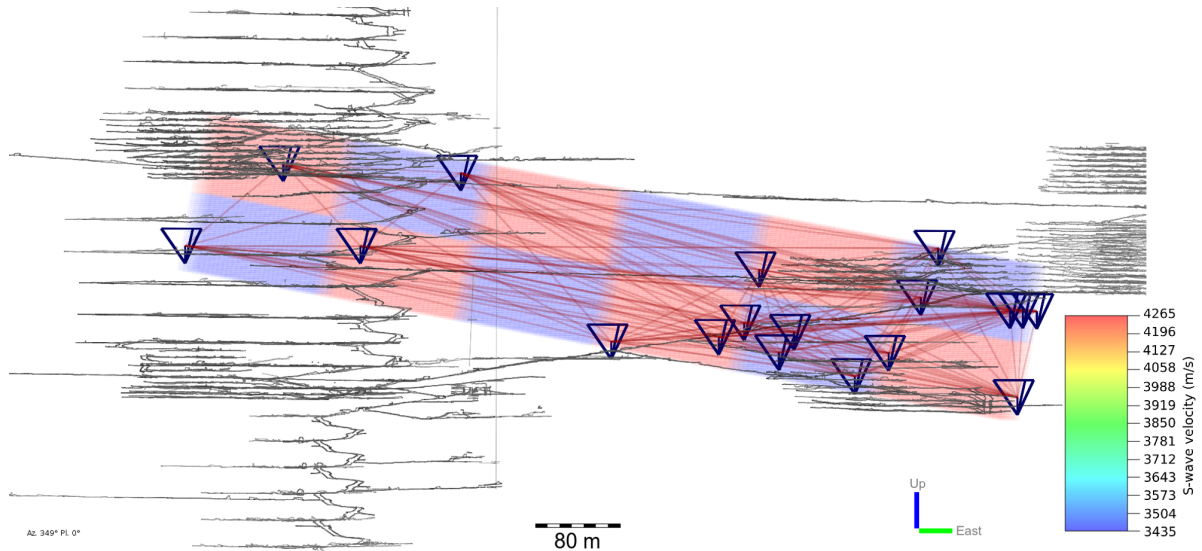


Figure 6B.2 – 2D cross section of the synthetic 3D velocity model used to create the Green's functions for the checkerboard resolution test.

In order to obtain realistic results, the solution is constrained to a certain range. Since large deviations in the S-wave velocity is not expected at these depths, the solution is constrained to the range $[0.8 \times v_S; 1.2 \times v_S]$. In Figure 12 we can see that the S-wave picks that were obtained by the Kurtosis estimator fall comfortably inside this constraint. If the constraint is eased, some of the S-wave picks fall outside the 20% range and cause random scatter in the final velocity model. This indicates that if the constraint is too wide, the Kurtosis estimator could mistake other local maxima in the cross-correlation function as the S-wave arrivals. The value of 20% was chosen because it resulted in a large reduction in travel time misfit (22%), while not causing random scatter in the final velocity model.

An important point to note here is that straight rays are assumed between sensors. Although this assumption is incorrect, it is reasonable in this case for two reasons. Firstly, the velocity variations are expected to be small in magnitude for the bulk medium. Secondly, the areas where the velocity contrasts are high, like the mining excavations, are spatially small enough so that the low frequency components of the direct arrivals in the estimates of the seismic Green's functions will not be affected by them (see Figures 2,5 and 11). To test if this assumption is valid, a numerical checkerboard velocity model is constructed. Synthetic Green's function between sensors are generated with full

waveform modeling (see numerical modeling section), the arrival times of the S-waves are picked and the 3D inversion is performed to see if the input velocity model can be recovered. If the correct model is recovered, it will show that the straight-ray assumption is reasonable in this case. Although we made no direct estimates of the picking error, if the synthetic test reasonably recovers the checkerboard velocity model, we can also assume that the picking error is negligible for current purposes.

6.7.3 Checkerboard resolution test

To assess the achievable resolution of the S-wave velocity inversion, we introduced blocks of consecutive high and low velocity zones in our velocity model, constructed synthetic Green's functions with numerical simulations, picked the arrival times of the synthetic S-waves and finally attempted to retrieve the blocks of high and low velocity zones. All the steps used in this synthetic test mimic the steps described in the manuscript for the cross-correlation functions.

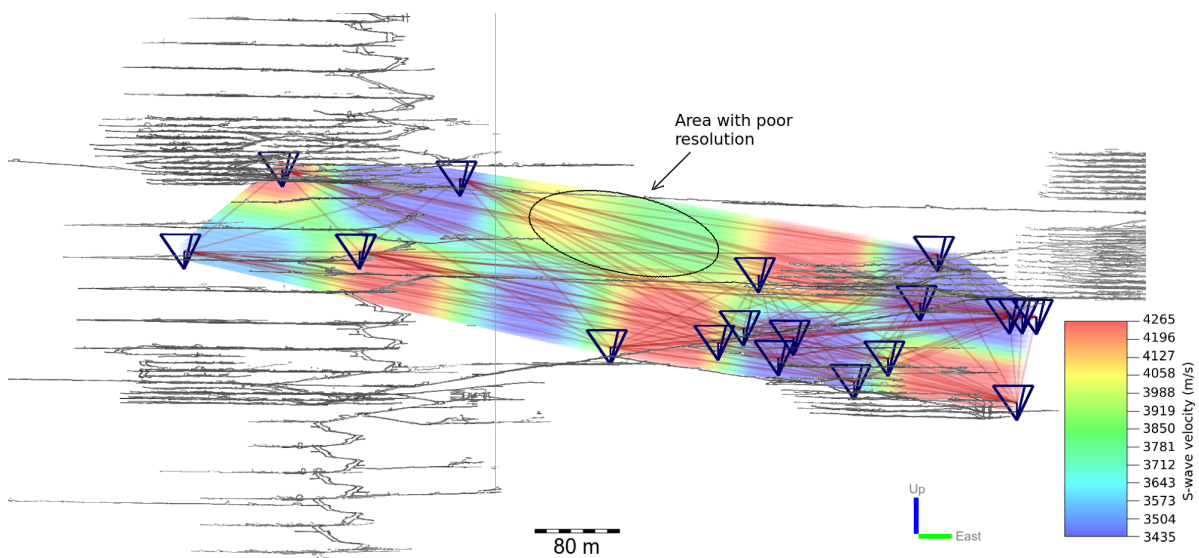


Figure 6B.3 – 2D cross section of the result from the inversion of data generated by the synthetic checkerboard velocity model. This shows the achievable resolution with the number of successful picks made of the S-wave arrivals of the cross-correlation functions. The outer edges of the checkerboard model can not be retrieved since no rays pass through them. For the interior of the array, the correct velocities structures were mostly recovered.

The difference between the velocity model obtained by the inversion and the actual synthetic checkerboard velocity model used to generate the seismograms indicates the areas where the achievable resolution is poor. It also indicates if the straight ray assumption is reasonable and if the S-wave picking algorithm is accurate. The blocks were chosen

to be $3.4 \times 10^6 \text{ m}^3$ ($150 \text{ m} \times 150 \text{ m} \times 150 \text{ m}$) and the variations used were 10% higher and lower than the background S-wave velocity, as shown in Figure B.2. These parameters were chosen bearing in mind the maximum velocity excursion we are expecting from the real data and the inter-sensor distance.

In order to do a realistic resolution test, only the 121 source-receiver functions for which we could find accurate S-wave picks in cross-correlation functions with real data are considered. The results of the checkerboard inversion are shown in Figure B.3. Almost all of the high and low velocity zones are recovered except for the section between the Kaspersbo and Lappberget ore bodies, which was to be expected due to the limited ray orientations of this section.

Part IV

Measuring seismic velocity variations

Chapter 7

Measuring seismic velocity variations in an underground mine

After having shown that the seismic Green's functions can be retrieved between sensors in an underground mine, I now turn my attentions to measuring time dependent changes in seismic velocity. In my second paper, I show that the reconstructed Green's function can be used to make robust, regular estimates of the seismic velocity variations in the vicinity of the seismic sensors. I measured the time dependent seismic velocity variations during a blast in a tunnel in the underground mine. I also investigated the timing and location of aftershocks and the expected static stress change from the blast. This experiment offered the unique opportunity to provide insights into the effects of a large dynamic stress perturbation on the surrounding medium, like the mechanisms of earthquake triggering.

7.1 Preliminary methods and parameters

Before I show the final results of the experiment, I will briefly discuss some of the technical parameters I needed to investigate, before applying the methods developed to measure velocity variations in crustal seismology in an underground mine.

7.1.1 Determining window for measuring velocity variations

As shown in Chapter 6, many of the sources present in an underground mining environment are monochromatic and stable (for instance ventilation fans). While I have developed a processing scheme that succeeds in recovering good estimates of the direct arrivals of the seismic Green's functions, I have to make sure that the coda parts of the cross-correlation functions are representative of real multiply scattered seismic waves and not an aliasing effect of monochromatic signals. To investigate this, I have to ensure that the seismic waves decay exponentially as expected (Aki, 1969; Aki and Chouet, 1975). If I incorrectly mistake the aliasing of a monochromatic signal as stable seismic coda, it will lead to an underestimation of the seismic velocity change, because the changes measured in the sections that are dominated by the monochromatic signal will tend to zero.

In Figure 7.1, I show the stack of all correlation functions for one station pair for the entire time period, along with its envelope. The coda part of the cross-correlation function decays exponentially up to roughly 0.4 seconds positive lag-time and -0.6 seconds negative lag-time. After these times, the coda waves do not decay exponentially and the envelope flattens out. From this figure, it appears likely that the cross-correlation function only represents real scattered seismic waves between -0.6 and 0.4 seconds and the apparently stable coda at larger lag-times is an aliasing effect from monochromatic sources. I investigated the envelope of the total stack of each of the 153 cross-correlation functions and in the following section used the windows that represent real scattered seismic waves to calculate the travel time variations for each station pair.

7.1.2 Calculation of relative velocity variations

In the next section, I construct hourly estimates of the seismic Green's function and measure relative travel time variations between them by using the moving-window cross-spectral technique (Clarke et al., 2011). The method is a variation of CWI (see Section 3.2) and entails calculating delay-time shifts between two cross-correlation functions in the frequency domain for different lag-time windows and performing a weighted least squares linear regression to estimate the travel time change between the two cross-correlation functions. In the linear regression, the delay-time measurements are weighted

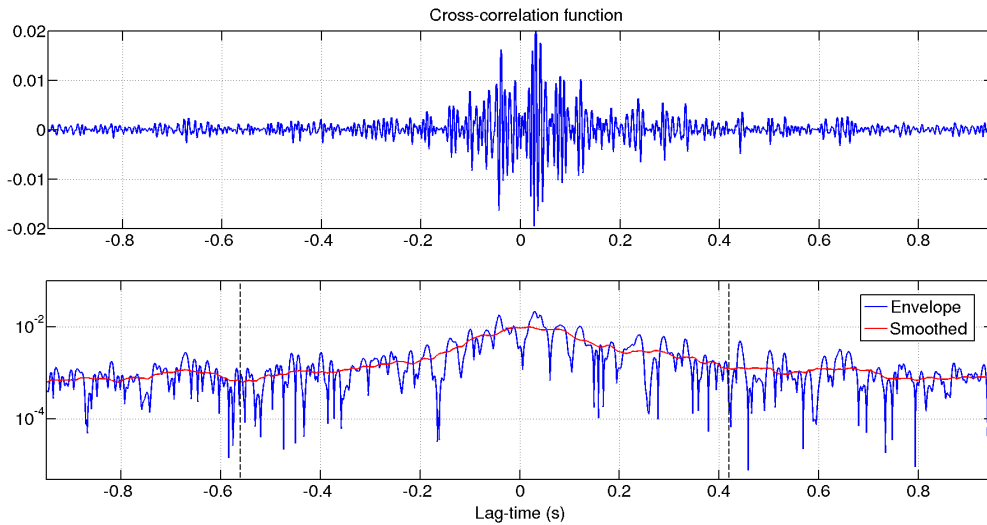


Figure 7.1 – Stack of cross-correlation functions for the entire 25 day period for one station pair (top) and the envelope and smoothed envelope (bottom). The coda part of the cross-correlation function decays exponentially up to -0.6 and 0.4 seconds lag-time, after which the aliasing of the monochromatic signals prevent the coda waves to decay as expected.

by the coherence of the cross-correlation functions in the corresponding windows. The frequency band that resulted in the most stable measurements was found to be 100 - 240 Hz. The low frequency band (≤ 50 Hz) was found to be particularly affected by the aliasing effect of the monochromatic sources I described in the previous section.

In Figure 7.2, the measurement of the travel time shift between two cross-correlation functions is shown. The measurements up to different maximum lag-times are indicated on the figure, namely up to 0.5 second lag-time and up to 0.95 second lag-time. The two measurements illustrate the effect that I suggested in the previous section - after 0.5 seconds the coda part of the cross-correlation function is no longer representative of real scattered seismic waves travelling between seismic sensors, but an artefact of monochromatic signal aliasing. As a result, if I measure the travel time variations up to 0.5 seconds, I find a shift of 2.5×10^{-4} , whereas if I measure up to 0.95 seconds, I only find a shift of 1.2×10^{-4} . The aliasing effect of the monochromatic signals that dominate at longer lag-times cause the travel time change estimate to be underestimated, because the cross-correlation functions are very coherent during these times, but the delay time measurements indicate low values.

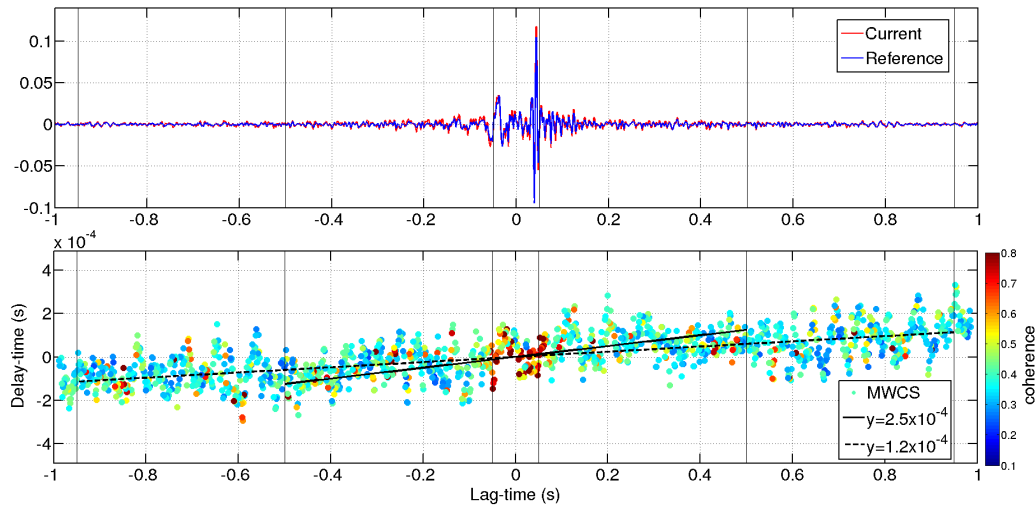


Figure 7.2 – Travel time variations measured with the MWCS technique for two cross-correlation functions. The colors of the points (bottom) indicate the coherence of the cross-correlation functions in each lag-time window. After 0.5 seconds there are points with high coherence, but with small delay times. This is due to the aliasing of monochromatic signals.

7.1.3 Inversion for time dependent velocity changes

In order to obtain the time dependent velocity variations for an entire period, it is common to measure changes between individual cross-correlation functions and an arbitrary reference cross-correlation function. The reference cross-correlation function can be the average of all available cross-correlation functions or the average of a subset. In an environment where it is possible that the cross-correlation functions can change due to medium or source changes, using this method could introduce large errors if the cross-correlation functions become incoherent over time (Hillers et al., 2014).

In the subsequent section, I will use a way to determine the time dependent seismic velocity variations that eliminates the need to introduce an arbitrary reference function. In this method, the travel time variations between each cross-correlation function and all the other cross-correlation functions are measured and a Bayesian least squares inversion is performed to find the time dependent seismic velocity variations (Breguier et al., 2014). This method requires $\frac{N \times (N-1)}{2}$ measurements compared to N measurements when using an arbitrary reference. However, the advantage of this method is that all measurements, weighted by their coherences, are inverted simultaneously, which reduces the potential errors introduced by changing cross-correlation functions. This method could be of particular use if the cross-correlation functions are not coherent for the entire time period.

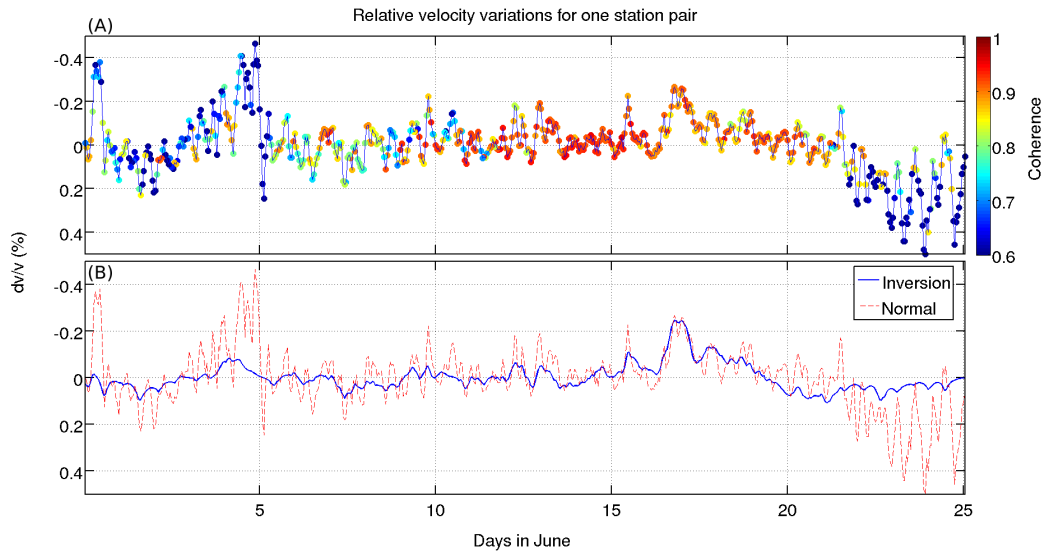


Figure 7.3 – Travel time variations for one station pair. The travel time variations are shown using the standard stack and compare method (top). The color indicates the coherence of the value and is indicative of the error. The large fluctuations are obtained when the coherence is low. The travel time variations obtained by inverting for the travel time curve are shown in the bottom panel along with the standard method. Since the inversion takes the coherence of each measurement as a weight, the large fluctuations when the coherence is low for the standard method disappears.

In Figure 7.3, the relative velocity variations for one station pair using both methods are shown. In panel a, it is clear that when using a reference consisting of all cross-correlation functions, the travel time variations are large when the coherence between the current cross-correlation function and reference cross-correlation function is low (see days 3 to 5 or days 22 to 25 for instance). In panel b, the travel time variations are shown when using the Bayesian least squares inversion. The large fluctuations during times of low coherence disappear, so that the only fluctuations that are consistent for the two methods are when the coherence is high for the arbitrary reference measurement.

Investigation of coseismic and postseismic processes using in situ measurements of seismic velocity variations in an underground mine

Gerrit Olivier, Florent Brenguier, Michel Campillo, Philippe Roux, Nikolai Shapiro, Richard Lynch

Geophysical Research Letters, 42, 9261–9269, doi:10.1002/2015GL065975.

Key points:

- Seismic velocity variations were examined with seismic noise correlations in a mine during a blast.
- A sudden decrease, gradual relaxation and permanent changes in the seismic velocity are observed.
- Elastic modelling shows that the permanent changes in velocity are due to changes in static stress.

Abstract: The in situ mechanical response of a rock mass to a sudden dynamic and static stress change is still poorly known. To tackle this question, we conducted an experiment in an underground mine to examine (1) the influence of dynamic and static stress perturbations on seismic velocities, (2) elastic static stress changes, and (3) induced earthquake activity associated with the blast and removal of a portion of hard rock. We accurately (0.01%) measured seismic velocity variations with ambient seismic noise correlations, located aftershock activity, and performed elastic static stress modeling. Overall, we observe that the blast induced a sudden decrease in seismic velocities over the entire studied area, which we interpreted as the damage due to the passing of strong seismic waves. This sudden process is followed by a slow relaxation lasting up to 5 days, while seismic activity returns to its background level after 2 days. In some locations, after the short-term effects of the blast have subsided, the seismic velocities converge to new baseline levels and permanent changes in seismic velocity become visible. After comparing the spatial pattern of permanent seismic velocity changes with elastic static stress modeling, we infer that the permanent seismic velocity changes are due to the change in the static volumetric stress induced by the removal of a solid portion of rock by the blast. To our knowledge, this is the first observation of noise-based permanent seismic velocity changes associated with static stress changes.

7.2 Introduction

The behaviour of the crust shortly after earthquakes has been the subject of numerous studies but many co- and post-seismic processes remain poorly understood. These processes are important to properly model and understand the behaviour of faults and

earthquake cycles. Damage and healing of the bulk rock mass, post-seismic deformation and the mechanisms of triggering are still not well understood (Scholz, 2002; Gonzalez-Huizar and Velasco, 2011; Johnson et al., 2015). This is partly due to the complexity of the stress distribution and heterogeneities in the fault zone and partly due to the lack of information and measurements close to faults. Laboratory stick slip experiments have provided insights into earthquake cycles and dynamic triggering (Johnson and Jia, 2005), but real faults have complex frictional properties and can be triggered by environmental factors like groundwater depletion (Amos et al., 2014), fluid pressure (Shapiro et al., 2003), dynamic stress perturbations from large earthquakes (Gomberg et al., 2001; Hill et al., 1993; Gomberg et al., 2004) and quasi-static stress changes from slow-slip events (Bouchon et al., 2011), which makes dynamic triggering and real earthquakes hard to model (Bakun and Lindh, 1985).

The mechanism of dynamic triggering is not well understood since the dynamic strain from large earthquakes is small beyond a few fault radii (Gomberg et al., 2003). Often delay times of minutes to hours between the initial large event and the "triggered" microseismic events are reported, which makes it hard to attribute the triggering of the latter to the former. Earthquakes can be considered to be dynamically triggered if the start time is within seconds of the arrival of the direct waves of the triggering event, allowing for a reasonable nucleation time (Tape et al., 2013). In other cases, the occurrence of triggered events are attributed to changes in the elastic static stress induced by the large earthquakes, where the relatively small change in elastic stress by a large earthquake moves another fault closer to failure (Stein, 1999; Mantovani et al., 2010). This mechanism allows for much larger delay times between the initial earthquake and triggered earthquakes.

To better understand how the crust responds to large earthquakes, there is a need to improve current methods for measuring in-situ stress change and damage near active faults. Strain cells, tiltmeters and extensometers have all been used in active fault zones, but the measurements are very localised and do not provide a complete picture of what is happening at depth.

On the other hand, seismic velocities of rock are sensitive to changes in applied stress (Nur, 1971; O'Connell and Budiansky, 1974; Lockner et al., 1977). The relation between applied stress and seismic velocity has been attributed to the opening and closing of microcracks, which will decrease and increase the seismic velocities, respectively. If the seismic velocity variations can be determined to the required accuracy, known stress changes like the deformation of the earth's crust due to the earth tides or the stress caused by atmospheric air pressure changes can be used to calibrate these stress-induced velocity variations (Fazio et al., 1973; Reasonberg and Aki, 1974; Leary et al., 1979). Unfortunately the sensitivity of seismic velocity to applied stress is low (Yamamura et al., 2003), so that the seismic velocities have to be measured very accurately to be able to detect the processes of interest.

Over the last decade a new method has emerged that eliminates the need for an active source or repeating earthquakes. Cross-correlating ambient seismic noise can be used to construct estimates of the seismic Green's function between sensors pairs, effectively turning one of the sensors into a virtual source (Shapiro and Campillo, 2004; Roux and Kuperman, 2004; Sabra et al., 2005b; Campillo, 2006). This creates stable virtual seismic signals with which we can regularly measure small changes in the seismic velocity (Sens-Schönfelder and Wegler, 2006). With this method, it has been shown that large earthquakes have measurable effects on seismic velocity. Significant co-seismic velocity drops have been reported along with a gradual relaxation back to pre-seismic levels (Brenguier et al., 2008a; Cheng et al., 2010). The velocity drops have been shown to be located in the rupture zone of the large event or in areas where the susceptibility of seismic velocities to stress change is large, like volcanic regions with high pore pressure. Significant precursory velocity changes have also been reported for volcanic eruptions (Brenguier et al., 2008b), mud landslides (Mainsant et al., 2013) and even earthquakes (Niu et al., 2008).

In this study, we investigate whether accurate measurements of seismic velocity variations can provide insights into the immediate and long-term effects of a sudden dynamic stress perturbation on the surrounding rock. The experiment was conducted in an environment that is well instrumented and fits naturally between laboratory and crustal scale - an active underground mine.

7.3 Data and methods

In an effort to understand the immediate and long-term effects of a sudden dynamic stress perturbation and elastic static stress changes on the surrounding medium, we conducted a small scale experiment in an active underground mine while recording continuous seismic data with the standard mine IMS microseismic monitoring network. The experiment consisted of simultaneously detonating multiple explosives in a 20 m^3 volume in a mining tunnel and examining the effects on the surrounding rock by considering triggered seismicity, seismic velocity variations and modeled elastic static stress behaviour. The blast produced peak ground motions of up to 30 mm/s on geophones roughly 50 m away.

The location of the blast and subsequent aftershocks relative to the mining tunnels and sensors are shown in Figure 1. The aftershocks are not grouped evenly around the location of the blast, but appear clustered. The locations of the aftershocks stay reasonably constant over a 2-day period and no convincing migration patterns were observed. The time distribution of the aftershocks follows Omori's law with a p value of

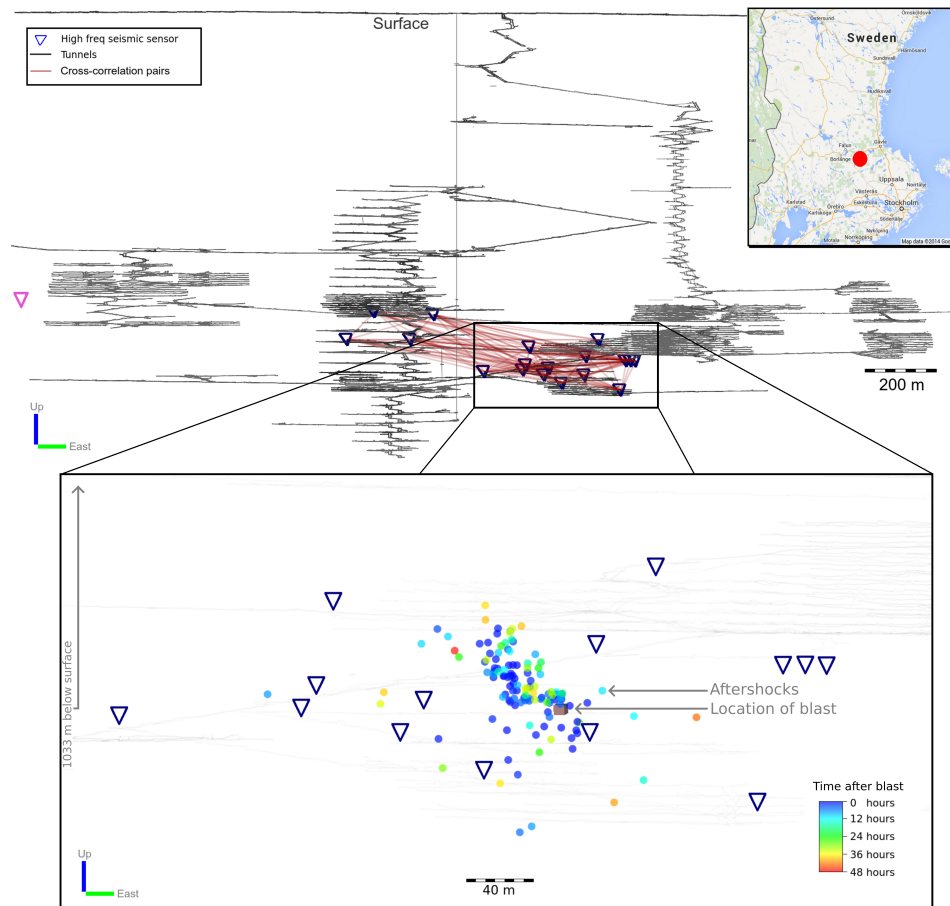


Figure 7.4 – Side view of the mine plans of Boliden’s Garpenberg mine in Sweden along with the locations of the seismic sensors (top). Zoomed view of the location of the blast and the proceeding aftershocks (bottom). The aftershocks are coloured by the amount of time elapsed after the blast. The aftershocks are not located homogeneously around the area where blasting occurred and no clear migration pattern is visible.

0.48, which seems low but is reasonable in a mine setting (Vallejos and McKinnon, 2010).

To better understand the immediate effect of the blast on the surrounding medium and the mechanism behind the aftershocks, we examined hourly measurements of the seismic velocity variations. Most of the previous studies where ambient seismic noise correlations have been used to measure seismic velocity variations have used surface seismic sensor arrays. In these scenarios, the surface waves from the interaction of the ocean waves with the solid earth provide stable seismic noise sources that can be used to make daily measurements of seismic velocity variations. However, these surface waves have limited sensitivity and resolution for structures located at depths larger than the considered wavelengths. Therefore, they are not ideally suited for many sub-surface applications.

Recently it has been shown that the noise generated by mining activity can be used to construct good estimates of the seismic Green's function if the noise is carefully selected (Olivier et al., 2015). This potentially creates a stable, repeatable signal with which we can regularly measure small seismic velocity variations in an underground mining environment. In order to measure small changes in the seismic velocity, we want to construct robust, regular estimates of the seismic Green's functions between sensors.

The processing scheme that we employed in this study is a variation of the method described in detail in Olivier et al. (2015) and only briefly outlined here. Every hour of continuous data is split into 10 second sections, spectrally whitened between 20 and 240 Hz and one-bit normalised. The resulting sections are cross-correlated among station pairs. If the 10 second cross-correlation function (CCF) for a specific station pair has a signal-to-noise ratio of 2 or more in a window around the lag-time corresponding to the expected arrival time of the primary S-wave, the CCF is added to the hour stack for this station pair. The resulting stack is used as the hourly CCF.

This processing scheme succeeds in recovering stable estimates of the seismic Green's function every hour. All CCFs for one station pair are shown in Figure 7.5. Each coloured line in the bottom part represents an hourly CCF while the average for the entire time period is shown at the top of the figure. A remarkable feature visible here is the temporal stability of the cross-correlation functions, especially in the coda of the CCFs. The coda of the CCFs are expected to be more stable as a function of time than the direct arrivals. This is due to the fact that the direct arrivals are more sensitive to changes in seismic sources than the coda when constructing CCFs (Froment et al., 2010).

These stable hourly estimates of the seismic Green's function are used to measure time dependent relative seismic velocity variations by using the moving-window cross-spectral technique (Poupinet et al., 1984; Clarke et al., 2011). This method is only used to measure changes of the seismic velocity in the coda of the CCFs. By excluding the direct arrival when measuring the relative velocity variations, we reduce the errors due to potential changes in the seismic sources. Relative velocity variations were measured in the frequency band 100-240 Hz and in the lag-time window between 0.02 s after the expected arrival of the direct S-wave and up to 0.4 seconds. A large number of different processing parameters were tested and these particular parameters resulted in the smallest errors.

In order to obtain the time dependent velocity variations for an entire period, it is common to measure changes between individual CCFs and an arbitrary reference CCF. The reference CCF can be the average of all available CCFs or the average of a subset. In an environment where it is possible that the CCFs can change due to medium or source changes, the use of this method could introduce large errors if the CCFs become

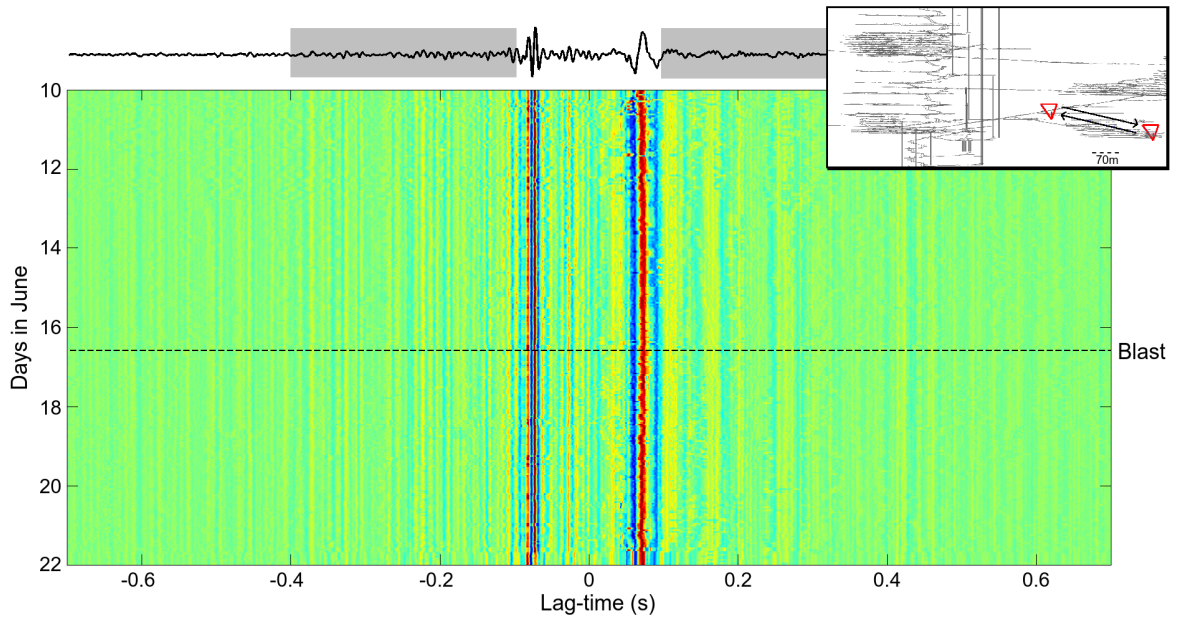


Figure 7.5 – Stack of all cross-correlation functions (top) and hourly cross-correlation functions for one station pair for the 12 day period (bottom). The time of the blast is indicated by a black dotted line. The cross-correlation functions appear stable for up to at least 0.7 second lag-time. The inset indicates which stations were used to construct the cross-correlation functions. The grey rectangles indicate the windows that were considered when measuring the velocity variations (after the direct S-wave, up to 0.4 seconds).

incoherent over time (Hillers et al., 2014).

Recently, a new way to determine the time dependent seismic velocity variations has been proposed that eliminates the need to introduce an arbitrary reference function. In this method, the travel time variation between each CCF and all the other CCFs are measured and a Bayesian least squares inversion is performed to find the time dependent seismic velocity variations (Breguier et al., 2014). This method requires $\frac{K \times (K-1)}{2}$ measurements compared to K measurements when using an arbitrary reference. However, the advantage of this method is that all measurements, weighted by their coherences, are inverted simultaneously, which reduces the potential errors introduced by a changing CCF.

In order to locate the regions where the velocity variations occur, we average the velocity variations for the $N - 1$ cross-correlation pairs involving a specific sensor (where N is the number of sensors). The seismic velocity variations are measured in the frequency band 100-240 Hz. At these frequencies the seismic wavefield is diffuse due to the scattering caused by the mining excavations and tunnels (Olivier et al., 2015). As a result the sensitivity kernels, based on diffusion approximations, has a pronounced maximum close to the sensors. The average of $N - 1$ velocity variations involving a specific sensor

is therefore a good approximation for the velocity change at this sensor. This averaging process also decreases the errors in the apparent seismic velocity variations introduced by changing noise source locations, since the sensor pairs are orientated at different azimuths to the changing noise sources.

7.4 Results

The relative velocity variations averaged for one sensor is shown in Figure 3 along with the temporal distribution of the aftershocks. The aftershocks occur minutes to hours after the blast (see bottom of Fig. 3). This is much later than the arrival of the direct seismic waves, which indicates that the microseismic events are not directly triggered by the passing dynamic strain wave. The spatial clustering and delayed timing of the aftershocks indicate that they were either triggered by the changed static stress or by another mechanism.

Three remarkable features are visible in the relative velocity variation curve. Firstly, an immediate decrease of roughly 0.025 % is visible at the time of the blast. The velocity drop is followed by a slow relaxation that takes roughly 5 days. For large earthquakes in a crustal setting, the relaxation can take years (Brenguier et al., 2008a). Finally, after 5 days the velocity has converged to a new baseline value.

The mechanism by which seismic velocities decrease in response to dynamic stress perturbations is often described as related to damage, that is the opening of cracks or motions at the grain joints. Therefore, we attribute the immediate velocity drop to damage and plastic deformation induced by the strong shaking of the production blast, whereas the subsequent relaxation is interpreted as the closing of the newly opened cracks and fractures by the confining static stress. Our results are very similar in shape to laboratory experiments (e.g. Figure 4d in Johnson and Jia (2005)) showing the so-called instantaneous weakening (fast dynamics) followed by a gradual healing of the medium (slow dynamics).

Arguably the most interesting feature of the velocity variations in Figure 3 is that the seismic velocity ultimately increases in response to the blast for this sensor. This result might seem unusual, since it is expected that the seismic velocity will decrease in response to the weakening of the medium by the blast. For other sensor locations, we do see a permanent decrease in the seismic velocity after the relaxation. In our opinion, the only physical mechanism for an increase of the seismic velocities in this scenario could be an increase in elastic static stress due to the removal of a piece of solid rock by the blast. Such modifications to excavations combine with the virgin stresses to produce zones of increased stress as well as zones of decreased stress.

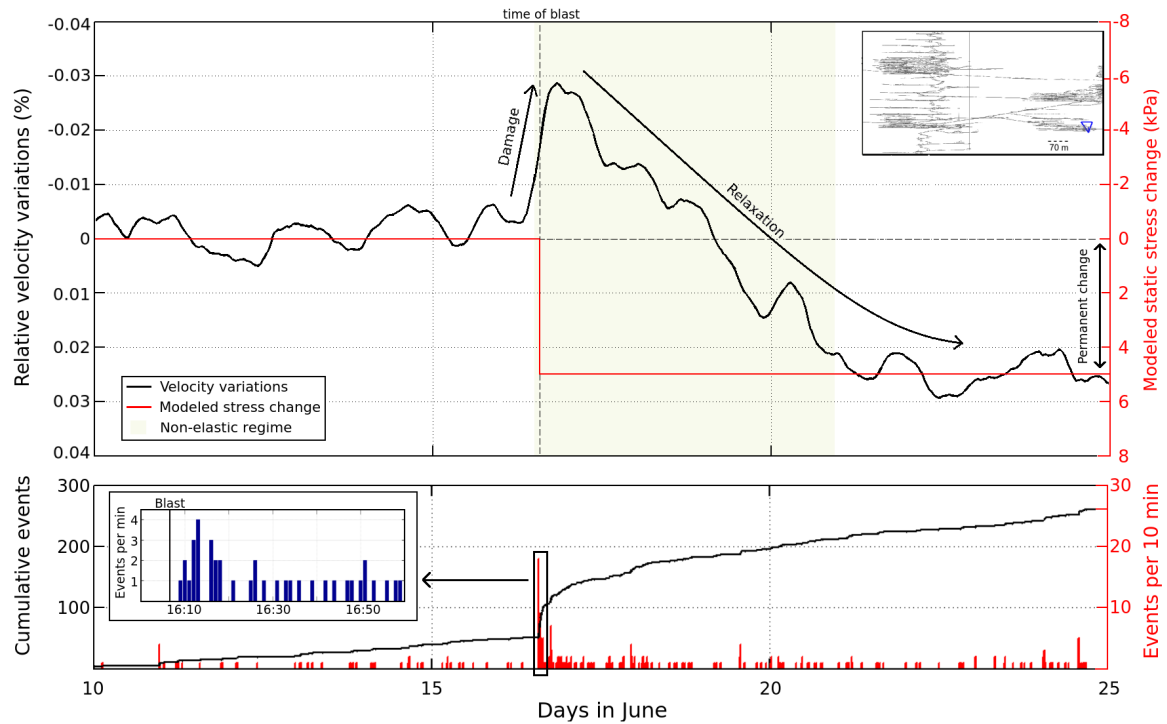


Figure 7.6 – Seismic velocity variations averaged for one sensor (top). Three features are present: an immediate decrease during the blast, relaxation that takes up to 5 days after the blast and the permanent change in baseline of the seismic velocity. The bottom figure shows the cumulative number of events recorded during the 15 day period, along with the number of events recorded every 10 minutes. The inset shows a zoomed view of the hour in which the blasting took place. The seismic activity rate peaks at 7 minutes after the blast.

To estimate the 3D elastic stress changes due to the blast, we constructed and solved an elastic static stress model. This entails creating a 3D model with the mined-out regions enclosed by free-surfaces and surrounded by homogeneous isotropic rock and using the displacement discontinuity boundary-element method (Jager and Ryder, 2002). In short, this method estimates the value of the stress at each element in our model as the sum of the Kelvin solutions for the stress induced at this element by the virgin stress acting individually on each of the other elements in our model. This process is repeated after a 20 m^3 piece of rock is removed in the location where blast was detonated and the difference between the two model solutions represents the modeled static stress change. The virgin stress used in the model was measured by CSIRO cell over-coring measurements, and measured values of the Young's modulus and Poisson's ratio were used (Boliden, 2014).

To approximate the values of the velocity change between sensors we used a 3D triangulation-based linear interpolation method. To visualize the velocity changes, iso-

MEASURING SEISMIC VELOCITY VARIATIONS IN AN UNDERGROUND MINE

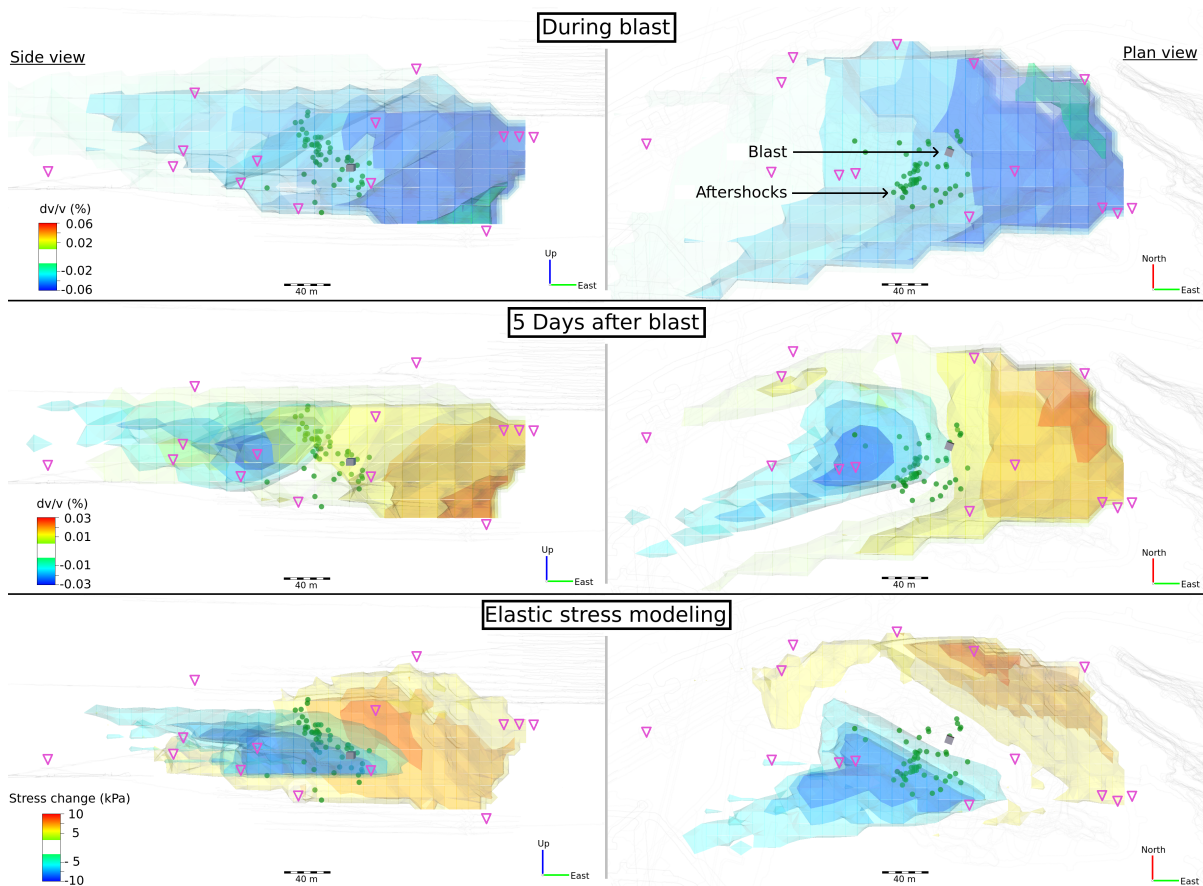


Figure 7.7 – Comparison of iso-surfaces of the immediate change in the seismic velocity, the permanent change in the seismic velocity and the modeled volumetric stress change. The permanent change in the seismic velocity (5 days after blast) and the modeled static stress change are qualitatively in agreement for most locations.

surfaces of the interpolated values were created. Even though it is possible to create high-resolution 3D images of the modeled elastic static stress changes, we chose to only calculate the elastic static stress changes in the vicinity of each seismic sensor and use the same 3D interpolation and visualisation method used to visualize the velocity changes. This was done in order to minimise the influence of the interpolation method on our final interpretations. The average of all elements within 10 m of each sensor was used as the value of the modeled stress change at this sensor.

Figure 4 shows the locations of the blast and aftershocks along with immediate changes of the seismic velocity (A), the permanent changes of the seismic velocity (B) and the changes in the modeled elastic static stress (C).

The permanent change in seismic velocity and the modeled change in volumetric stress $\frac{1}{3}(\sigma_{11} + \sigma_{22} + \sigma_{33})$ are generally in agreement for most locations - there is an in-

crease in modeled volumetric stress to the north-east of the blast and a decrease to the south-west. A comparison of the relative velocity change to the modeled stress change indicate a velocity-stress sensitivity of the order of $10^{-8}/\text{Pa}$, which compares well with values reported in literature (see table in [Yamamura et al. \(2003\)](#)). The similar spatial distribution, along with the plausible value for the velocity-stress sensitivity, indicates that the change in baseline of the seismic velocity could be a good proxy for the change in elastic static volumetric stress.

Although the comparison between the two independent methods are qualitatively convincing, there are a few areas where the methods are not in complete agreement. The difference is especially clear in the area where the aftershocks are clustered (directly to the south of the blast in Fig. 4). The presence of fractured zones, as indicated by the spatial clustering of the aftershocks, could explain the discrepancy between the modeled stress change and the observed velocity changes. In other words, the homogeneous static stress model could be too simple to accurately represent the complex rock mass in these zones.

The majority of the aftershocks are clustered in an area where we see an immediate decrease in the seismic velocity and also a change in modeled elastic static stress. However, the aftershocks are not necessarily located in areas where we see the largest change in either of these quantities. This could indicate that the aftershocks occur on an optimally orientated fault that was activated by the changes in elastic static stress from the blast. The location of the cluster of aftershocks could also indicate that this area was highly stressed before the deformation and more susceptible to induced fracturing. This observation is consistent with previous results obtained in a mine environment ([Castellanos and Van der Baan, 2015](#)).

7.5 Conclusions

An experiment was performed in which a blast was detonated in a tunnel in an underground mine while seismic velocity variations were accurately (0.01 %) measured with ambient seismic noise correlations. Additionally, aftershock activity was examined and the influence of the removal of a piece of solid rock was estimated with elastic static stress numerical modeling. The majority of the aftershocks were delayed with respect to the passing of the dynamic waves from the blast, while the locations of the aftershocks appeared clustered and not homogeneously spread around the blast location.

A significant velocity drop is visible during the time of the blast, which is interpreted as a consequence of damage and plastic deformation. These non-elastic effects are healed by the confining stresses over a period of 5 days until the seismic velocity converges to a new baseline level. The instantaneous weakening and gradual healing observed from

the velocity variations are qualitatively similar to results reported in laboratory studies. The change in the baseline level of the seismic velocity before and after the blast indicates a change in the static stress that is comparable to the results of elastic static stress modelling. The differences between the elastic model predictions and the seismic velocity variations could be due to zones of fractured rock, suggested by the spatial clustering of the aftershocks, that are not represented by the simple homogeneous isotropic elastic model.

Acknowledgements

We would like to thank Boliden's Garpenberg mine in Sweden for giving permission to use the mine plans and data; the IMS research patrons for funding the project; P. Johnson for the useful discussions and G. Basson for help with the static stress modelling. The work of N. Shapiro was supported by the Russian Science Foundation (grant 14-47-00002).

Conclusions

In this dissertation, I presented the results of my research into applying noise-based methods to seismic data recorded in mines. The application of this method is of great interest as it could potentially be used to improve safety in mines and increase productivity. Since many mines have modern seismic monitoring networks, this method could be applied at relatively low cost, because no extra hardware is required and data is used that would normally be discarded.

In Chapter 2 and 3 I introduced the fundamental methods and concepts that I used throughout my dissertation. I then showed the past imaging and monitoring applications of the method in crustal seismology in Chapter 4. The diverse range of environments where this method has been successfully applied, served as encouragement that the method could be applied in mines. In Chapter 5, I discussed some of the potential applications of this method in mines, including seismic exploration, re-entry protocols and stress change monitoring. All these applications depended on an unresolved question: can the noise generated by mining activity be used to reconstruct the seismic Green's function between sensors in an underground mine?

In Chapter 6, I set about carefully evaluating the seismic noise recorded in mines and its potential use to construct seismic Green's functions. To my knowledge, this has never been done successfully in a mining environment. Before I calculated the cross-correlation functions, I constructed a finite difference numerical model that consisted of the tunnels and mined out areas, to generate numerical estimates of the seismic Green's functions. This was created to investigate if the scattering caused by mining tunnels and voids create favourable conditions to reconstruct the seismic Green's function. I found that the tunnels and excavations cause severe scattering of the seismic waves, indicated by a mean-free-path of roughly 30 meters. Since each of these scatterers can act as secondary seismic sources when excited, the scatterers improve our chances of recovering the seismic Green's function - even in the absence of stable seismic sources.

When considering actual seismic data recorded in an underground mine, I found that some of the seismic noise is not suitable to use to reconstruct the seismic Green's function. In particular, the presence of stable monochromatic signals from mechanical sources (like ventilation fans) prohibit the convergence of the cross-correlation functions to the seismic Green's function. In an effort to suppress these monochromatic signals and amplify the signals that could aid the recovery of the seismic Green's function, I developed a selective processing scheme. By implementing this scheme, I showed that

CONCLUSIONS AND PERSPECTIVES

good estimates of the seismic Green's functions can be retrieved for 80% of the 153 station pairs for the frequency band 20 - 400 Hz.

In the low frequency band (< 100 Hz), the cross-correlation functions are in the single scatter regime and had clear direct arrivals. I used the direct arrivals and an automatic picking algorithm to create a 3D S-wave velocity model of the mining area. The location of a high-velocity anomaly was in agreement for a known ore-body. The differences between the velocity of the ore-body and host rock were estimated from laboratory measurement on core samples and were generally in agreement with my 3D model. This application showed the promise of using the method to create 3D velocity models that can be used for mineral exploration and for locating microseismic events more accurately.

In Chapter 7, I used the reconstructed Green's functions to measure small changes in the seismic velocity during a blast in the mine. I also examined the aftershock activity and modelled the elastic static stress changes associated with the removal of a piece of rock in the location where the blast was performed. This experiment presented a unique opportunity to examine the response of the medium to a large dynamic stress perturbation, and the mechanisms behind earthquake triggering.

A significant velocity drop is visible during the time of the blast, which is interpreted as damage and plastic deformation. This observation has been seen in numerous crustal studies for large earthquakes. These non-elastic effects are healed by the confining stresses over a period of 5 days, until the seismic velocity converges to a new baseline level. The instantaneous weakening and gradual healing observed from the velocity variations are qualitatively similar to results reported in laboratory studies. In my opinion, the most interesting aspect about the velocity variations is that some sensors experience a permanent increase in seismic velocity. The change in the baseline level of the seismic velocity before and after the blast indicates a change in the static stress, that is comparable to the results of elastic static stress modelling. The differences between the elastic stress model predictions and the seismic velocity variations could be due to zones of fractured rock. These zones are indicated by the spatial clustering of the aftershocks, that are not represented by the simple homogeneous isotropic elastic model.

When considering the induced earthquakes, I found that the the locations of the aftershocks appeared clustered and not homogeneously spread around the blast location. The spatial clustering of the aftershocks, along with the location of the damage-driven (immediate) and stress-driven (long-term) velocity changes, indicate that the aftershocks are either located on an optimally orientated fault that was activated by the change in the elastic static stress, or in an area that was highly stressed and more susceptible to fracturing by the blast.

The results presented in this dissertation indicate that ambient seismic noise correlations and the corresponding seismic velocity changes can be used for imaging and monitoring applications in underground mines.

Future work and outlook

I hope that the results presented in this dissertation will form the foundations of some future studies. During the course of my PhD studies, I have found that for the method to work, a thorough investigation of the seismic data is required in order to set up the correct processing parameters. Due to the complexity of the method and the substantial differences between sites, the method can not be used as a "black box" to monitor the elastic properties of the rock inside mines at this stage. Ultimately, I am working towards turning this into a method that can be used routinely in all underground mines with microseismic monitoring networks around the world. I believe this method has tremendous potential in the mining industry to improve miner safety and increase productivity.

Currently, I am working on a few other mining projects where I plan to use the ambient seismic noise based methods developed during my PhD studies, in conjunction with conventional microseismic monitoring. I plan to implement this method to attempt to detect movement in the pit walls of an open pit mine in the near future. For this goal, I have collected more than 1 year of continuous data in an open pit mine. I am also interested in applying this method to underground mines that are prone to relatively large seismic events (for instance deep gold mines in South Africa), since I believe that this method could indicate whether seismic velocity changes can be detected before large earthquakes (which have previously been hinted at). I am currently involved in an industry funded research project to examine whether seismic velocity variations can be used to predict large seismic events in mines. Finally, I hope to implement this method in a mine with a dense sensor network. Some mines have more than 200 seismic sensors in a relatively small region ($< 4 \text{ km}^3$). As stated in Chapter 2.3, this method is ideally suited for large sensor networks. A network with this density provides great potential for this method to image and monitor the mining area with high resolution.

Bibliography

- Ahmadi, O., Juhlin, C., Malehmir, A., and Munck, M. (2013). High-resolution 2d seismic imaging and forward modeling of a polymetallic sulfide deposit at garpenberg, central sweden. *Geophysics*, 78(6):B339–B350.
- Aki, K. (1969). Analysis of seismic coda of local earthquake as scattered waves. *J. Geophys. Res*, 74(2):615–631.
- Aki, K. (1992). Scattering conversions P to S versus S to P. *Bulletin of the Seismological Society of America*, 82:1969–1972.
- Aki, K. and Chouet, B. (1975). Origin of coda waves: source, attenuation and scattering effects. *J. Geophys. Res*, 80(23):3322–3342.
- Aki, K. and Richards, P. (1980). Quantitative seismology: Theory and methods. *Volume I: WH Freeman & Co.*
- Amos, C. B., Audet, P., Hammond, W. C., Bürgmann, R., Johanson, I. A., and Blewitt, G. (2014). Uplift and seismicity driven by groundwater depletion in central california. *Nature*, 509(7501):483–486.
- Aoki, Y. (2015). Monitoring temporal changes of seismic properties. *Frontiers in Earth Science*, 3:42.
- Bakun, W. H. and Lindh, A. G. (1985). The parkfield, california, earthquake prediction experiment. *Science*, 229(4714):619–624.
- Bender, C. M. and Orszag, S. A. (1999). *Advanced Mathematical Methods for Scientists and Engineers I*. Springer Science & Business Media.
- Birch, F. (1961). The velocity of compressional waves in rocks to 10 kilobars: 2. *Journal of Geophysical Research*, 66(7):2199–2224.
- Boliden (2014). Laboratory measurements on core samples at Garpenberg. Internal communications.
- Bonnefoy-Claudet, S., Cotton, F., and Bard, P.-Y. (2006). The nature of noise wavefield and its applications for site effects studies: a literature review. *Earth-Science Reviews*, 79(3):205–227.

BIBLIOGRAPHY

- Boschi, L. and Weemstra, C. (2015). Stationary-phase integrals in the cross-correlation of ambient noise. *Reviews of Geophysics*.
- Bouchon, M., Karabulut, H., Aktar, M., Özalaybey, S., Schmittbuhl, J., and Bouin, M.-P. (2011). Extended nucleation of the 1999 mw 7.6 izmit earthquake. *Science*, 331(6019):877–880.
- Boué, P., Poli, P., Campillo, M., Pedersen, H., Briand, X., and Roux, P. (2013). Teleseismic correlations of ambient seismic noise for deep global imaging of the Earth. *Geophysical Journal International*, 194:844–848.
- Boué, P., Roux, P., Campillo, M., and Briand, X. (2014). Phase velocity tomography of surface waves using ambient noise cross-correlation and array processing. *Journal of Geophysical Research*, 119:519–529.
- Brenguier, F., Campillo, M., Hadziioannou, C., Shapiro, N., Nadeau, R., and Larose, E. (2008a). Postseismic relaxation along the San Andreas fault at Parkfield from continuous seismological observations. *Science*, 321:1478–1481.
- Brenguier, F., Campillo, M., Takeda, T., Aoki, Y., Shapiro, N., Briand, X., Emoto, K., and Miyake, H. (2014). Mapping pressurized volcanic fluids from induced crustal seismic velocity drops. *Science*, 345(6192):80–82.
- Brenguier, F., Clarke, D., Aoki, Y., Shapiro, N., Campillo, M., and Ferrazzini, V. (2011). Monitoring volcanoes using seismic noise correlations. *Comptes Rendus Geoscience*, 343:633â–638.
- Brenguier, F., Shapiro, N., Campillo, M., Ferrazzini, V., Duputel, Z., Coutant, O., and Nercessian, A. (2008b). Towards forecasting volcanic eruptions using seismic noise. *Nature Geoscience*, 321:126–130.
- Brenguier, F., Shapiro, N.M., Campillo, M., Nercessian, A., and Ferrazzini, V. (2007). 3-D surface wave tomography of the Piton de la Fournaise volcano using seismic noise correlations. *Geophys. Res. Lett.*, 34(L02305).
- Cai, W., Dou, L., Cao, A., Gong, S., and Li, Z. (2014). Application of seismic velocity tomography in underground coal mines: A case study of yima mining area, henan, china. *Journal of Applied Geophysics*, 109:140–149.
- Campillo, M. (2006). Phase and Correlation in Random Seismic Fields and the Reconstruction of the Green Function. *Pure Applied Geophysics*, 163:475–502.
- Castellanos, F. and Van der Baan, M. (2015). Dynamic triggering of microseismicity in a mine setting. *Geophysical Journal International*, 202(2):728–737.
- Cheng, X., Niu, F., and Wang, B. (2010). Coseismic velocity change in the rupture zone of the 2008 Mw 7.9 Wenchuan earthquake observed from ambient seismic noise. *Bulletin of the Seismological Society of America*, 100(5B):2539–2550.

- Claerbout, J. F. (1968). Synthesis of a layered medium from its acoustic transmission response. *Geophysics*, 33:264–269.
- Clarke, D., Zaccarelli, L., Shapiro, N., and Brenguier, F. (2011). Assessment of resolution and accuracy of the moving window cross spectral technique for monitoring crustal temporal variations using ambient seismic noise. *Geophysical Journal International*, 1365:867–882.
- Colombi, A., Chaput, J., Brenguier, F., Hillers, G., Roux, P., and Campillo, M. (2014). On the temporal stability of the coda of ambient noise correlations. *Comptes Rendus Geoscience*, 346(11):307–316.
- Dainty, A. and Toksoz, M. (1977). Seismic codas on the earth and the moon: a comparison. *Physics of the earth and planetary interiors*, 26:250–260.
- Derode, A., Larose, E., Campillo, M., and Fink, M. (2003). How to estimate the Green’s function for a heterogeneous medium between two passive sensors? *Applied Physics Letters*, 83:3054–3056.
- Draganov, D., Campman, X., Thorbecke, J., Verdel, A., and Wapenaar, K. (2009). Reflection images from ambient seismic noise. *Geophysics*, 74:A63–A67.
- Duvall, T., D’silva, S., Jefferies, S., Harvey, J., and Schou, J. (1996). Downflows under sunspots detected by helioseismic tomography. *Nature*, 379(6562):235–237.
- Eberhart-Phillips, D., Han, D.-H., and Zoback, M. D. (1989). Empirical relationships among seismic velocity, effective pressure, porosity, and clay content in sandstone. *Geophysics*, 54(1):82–89.
- Ekström, G. (2001). Time domain analysis of earth’s long-period background seismic radiation. *Journal of Geophysical Research: Solid Earth (1978–2012)*, 106(B11):26483–26493.
- Fairhurst, C. (2003). Stress estimation in rock: a brief history and review. *International Journal of Rock Mechanics and Mining Sciences*, 40(7):957–973.
- Fazio, T. D., Aki, L., and Alba, K. (1973). Solid earth tide and observed change in the in situ seismic velocity. *Journal of Geophysical Research*, 78:1319–1322.
- Forghani, F. and Snieder, R. (2010). Underestimation of body waves and feasibility of surface wave reconstruction by seismic interferometry. *The Leading Edge*, 29:790–794.
- Frankel, A., McGarr, A., Bicknell, J., Mori, J., Seeber, L., and Cranswick, E. (1990). Attenuation of high-frequency shear waves in the crust: Measurements from New York State, South Africa, and southern California. *Journal of Geophysical Research: Solid Earth*, 95(B11):17441–17457.

BIBLIOGRAPHY

- Friedel, M., Jackson, M., Scott, D., Williams, T., and Olson, M. (1995). 3-D tomographic imaging of anomalous conditions in a deep silver mine. *Journal of applied geophysics*, 34(1):1–21.
- Friedel, M., Scott, D., Jackson, M., Williams, T., and Killen, S. (1996). 3-D tomographic imaging of anomalous stress conditions in a deep US gold mine. *Journal of applied geophysics*, 36(1):1–17.
- Froment, B., Campillo, M., Roux, P., Gouédard, P., Verdel, A., and Weaver, R. L. (2010). Estimation of the effect of nonisotropically distributed energy on the apparent arrival time in correlations. *Geophysics*, 75(5):SA85–SA93.
- Gomberg, J., Bodin, P., Larson, K., and Dragert, H. (2004). Earthquake nucleation by transient deformations caused by the m = 7.9 denali, alaska, earthquake. *Nature*, 427(6975):621–624.
- Gomberg, J., Bodin, P., and Reasenberg, P. A. (2003). Observing earthquakes triggered in the near field by dynamic deformations. *Bulletin of the Seismological Society of America*, 93(1):118–138.
- Gomberg, J., Reasenberg, P., Bodin, P., and Harris, R. (2001). Earthquake triggering by seismic waves following the landers and hector mine earthquakes. *Nature*, 411(6836):462–466.
- Gonzalez-Huizar, H. and Velasco, A. A. (2011). Dynamic triggering: Stress modeling and a case study. *Journal of Geophysical Research: Solid Earth*, 116(B2):2304. B02304.
- Gouedard, P., Stehly, L., Brenguier, F., Campillo, M., de Verdiere, Y. C., Larose, E., Margerin, L., Roux, P., Sanchez-Sesma, F., Shapiro, N. M., and Weaver, R. (2008). Cross-correlation of random fields: mathematical approach and applications. *Geophysical Prospecting*, 56:375–393.
- Grêt, A., Snieder, R., and Özbay, U. (2006). Monitoring in situ stress changes in a mining environment with coda wave interferometry. *Geophysical Journal International*, 167(2):504–508.
- Hadziioannou, C., Larose, E., Coutant, O., Roux, P., and Campillo, M. (2009). Stability of Monitoring Weak Changes in Multiply Scattering Media with Ambient Noise Correlation: Laboratory Experiments. *Journal of the Acoustical Society of America*, 125:3688–3695.
- Hasselmann, K. (1963). A statistical analysis of the generation of microseisms. *Reviews of Geophysics*, 1(2):177–210.
- Hill, D., Reasenberg, P., Michael, A., Arabaz, W., Beroza, G., Brumbaugh, D., Brune, J., Castro, R., Davis, S., Ellsworth, W., et al. (1993). Seismicity remotely triggered by the magnitude 7.3 landers, california, earthquake. *Science*, 260(5114):1617–1623.

- Hillers, G., Ben-Zion, Y., Campillo, M., and Zigone, D. (2015a). Seasonal variations of seismic velocities in the san jacinto fault area observed with ambient seismic noise. *Geophysical Journal International*, 202(2):920–932.
- Hillers, G., Campillo, M., and Ma, K.-F. (2014). Seismic velocity variations at TCDP are controlled by MJO driven precipitation pattern and high fluid discharge properties. *Earth and Planetary Science Letters*, 391:121–127.
- Hillers, G., Husen, S., Obermann, A., Planès, T., Campillo, M., and Larose, E. (2015b). Noise based monitoring and imaging resolve reservoir dynamics associated with the 2006 basel injection experiment. *Geophysics*, in press.
- Huang, J., Reyes-Montes, J., and Young, R. (2013). Passive three-dimensional micro-seismic imaging for mining-induced rock-mass degradation. *RapidMiner: Data Mining Use Cases and Business Analytics Applications*, page 135.
- Jackson, M., Friedel, M., Tweeton, D., Scott, D., and Williams, T. (1995). Three-dimensional imaging of underground mine structures using seismic tomography. In *8th EEGS Symposium on the Application of Geophysics to Engineering and Environmental Problems*.
- Jager, A. and Ryder, J. (2002). *A textbook on rock mechanics for tabular hard rock mines*. Safety in Mines Research Advisory Committee (SIMRAC).
- Johnson, C. W., Burgmann, R., and Pollitz, F. F. (2015). Rare dynamic triggering of remote $M > 5.5$ earthquakes from global catalog analysis. *Journal of Geophysical Research: Solid Earth*, 120(3):1748–1761. 2014JB011788.
- Johnson, P. and Sutin, A. (2005). Slow dynamics and anomalous nonlinear fast dynamics in diverse solids. *The Journal of the Acoustical Society of America*, 117(1):124–130.
- Johnson, P. A. and Jia, X. (2005). Nonlinear dynamics, granular media and dynamic earthquake triggering. *Nature*, 437(7060):871–874.
- Kanu, C., Snieder, R., and Pankow, K. (2014). Time-lapse monitoring of velocity changes in utah. *Journal of Geophysical Research: Solid Earth*, 119(9):7209–7225.
- Kukkonen, I. T., Heikkinen, P., Heinonen, S., and Laitinen, J. (2011). Reflection seismics in exploration for mineral deposits: Initial results from the hire project. *Geological Survey of Finland Special Paper*, 49:49–58.
- Langet, N., Maggi, A., Michelini, A., and Brenguier, F. (2014). Continuous Kurtosis-Based Migration for Seismic Event Detection and Location, with Application to Piton de la Fournaise Volcano, La Réunion. *Bulletin of the Seismological Society of America*, 104:229–246.
- Larose, E. and Hall, S. (2009). Monitoring stress related velocity variation in concrete with a 2×10^{-5} relative resolution using diffuse ultrasound. *The Journal of the Acoustical Society of America*, 125(4):1853–1856.

BIBLIOGRAPHY

- Larose, E., Roux, P., Campillo, M., and Derode, A. (2008). Fluctuations of correlations and Green's function reconstruction: role of scattering. *Journal of Applied Physics*, 103:114907.
- Leary, P., Malin, P., Phinney, R., Brocher, T., and Voncolln, R. (1979). Systematic monitoring of millisecond travel time variations near Palmdale, California. *Journal of Geophysical Research: Solid Earth (1978–2012)*, 84(B2):659–666.
- Lin, F., Li, D., Clayton, R. W., and Hollis, D. (2013a). High-resolution 3D shallow crustal structure in Long Beach, California: Application of ambient noise tomography on a dense seismic array. *Geophysics*, 78:45–56.
- Lin, F., Schmandt, B., and Tsai, V. (2013b). Joint inversion of Rayleigh wave phase velocity and ellipticity using USArray: constraining velocity and density structure in the upper crust. *Geophysical Research Letters*, 39:12303.
- Lin, F.-C., Moschetti, M. P., and Ritzwoller, M. H. (2008). Surface wave tomography of the western united states from ambient seismic noise: Rayleigh and love wave phase velocity maps. *Geophysical Journal International*, 173(1):281–298.
- Lobkis, O. and Weaver, R. (2001). On the emergence of the Green's function in the correlation of a diffuse field. *Journal of the Acoustical Society of America.*, 110:311–317.
- Lockner, D., Walsh, J., and Byerlee, J. (1977). Changes in seismic velocity and attenuation during deformation of granite. *Journal of Geophysical Research*, 82(33):5374–5378.
- Longuet-Higgins, M.S. (1950). A theory of the origin of microseisms. *Philos. Trans. R. Soc. London, Ser. A*, 243:1–35.
- Lucente, F. P., De Gori, P., Margheriti, L., Piccinini, D., Di Bona, M., Chiarabba, C., and Agostinetti, N. P. (2010). Temporal variation of seismic velocity and anisotropy before the 2009 mw 6.3 l'aquila earthquake, italy. *Geology*, 38(11):1015–1018.
- Lurka, A. and Swanson, P. (2009). Improvements in seismic event locations in a deep western us coal mine using tomographic velocity models and an evolutionary search algorithm. *Mining Science and Technology (China)*, 19(5):599–603.
- Luxbacher, K., Westman, E., Swanson, P., and Karfakis, M. (2008). Three-dimensional time-lapse velocity tomography of an underground longwall panel. *International Journal of Rock Mechanics and Mining Sciences*, 45(4):478–485.
- Lyakhovskiy, V., Hamiel, Y., Ampuero, J.-P., and Ben-Zion, Y. (2009). Non-linear damage rheology and wave resonance in rocks. *Geophysical Journal International*, 178(2):910–920.
- Lynch, R. and Lotter, E. (2007). Estimation of cave geometry using a constrained velocity model inversion with passive seismic data. *Journal of the South African Institute of Mining & Metallurgy*, 107(12):791.

- Mainsant, G., Larose, E., Bronnimann, C., Jongmans, D., Michoud, C., and Jaboyedoff, M. (2013). Ambient seismic noise monitoring of a clay landslide: toward failure prediction. *Journal of Geophysical Research*, 117:F01030.
- Malehmir, A., Durrheim, R., Bellefleur, G., Urosevic, M., Juhlin, C., White, D. J., Milkereit, B., and Campbell, G. (2012). Seismic methods in mineral exploration and mine planning: A general overview of past and present case histories and a look into the future. *Geophysics*, 77(5):WC173–WC190.
- Mantovani, E., Viti, M., Babbucci, D., Albarello, D., Cenni, N., and Vannucchi, A. (2010). Long-term earthquake triggering in the southern and northern apennines. *Journal of seismology*, 14(1):53–65.
- Margerin, L., Campillo, M., and Tiggelen, B. V. (2000). Monte Carlo Simulation of multiple scattering of elastic waves. *Journal of Geophysical Research*, 105(B4):7873–7892.
- Maxwell, S. and Young, R. (1992). Sequential velocity imaging and microseismic monitoring of mining-induced stress change. *Pure and Applied Geophysics*, 139(3-4):421–447.
- Meier, U., Shapiro, N. M., and Brenguier, F. (2010). Detecting seasonal variations in seismic velocities within Los Angeles basin from correlations of ambient seismic noise. *Geophysical Journal International*, 181(2):985–996.
- Mendecki, A. J. (1997). *Seismic monitoring in mines*. Springer Science & Business Media.
- Mjachkin, V., Brace, W., Sobolev, G., and Dieterich, J. (1975). Two models for earthquake forerunners. In *Earthquake Prediction and Rock Mechanics*, pages 169–181. Springer.
- Moschetti, M. P., Ritzwoller, M. H., and Shapiro, N. (2007). Surface wave tomography of the western United States from ambient seismic noise: Rayleigh wave group velocity maps. *Geochemistry Geophysics Geosystems*, 8:Q08010.
- Murnaghan, F. D. (1951). *Finite deformation of an elastic solid*. Dover Publications Inc.
- Nakamura, Y. (1977). Seismic energy transmission in an intensively scattering medium. *Journal of Geophysics*, 43:389–399.
- Nakata, N., Chang, J. P., Lawrence, J. F., and Boué, P. (2015). Body wave extraction and tomography at long beach, california, with ambient-noise interferometry. *Journal of Geophysical Research: Solid Earth*, 120(2):1159–1173.
- Nakata, N. and Snieder, R. (2011). Near-surface weakening in Japan after the 2011 Tohoku-Oki earthquake. *Geophysical Research Letters*, 38(17):L17302.

BIBLIOGRAPHY

- Niu, F., Silver, P. G., Daley, T. M., Cheng, X., and Majer, E. L. (2008). Preseismic velocity changes observed from active source monitoring at the Parkfield SAFOD drill site. *Nature*, 454(7201):204–208.
- Nur, A. (1971). Effects of stress on velocity anisotropy in rocks with cracks. *Journal of Geophysical Research*, 76(8):2022–2034.
- Nur, A. and Simmons, G. (1969). Stress-induced velocity anisotropy in rock: An experimental study. *Journal of Geophysical Research*, 74(27):6667–6674.
- Obermann, A., Kraft, T., Larose, E., and Wiemer, S. (2015). Potential of ambient seismic noise techniques to monitor the st. gallen geothermal site (switzerland). *Journal of Geophysical Research: Solid Earth*.
- O’Connell, R. J. and Budiansky, B. (1974). Seismic velocities in dry and saturated cracked solids. *Journal of Geophysical Research*, 79(35):5412–5426.
- Olivier, G., Brenguier, F., Campillo, M., Lynch, R., and Roux, P. (2015). Body-wave reconstruction from ambient seismic noise correlations in an underground mine. *Geophysics*, 80(3):KS11–KS25.
- Patanè, D., Barberi, G., Cocina, O., De Gori, P., and Chiarabba, C. (2006). Time-resolved seismic tomography detects magma intrusions at mount etna. *Science*, 313(5788):821–823.
- Picozzi, M., Parolai, S., Bindi, D., and Strollo, A. (2009). Characterization of shallow geology by high-frequency seismic noise tomography. *Geophysical Journal International*, 176:164–174.
- Poupinet, G., Ellsworth, W. L., and Frechet, J. (1984). Monitoring velocity variations in the crust using earthquake doublets: An application to the Calaveras Fault, California. *Journal of Geophysical Research: Solid Earth*, 89(B7):5719–5731.
- Reasonberg, P. and Aki, K. (1974). A precise, continuous measurement of seismic velocity for monitoring in situ stress. *Journal of Geophysical Research*, 79:399–406.
- Rhie, J. and Romanowicz, B. (2004). Excitation of earth’s continuous free oscillations by atmosphere–ocean–seafloor coupling. *Nature*, 431(7008):552–556.
- Rhie, J. and Romanowicz, B. (2006). A study of the relation between ocean storms and the earth’s hum. *Geochemistry, Geophysics, Geosystems*, 7(10).
- Riemer, K. and Durrheim, R. (2011). Mining seismicity in the witwatersrand basin: monitoring, mechanisms and mitigation strategies in perspective. *Journal of Rock Mechanics and Geotechnical Engineering*, 3(3):250–259.
- Ritzwoller, M., Lin, F., and Shen, W. (2011). Ambient noise tomography with a large seismic array. *C.R. Geoscience*, 343(8):558–570.

- Roux, P. and Kuperman, W. (2004). Extracting coherent wavefronts from acoustic ambient noise in the ocean. *Journal of the Acoustical Society of America*, 116:1995–2003.
- Roux, P., Sabra, K., Gerstoft, P., and Kuperman, W. (2005a). P-waves from crosscorrelation of seismic noise. *Geophysical Research Letters*, 32:L19303.
- Roux, P., Sabra, K. G., Kuperman, W., and Roux, A. (2005b). Ambient noise cross correlation in free space: Theoretical approach. *The Journal of the Acoustical Society of America*, 117(1):79–84.
- Sabra, K., Gerstoft, P., Roux, P., Kuperman, W., and Fehler, M. (2005a). Surface wave tomography from microseisms in southern California. *Geophysical Research Letters*, 32:L14311.
- Sabra, K.G., Gerstoft, P., Roux, P., Kuperman, W.A., and Fehler, M. (2005b). Extracting time domain Green’s function estimates from ambient seismic noise. *Geophysical Research Letters*, 32(L03310).
- Sawazaki, K., Kimura, H., Shiomi, K., Uchida, N., Takagi, R., and Snieder, R. (2015). Depth-dependence of seismic velocity change associated with the 2011 tohoku earthquake, japan, revealed from repeating earthquake analysis and finite-difference wave propagation simulation. *Geophysical Journal International*, 201(2):741–763.
- Scholz, C. H. (2002). *The mechanics of earthquakes and faulting*. Cambridge university press.
- Scott, D., Williams, T., and Friedel, M. (1996). Application of seismic tomography in underground mining. Technical report, Colorado School of Mines, Golden, CO (United States).
- Seats, K. J. and Lawrence, J. F. (2014). The seismic structure beneath the yellowstone volcano field from ambient seismic noise. *Geophysical Research Letters*, 41(23):8277–8282.
- Sens-Schönfelder, C. and Wegler, U. (2006). Passive image interferometry and seasonal variations of seismic velocities at merapi volcano, indonesia. *Geophysical research letters*, 33(21).
- Sewee, R., Lynch, R., and Du Toit, C. (2008). Locating seismic events in mines containing strongly heterogeneous media. *Proceedings of the Fifth International Conference and Exhibition on Mass Mining, Lulea, Sweden*.
- Shapiro, N., Campillo, M., Stehly, L., and Ritzwoller, M. (2005). High resolution surface-wave tomography from ambient seismic noise. *Science*, 307:615–618.
- Shapiro, N. M. and Campillo, M. (2004). Emergence of broadband Rayleigh waves from correlations of the ambient seismic noise. *Geophysical Research Letters*, 31(7):L07614.

BIBLIOGRAPHY

- Shapiro, S., Patzig, R., Rothert, E., and Rindschwentner, J. (2003). Triggering of seismicity by pore-pressure perturbations: Permeability-related signatures of the phenomenon. *Pure and applied geophysics*, 160(5-6):1051–1066.
- Silver, P. G., Daley, T. M., Niu, F., and Majer, E. L. (2007). Active source monitoring of cross-well seismic travel time for stress-induced changes. *Bulletin of the Seismological Society of America*, 97(1B):281–293.
- Snieder, R. (2004). Extracting the Green’s function from the correlation of coda waves: A derivation based on stationary phase. *Physics Review E*, 69:046610.
- Snieder, R. (2006). The theory of coda wave interferometry. *Pure and applied geophysics*, 163(2):455–473.
- Snieder, R. and Hagerty, M. (2004). Monitoring change in volcanic interiors using coda wave interferometry: Application to Arenal Volcano, Costa Rica. *Geophysical Research Letters*, 31(9):L09608.
- Spottiswoode, S. and Linzer, L. (2005). A hybrid location methodology. *South African Institute of Mining and Metallurgy*, 105(6):417.
- Stehly, L., Campillo, M., Froment, B., and Weaver, R. (2008). Reconstructing Green’s function by correlation of the coda of the correlation (C^3) of ambient seismic noise. *Journal of Geophysical Research*, 113:B11306.
- Stein, R. S. (1999). The role of stress transfer in earthquake occurrence. *Nature*, 402(6762):605–609.
- Taira, T., Brenguier, F., and Kong, Q. (2015). Ambient noise based monitoring of seismic velocity changes associated with the 2014 mw 6.0 south napa earthquake. *Geophysical Research Letters*.
- Tanimoto, T. (2005). The oceanic excitation hypothesis for the continuous oscillations of the earth. *Geophysical Journal International*, 160(1):276–288.
- Tanimoto, T. and Um, J. (1999). Cause of continuous oscillations of the earth. *Journal of Geophysical Research: Solid Earth (1978–2012)*, 104(B12):28723–28739.
- Tape, C., West, M., Silwal, V., and Ruppert, N. (2013). Earthquake nucleation and triggering on an optimally oriented fault. *Earth and Planetary Science Letters*, 363:231–241.
- Tsai, V. (2009). On establishing the accuracy of noise tomography travel-time measurements in a realistic medium. *Geophysical Journal International*, 178:1555–1564.
- Tsai, V. C. (2011). A model for seasonal changes in gps positions and seismic wave speeds due to thermoelastic and hydrologic variations. *Journal of Geophysical Research: Solid Earth (1978–2012)*, 116(B4).

- Vallejos, J. and McKinnon, S. (2010). Omori's law applied to mining-induced seismicity and re-entry protocol development. *Pure and Applied Geophysics*, 167(1-2):91–106.
- Verdon, J. P., Angus, D. A., Michael Kendall, J., and Hall, S. A. (2008). The effect of microstructure and nonlinear stress on anisotropic seismic velocities. *Geophysics*, 73(4):D41–D51.
- Wang, B., Zhu, P., Chen, Y., Niu, F., and Wang, B. (2008). Continuous subsurface velocity measurement with coda wave interferometry. *Journal of Geophysical Research: Solid Earth (1978–2012)*, 113(B12).
- Wapenaar, K. (2004). Retrieving the elastodynamic Green's function of an arbitrary inhomogeneous medium by cross-correlation. *Physics Review Letters*, 93:254301.
- Weaver, R., Froment, B., and Campillo, M. (2009). On the correlation of non-isotropically distributed ballistic scalar diffuse waves. *Journal of the Acoustical Society of America*, 126:1817–1826.
- Webb, S. (1998). Broadband seismology and noise under the ocean. *Reviews of Geophysics*, 36:105–142.
- Wegler, U. and Luhr, B. (2001). Scattering behaviour at Merapi volcano (Java) revealed from an active seismic experiment. *Geophysics Journal International*, 145:579 – 592.
- Wegler, U., Nakahara, H., Sens-Schönfelder, C., Korn, M., and Shiomi, K. (2009). Sudden drop of seismic velocity after the 2004 mw 6.6 mid-niigata earthquake, japan, observed with passive image interferometry. *Journal of Geophysical Research*, 114(B6).
- Westman, E., Luxbacher, K., and Schafrik, S. (2012). Passive seismic tomography for three-dimensional time-lapse imaging of mining-induced rock mass changes. *The Leading Edge*, 31(3):338–345.
- Whitcomb, J. H., Garmany, J. D., and Anderson, D. L. (1973). Earthquake prediction: Variation of seismic velocities before the san francisco earthquake. *Science*, 180(4086):632–635.
- Yamamura, K., Sano, O., Utada, H., Takei, Y., and Nakao, S. (2003). Long-term observation of in situ seismic velocity and attenuation. *Journal of Geophysical Research*, 108:2317–2331.
- Yang, Y.J., Ritzwoller, M.H., Levshin, A., and Shapiro, N.M. (2007). Ambient noise Rayleigh wave tomography across Europe. *Geophysical Journal International*, 168(1):259–274.
- Yao, H. and van der Hilst, R.D. (2009). Analysis of ambient noise energy distribution and phase velocity bias in ambient noise tomography, with application to SE Tibet. *Geophysical Journal International*, 179(2):1113–1132.

BIBLIOGRAPHY

- Zhan, Z. and Ni, S. (2010). Stationary phase approximation in the ambient noise method revisited. *Earthquake Science*, 23(5):425–431.
- Zhang, H., Thurber, C., and Rowe, C. (2003). Automatic P-Wave Arrival Detection and Picking with Multiscale Wavelet Analysis for Single-Component Recordings. *Bulletin of the Seismological Society of America*, 93:1904–1912.
- Zhang, J., Gerstoft, P., and Shearer, P. (2009). High-frequency P-wave seismic noise driven by ocean winds. *Geophysical Research Letters*, 36:L09392.

